MOLECULAR DYNAMICS SIMULATIONS OF THE STRUCTURE AND FAILURE OF SILICATE GLASSES

BY

LAURA R. V. ADKINS

A THESIS

SUBMITTED TO THE FACULTY OF

ALFRED UNIVERSITY

IN PARTIAL FULFILLMENT OF THE REQUIREMENTS
FOR THE DEGREE OF

DOCTOR OF PHILOSOPHY

IN

MATERIALS SCIENCE AND ENGINEERING

ALFRED, NEW YORK

DECEMBER, 2011

MOLECULAR DYNAMICS SIMULATIONS OF THE STRUCTURE

AND FAILURE OF SILICATE GLASSES

BY

LAURA R. V. ADKINS

B.S. SUNY FREDONIA (2007), B.S. ALFRED UNIVERSITY(2007)

SIGNATURE OF AUTHOR_____

APPROVED BY _____
ALASTAIR N. CORMACK, ADVISOR

_____
JAMES VARNER, ADVISORY COMMITTEE

_____
NATHAN MELLOTT, ADVISORY COMMITTEE

_____
WILLIAM LACOURSE, ADVISORY COMMITTEE

_____
WALTER SCHULZE, ADVISORY COMMITTEE

_____
CHAIR, ORAL THESIS DEFENSE

ACCEPTED BY _____
DOREEN D. EDWARDS, DEAN
KAZUO INAMORI SCHOOL OF ENGINEERING

ACCEPTED BY _____
NANCY J. EVANGELISTA, ASSOCIATE PROVOST
FOR GRADUATE AND PROFESSIONAL PROGRAMS
ALFRED UNIVERSITY

ACKNOWLEDGMENTS

I would like to extend my sincere thanks to my advisor, Dr. Alastair Cormack, for his assistance, guidance and advice as I worked to complete this research. I also thank my committee members, for their help in revising this document, and for their comments and suggestions as I brought questions to them.

This path has not led me down the smoothest of roads, and assistance in the journey was always very much appreciated.

I've enjoyed the community of my office, and must thank Bu Wang, Rob Koch, and Sam Lamphier for their advice and support as I worked to complete this document. No matter how many times in a day I started to pose a question, or asked for opinions, they listened, and responded thoughtfully. This was an invaluable help.

I also extend my thanks to my family and friends for their kind support and encouragement throughout this process. Thank you for listening to excruciatingly long stories, and for offering advice and suggestions. Thanks to my sister, Rachel VanCott, especially, for her help in editing and technical advice.

I thank Alfred University for supporting this work financially by granting me a post as a teaching assistant. I also thank the International Materials Institute, the organizers of the 9th Conference on the Advanced Fusion and Processing of Glass, and Alfred University again, along with Dr. Cormack, for financially supporting my international travel to present my research abroad and to learn from the research of others. My trips to Japan, France, and Australia have changed the way I see both our scientific community and the world.

Finally, I'd like to thank my husband, Ian Adkins, for his unflagging support and love throughout these last four and half years of research. His consistent confidence in my abilities has helped me to work through research that was challenging, and occasionally discouraging, to come out on the other side, better for the journey.

TABLE OF CONTENTS

Page

LIST OF TABLES

LIST OF FIGURES

ABSTRACT

Molecular dynamics simulations were used to study the atomic structure of silica glass fibers and bulk sodium silicate and sodium aluminosilicate glasses, both at rest and strained under tension until failure.

The sodium silicate and sodium aluminosilicate glass samples were found to have an atomic structure that agreed well with the results of other computational work and experiments, but some small discrepancies were noted. A shift in the proportion of Q_n species as well as a small number of five-coordinated silicon and triply-bridged oxygen, especially noted in large-scale simulation, suggested that the sample had an elevated structural temperature. Thus, the formed structure was found to be more analogous to a splat-cooled glass than a traditionally annealed sample.

This work marks the first computational study wherein silica glass fibers were formed in their entirety. Fiber samples were formed in varying sizes and with several different cross-sectional geometries. Upon analysis, the fibers were found to have a distinct surface layer between 5.7 and 11Å thick, with a lower-density structure than the bulk, populated with unusually coordinated, or defect, species. Surface layer thickness was found to vary with sample size, but this dependence rapidly dropped off as system size was increased.

When the silica glass fibers were strained, they broke at failure stress values of 12.21±0.04, 11.63±0.05, and 12.21±0.06 GPa, agreeing well with experiment, but at lower values of strain than expected. The failure of the fibers was initiated at the surface and the formed crack moved through the bulk of the material through to the other side of the fiber to break it in two. These cracks that caused failure were usually formed by bond breakages around three-coordinated silicon, triply-bridged oxygen, or bonds aligned with the strain axis.

The sodium silicate and sodium aluminosilicate glass samples behaved in an unexpected manner under strain, stretching as if they were viscous rather than brittle solids. No clear cause for this behavior has been found.

Chapter One – Introduction

1. Motivation

Glass is a brittle material, and when stressed beyond tolerance levels, glass bodies break quickly, without warning. The cracks that propagate through glass can travel at velocities as low as 30m/s,[1] up to the theoretical Rayleigh wave speed for a specific glass composition, for example, 5300 m/s for soda lime silicate glasses.[2] This fast failure can be observed through the use of high speed cameras,[2,3] and fractography can be used to characterize how the failure occured.[4] However, these observations are made on a macro and microscale level, and shed no light on the atomic processes occurring during failure.

The atomic changes that occur in the structure under stress, if observed, could be used to suggest changes that will allow us to better control its behavior. Similarly, understanding the glass structure itself, in the absence of a dynamic process, is important. Material properties are often defined by their atomic structure, and small changes in composition can drastically alter the structure. Without a clear understanding of the material structure, property changes that occur can be unexpected and unintended.

In general, atoms on a carefully prepared surface can be observed individually, using scanning-tunneling microscopy,[5] but this technique is limited to atoms directly on the surface of a material. Further, mechanical limitations of the scanning process make it difficult to observe a dynamic event that occurs as quickly as brittle failure. Because glasses possess no long-range order,[6] most experimental techniques that rely on regular crystal structure, such as (standard) x-ray diffraction, cannot be used to characterize the atomic structure. Glasses do posses short- and medium-range order to describe the regular angles found in tetrahedra, and the ring structures seen in the glass. Nuclear magnetic resonance techniques and neutron (and x-ray) scattering[7,8] can be used to gather information about the short- and medium-range order of glass structure[9], but this information is statistical, and cannot illustrate more subtle structural features. Since neither the bulk atomic structures of a glass, nor changes to that structure as it is strained are directly observable by experimental means, an alternative technique must be used to explore these details.

Computational simulation methods provide a solution to this situation. Using atomistic modeling techniques, the structure of a material can be visually and quantitatively observed, both at a material surface and within the bulk. Changes to the material structure over time, under applied conditions, can be directly observed, and fast dynamic processes can be followed in detail.

2. General Introduction

In the time since the general method for conducting molecular dynamics simulations was introduced by Alder and Wainwright in the late 1950's[10], the technique has been adapted from the initial task of examining the interaction of hard, perfectly elastic spheres, to more realistically representing the motion of atoms. Interatomic potential models were developed to describe the changing forces between atoms as they moved throughout the system, initially for liquid argon using a Lennard-Jones potential,[11] but eventually for a wide range of materials.[12]

Vitreous silica was first modeled by Woodcock et al,[13] producing a simulated glass that agreed reasonably well with the radial distribution function gathered from X-ray studies. Many simulations have since been conducted to study the structure and properties of silica glass that would be otherwise unobtainable by experimental means. Structural features of a bulk sample of silica glass have been examined, as well as the structural features of many other compositions. [14-23]

Research has also been done to examine the surface structure of silica glass.[24-29] In examining this surface, researchers found a surface layer that extended approximately 5 to 10Å into the glass, containing unusually coordinated species such as three-coordinated silicon atoms, non-bridging oxygen atoms, and silica tetrahedra in coordination other than Q_4.

As technology has advanced, and computing resources have become more abundant and affordable, it has become possible to work with the larger and more complex systems that have been too computationally expensive in the past. Although studies of silica have grown to include examination of surfaces, as previously mentioned, no samples with more complex geometries than a flat plate have been studied. This has been partially due to the fact that large-scale computer simulations, creating samples of

small experimental size, have been computationally expensive. Through the use of a Blue Gene/L supercomputer, we have prepared and examined the structure of silica glass fibers, up to a small experimental scale.

In addition to studying glass structure under ambient conditions, researchers have used atomistic modeling to study the changes to structure in non-standard pressure[30-33] and temperature[19,34,35] conditions. Recently, a procedure was established by Pedone et al.[36] to strain a bulk glass under tension until failure. This procedure allowed relaxation of the structure in the directions not strained, making it possible to include a non-zero Poisson's ratio in the simulation, a detail not incorporated into a number of other simulations of the failure of silica glass.[37-39] This technique has been applied to the silica glass fibers modeled in this thesis, and also to the bulk glass samples in the sodium silicate and sodium aluminosilicate compositional families.

In Chapter Two of this work, the structural features of sodium silicate and sodium aluminosilicate glasses are discussed. Chapter Three presents the forming process used to create fibers of silica glass, and in Chapter Four, the failure of these fibers under tension is analyzed. Within Chapter Five, the results of the work on straining sodium silicate glasses until failure are presented.

3. Molecular Dynamics Methodology

A number of different techniques are commonly used to examine the atomic structure of glass through computer simulations. In classical Molecular Dynamics (MD) simulations, the equations of Newtonian physics are used to calculate the position, velocity, and acceleration of atoms in a simulated sample. A Born model of the solid is used, in which interatomic forces are calculated using a potential model with atom specific parameters to dictate the interactions of atoms in the system.[12] After the forces are calculated, the atoms in the sample are allowed to move in three-dimensional space for a very short period of time before forces are recalculated based on the new atomic positions. Over many iterations of this process, the sample acquires a structure that is characteristic of the material simulated, at a dictated pressure and temperature.[12]

Although this technique does not account for the full complexity of atomic interactions as understood through quantum mechanics, simulations using interatomic

potential models containing tens of thousands, or even millions of atoms can be conducted in a reasonable amount of time.[40] Simulations using quantum mechanical (QM) considerations are computationally demanding and are limited to less than 200 atoms by the currently available resources. For each timestep of a Molecular Dynamics simulation, the forces on the atoms of the system are recalculated and velocities are rescaled, based on the set equations. To advance a timestep in a QM simulation, a large number of integrals must be carried out to find the most favorable electronic state of the system, and this takes significantly more computational time than a timestep in MD. Since both types of simulation require more time as a larger number of atoms are used, the extra computational power required for QM calculations limits the number of atoms in these studies.[41]

The potential model and atomic parameters used in these studies are shown in Equation 1-1 and Table I-I.

$$U_{ij}(r) = \frac{z_i z_j e^2}{r_{ij}} + D_{ij}\left[\left\{1 - e^{-a_{ij}(r_{ij}-r_0)}\right\}^2 - 1\right] + \frac{C_{ij}}{r_{ij}^{12}} \qquad (1\text{-}1)$$

Table I-I. Interatomic Parameters Used in This Work

Interaction	D_{ij} (eV)	a_{ij} (A^{-2})	r_o (A)	C_{ij} (eV A^{12})
Al-O	0.361581	1.900442	2.164818	0.9
Na-O	0.023363	1.763867	3.006315	5.0
O-O	0.042395	1.379316	3.618701	22.0
Si-O	0.340554	2.006700	2.100000	1.0

This potential model[42] was empirically developed for use with silicate glasses, and the total energy is given by the sum of all U_{ij} for individual pairs of atoms *i* and *j*. The equation consists of a long-range Coulomb potential, a short-range Morse potential and an additional repulsive term, presented from left to right Equation 1-1, separated by addition signs. Traditionally, the terms of a Morse function have direct physical

meaning, related to the bond dissociation energy, potential energy well, and equilibrium bond distance, D_{ij}, a_{ij}, and r_o, respectively in small molecules, but because this potential explicitly includes a Coulomb term, the values shown in Table I-I are best considered as just parameters.[42] Long-range forces were calculated using Ewald summation, with a cutoff distance of 12 Å, and short-range forces were calculated to a cutoff of 6 Å. The additional repulsive term of this potential, C_{ij}/r^{12}, is significant only at the high temperatures required for melting a glass, and keeps atoms from getting too close to one another when they move at the high speeds associated with high temperature.

MD simulations must also account for ambient conditions, in addition to the interatomic potentials and Newton's laws of motion. To that end, thermostat and barostat algorithms are used to control the temperature and pressure of the sample, as dictated by the system constraints. In order to control temperature, a kinetic thermostat is employed, [43-45] which uses Equation 1-2 to calculate the temperature of the system based on an average of the kinetic energies of the atoms.

$$\left\langle \sum_{i=1}^{N} \frac{p_i^2}{2m_i} \right\rangle = \frac{3}{2} N k_B T_{kinetic} \tag{1-2}$$

p = atom momentum m= atom mass $k_{b=}$ Boltzmann's constant T = temperature
N= number of atoms

Adjustments to the temperature are made by scaling the kinetic energy of all the atoms of the system up or down to bring the average closer to the target temperature. Similarly, pressure can be held constant though adjustments to the cell volume. In this work, a Berendsen thermostat and barostat[46] were used to control system temperature and pressure, due to their high efficiency of calculations.

For the MD studies presented in this work, a prepared package called DL_POLY, with some in-house modifications, was used.[47] Samples were evaluated at room temperature (300K) and zero pressure unless otherwise stated.

4. Formation of a Glass Sample

To form a glass, a sample box of randomly positioned, stoichiometrically balanced atoms is held at a high kinetic temperature to simulate the disorder of a liquid structure. The temperature of the system is then reduced to room temperature under NVT conditions, as shown in Figure 1-1. Since temperature in these simulations is controlled through a kinetic thermostat that uniformly removes heat from the atoms of the system without relying on a radiative or conductive process to cool the sample from the surfaces in, this cooling process is not comparable to how samples would be cooled experimentally in a lab.

For small samples, the nominal cooling rate was 5K/ps. In larger samples, atoms did occasionally approach one another too closely, and were repelled with a high energy, despite the repulsive term in the Equation 1-1. This high velocity repulsion caused other close interactions of atoms, repeating the process, causing the program to crash. Although the repulsive portion of the equation decreased the likelihood of this happening, the probability of such an event was non-zero, and with enough atoms in the system, at least one instance occurred. To avoid the problems associated with this condition, a smaller timestep was used for the larger samples, and a lower initial temperature was used.

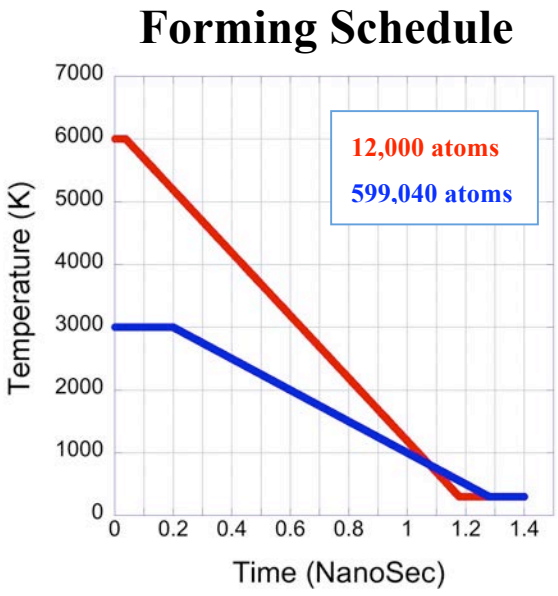

Figure 1-1: The initial forming procedure for small and large-scale glass simulations is shown here.

These samples contained a very small number of atoms when compared to the population of a physical sample. With just the sample box previously described, a large percentage of the atoms would be affected by the surfaces, and very little bulk structure would be produced within the sample. This problem was addressed through the use of periodic boundary conditions.[12] Images of the sample box were placed all around the original to form an infinite lattice that encapsulated the formed sample. As atoms moved in the sample, their images moved in all the surrounding images as well. Any atom that moved out of the box during the simulation was replaced by an image atom moving into the box from the opposite side. In this way, no surfaces were created, and the sample formed could be viewed as a bulk material despite its small physical size.

5. Terminology and Analytical Techniques

A number of commonly used terms exist within the scientific glass community to describe the structure of glass, and these terms will be used throughout this work. The basic structural unit of a silica glass is the silica tetrahedron. This unit consists of a single silicon atom, bonded to four surrounding oxygen atoms. Each of the oxygen bonded to the central silicon is, in turn, bonded to another silicon, which is the center of another tetrahedron. In this ideal situation, the oxygens are referred to as bridging oxygens (BO), and the silicon tetrahedron is known as a Q_4 unit. If an oxygen of the silica tetrahedron is not bonded with another silica tetrahedron, it is called a non-bridging oxygen (NBO), and the tetrahedron containing this NBO is a Q_3 unit. For each oxygen on the tetrahedron that is non-bridging, the subscript of the Q unit is decreased until a Q_0 species is produced, completely separated from the rest of the network structure. These terms can also be applied to non-silica systems, where the main building block of the glass is in tetrahedral coordination. NBO content and the population of different Q_N units found in a sample can be used to describe the connectivity of a glass structure.

Distribution functions are used in this work to describe the structure of the glass samples examined. A pair-distribution function (PDF) details the average number density of type *j* atoms around type *i* atoms, as found through a radial scan out from all atoms *i* in three dimensions. Information gathered is only as a function of radial distance, and position information is discarded, producing only one-dimensional information. For

a given pair of atoms, *i j*, the bond distance between them may be determined by the location of the first peak in the pair-distribution function, and the width of the peak indicates the distribution of different bond-lengths for this pair in the system.

Although glasses contain no long-range order in the way that crystals do, they do contain medium- and short-range order.[21,48] One way of systematically characterizing the medium range order of glass structures is through analysis of the silicon-oxygen rings formed in the structure. Silica tetrahedra in the structure share corners with one another through bridging oxygens, and link together to form rings within the structure. Although a silica tetrahedron may be involved in any number of rings throughout the structure, only primitive rings, or those which follow the shortest path from one tetrahedron, to another, and back to the original tetrahedron, are of analytical value and presented as results. Again, this technique can be used with other glass compositions in addition to silica.[21,22]

Chapter Two – The Structure of Sodium Silicate and Sodium Aluminosilicate Glasses

1. Introduction

Because of its compositional simplicity, silica glass has been the choice of many researchers for initial simulation work.[24,25,28,29,36-38,49-68] Despite the ease of simulation, silica glass is not a characteristic glass, behaving in an anomalous manner under a number of different conditions. Further, because of its high melting temperature and the need for extreme purity of raw materials, silica glass is a relatively expensive glass to form, and is not the first choice for most consumer goods. Although silica glass is compositionally simple, and is a good first step when addressing complex new concerns such as addressing artifacts of simulation or working with new sample geometries, computational studies of more chemically complex glasses are necessary.

Soda added to a pure silica glass acts as a flux to lower the temperatures required for glass melting from a prohibitively expensive temperature greater than 2000°C to a more reasonable value below 1600°C.[6] A lower melting temperature requires significantly less energy to achieve and maintain, and the subsequent wear on the furnace tank and refractory is less severe, allowing for longer runs before repair or replacement of the equipment. These differences make the addition of sodium to a silica glass a choice of economy. However, the changes to the glass are not confined to those convenient and economical. The addition of sodium to a silica glass changes many chemical properties of the glass, the most severe of which is chemical durability. Sodium silicate glass degrades easily in water, when compared with silica, and is unsuitable for containers, window glass, or any other application that would require the glass to maintain its properties while exposed to liquid water or a humid atmosphere.

Alumina is one of many materials that can be added to a sodium silicate glass to bring the properties of the glass closer to that of silica glass. Alumina increases the chemical durability of the material while only mildly increasing the melting temperature.[6] A silicate glass including sodium and aluminum may be more economically feasible to make than pure silica glass, while maintaining many of the original properties of that

glass. For these reasons, among others, sodium and aluminum are often found in combination in commercial glasses.

The bulk structures of sodium silicate and sodium aluminosilicate glasses have been studied using computer simulation in previous work.[21,68-70] Typically these simulations have been small in size, containing from several hundred[70] to three thousand[21] atoms. Simulated structures have been found to agree with experimental data, but generally show that the samples may have an elevated fictive temperature.

In this work, sodium and aluminum have been added to silica glass, forming compositions of $(X)Na_2O$-$(100-X)SiO_2$, with X= 7, 10, 15, 20, 25, 30, 35, and $25Na_2O$-$(Y)Al_2O_3$-$(75-Y)$ SiO_2, Y= 5, 10, 15 20, 25, 30, 32.5. Hereafter, these compositions will be referred to as XNa or YAl. System sizes varied slightly with composition, but most samples formed contained approximately 12000 atoms. The structure of these glass samples has been examined and compared to other simulations and to experiment, to determine if the samples are characteristic of the intended glass compositions.

2. Sodium Silicate and Aluminosilicate Glasses

The addition of sodium to the compositionally simple silica glass is a natural step in the progression of structural complexity. As sodium is added to the glass, non-bridging oxygens are formed, and the connectivity of the structure is decreased. This is illustrated in Figure 1-1.[6,71] In all illustrated figures, bridging oxygens are assumed unless labeled as NBO.

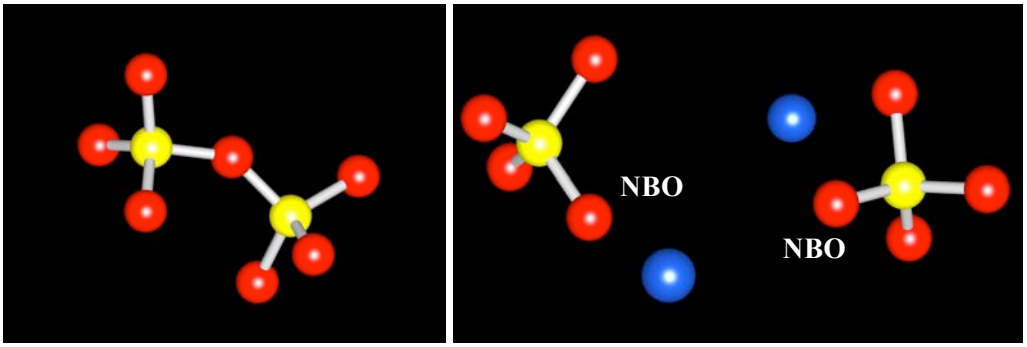

Figure 2-1. The breaking of a Si-O-Si bond with the addition of sodium is shown here.

As the Q_4 silica tetrahedra become Q_3 units, they are less connected to the structure. From this, it is expected that as the sodium content of the glass increases, the rings of tetrahedra found in the glass should increase in size. The NBO content of the glass should increase proportionally with sodium content, and the bond-lengths and angles may change and distort as the structure is disrupted. In glasses that contain a large amount of sodium, the sodium atoms in the system cluster together forming a sodium-rich region.[21]

Aluminum atoms, added to a sodium silicate glass in quantities less than 5%, are found in the structure in silica-rich regions, in four-fold tetrahedral coordination. A sodium ion is associated with each aluminum tetrahedron to balance local charge, and this is shown in Figure 2-2.

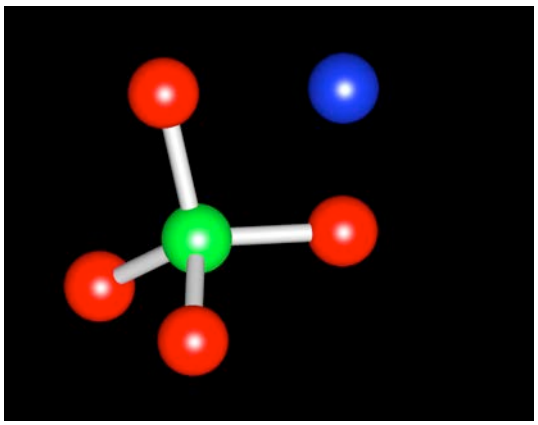

Figure 2-2. This image shows aluminum acting as a glass network former with an associated charge-balancing sodium ion.

As the aluminum content of the glass increases from 5% to 10%, the glass adopts a transitional structure,[72] where a continuous aluminosilicate glass is formed, replacing the modified random-network structure of alkali-rich and silica-rich regions in the glass. Above 10%, the structure can be described as a fully continuous aluminosilicate glass.

Each aluminum added to the structure can be thought of as adding back a bridging oxygen that the sodium in the structure had turned into a non-bridging oxygen. When $Al_2O_3/Na_2O = R = 1$, theoretically, all non-bridging oxygens in the structure should be re-

coordinated back to bridging oxygens, all aluminum should be in tetrahedral configuration, as glass formers, and all sodium should be associated with an aluminum tetrahedron. Beyond that value of R, the aluminum could either go into octahedral coordination, or triply bridged oxygen may be formed, with a single oxygen shared between three glass formers.[6,71]

It is expected that additional aluminum in the glass should increase the connectivity of the structure, decreasing the average ring size and number of non-bridging oxygens.

3. Ring Structure

The population of rings of differing size for sodium silicate and sodium aluminosilicate glasses formed in this study is shown in Figures 2-3 and 2-4.

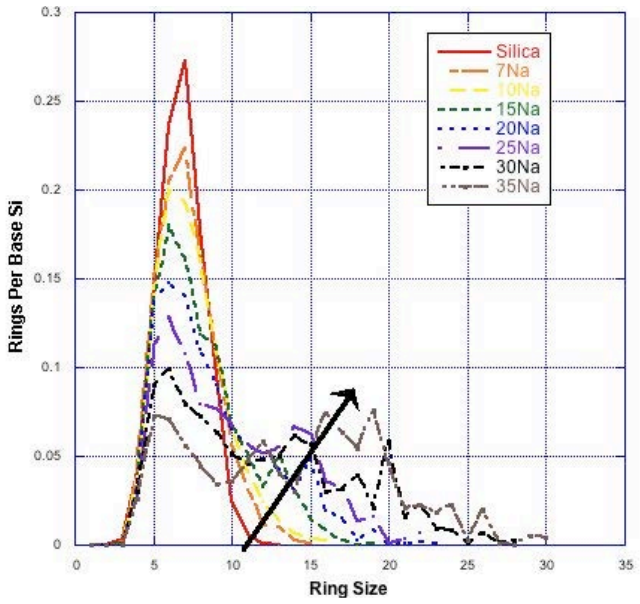

Figure 2-3. Ring size distribution for sodium silicate glasses are shown here. The arrow indicates the direction of increasing sodium content in the glass.

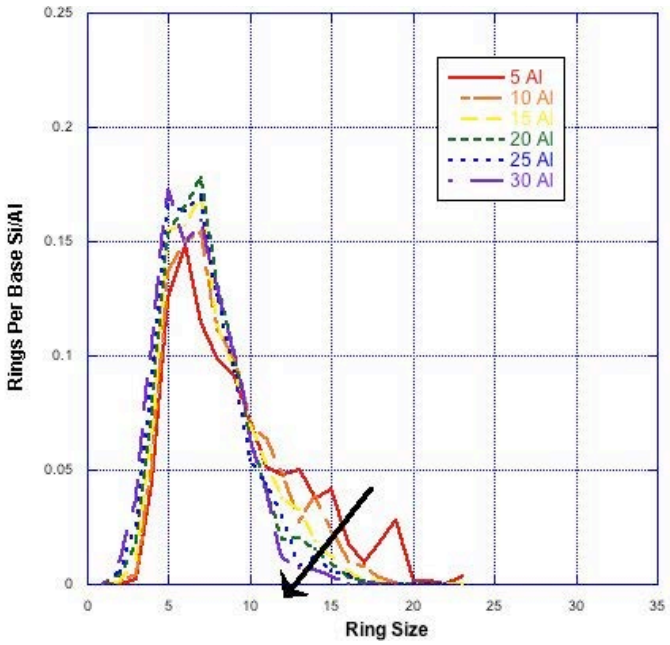

Figure 2-4. Ring size distribution for sodium aluminosilicate glasses are shown here. The arrow indicates the direction of increasing aluminum content in the glass.

Pure silica glass, with no modifiers or other glass formers, consists primarily of six- and seven-membered rings, although rings of larger and smaller size can be found within the structure as well. Ring size can be linked directly to the number of non-bridging oxygens found in the structure. As sodium content in sodium silicate glasses increases, the ring size distribution shifts to include larger rings. As aluminum content in the sodium aluminosilicate glasses increases, the rings become more interconnected, and the ring size distribution tightens again to consist primarily of six- and seven-membered rings. This behavior agrees well with theoretical understanding and other studies of ring size distribution[21,73] in the glasses examined.

4. Oxygen Coordination

In addition to medium-range order, glasses also possess short-range order, with predictable distances between bonded atoms and characteristic angles between sets of bonded atoms. Species which are fully connected into the silica glass structure are bridging oxygens, connected to two silicon atoms, and Q_4 units, which are silica

tetrahedra terminating in four bridging oxygens. As the connectivity of the structure is reduced, the number of non-bridging oxygen and Q_n species other than Q_4 increases. Figure 2-5 shows the changes in the number of non-bridging oxygen found in the sodium silicate and aluminosilicate glasses as a function of composition.

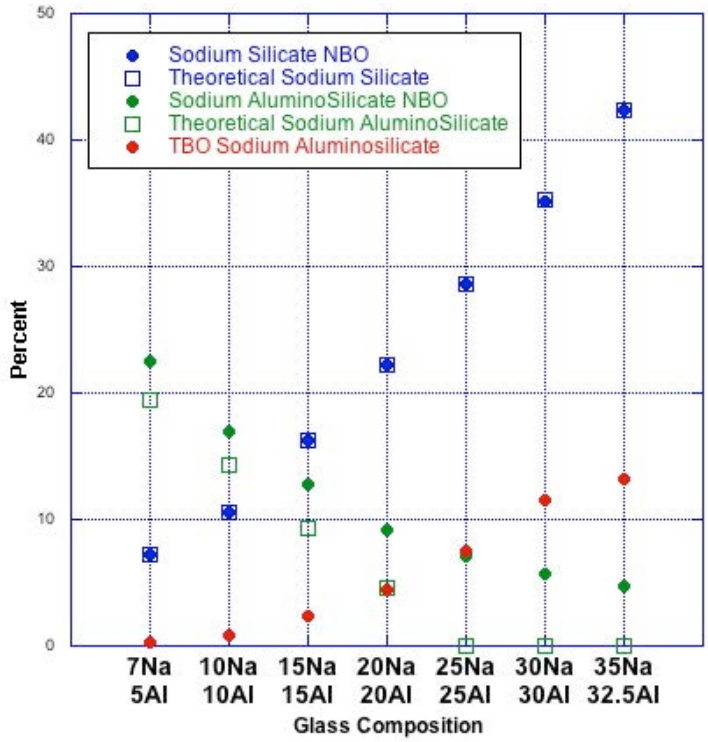

Figure 2-5. Non-bridging and triply-bridged oxygen content in the systems are shown here, given as a function of composition.

In sodium silicate glasses, the only oxygen species found were bridging and non-bridging. Since the number of non-bridging oxygens in the structure is the same as the number of sodium ions, theoretical percent non-bridging oxygen is easily calculated.[6,71] The percent non-bridging oxygen found in the simulated glasses matches well with the theoretically predicted values.

The calculated NBO content in the simulated sodium aluminosilicate glasses studied does not agree as well with the theoretical content of non-bridging oxygens which should be in the system. A significant number of non-bridging oxygen remain at R=1, and before that point, triply-bridged oxygen have been found within the system.

Although the simple theory does not suggest this behavior, it has been noted in other MD analysis of sodium aluminosilicate glasses.[69,70] The presence of triply-bridged oxygen in a glass with an R value less than 1 is balanced by the persistent high presence of NBO in the system.

Triply-bridged oxygen in the structure initially consist primarily of oxygen coordinated to 2 silicon and 1 aluminum atoms, as indicated by the ratio of peak heights in the pair-distribution function shown in Figure 2-6.

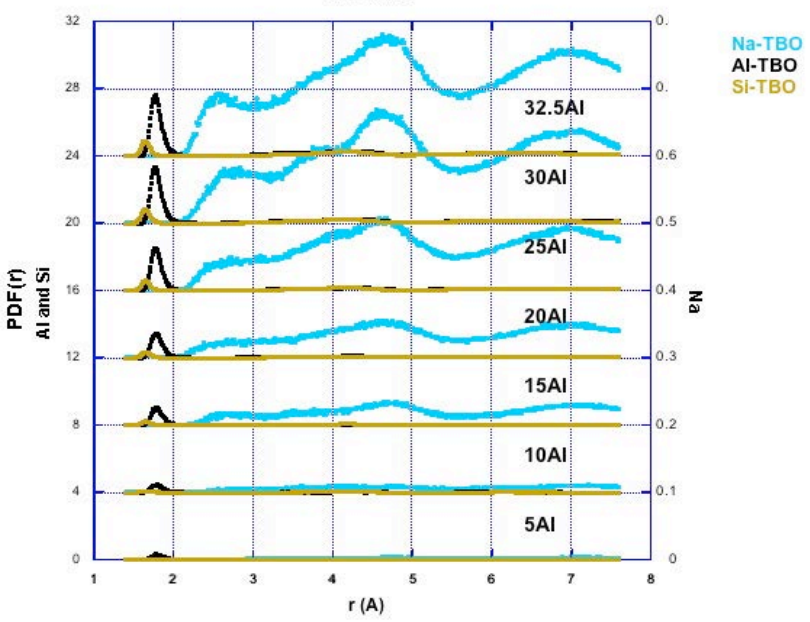

Figure 2-6. Pair-distribution functions for triply-bridged oxygen are shown here.

This initial configuration is likely due to the scarcity of aluminum in the low-aluminum-content glasses. As aluminum content in the glass increases, the triply-bridged oxygen is primarily connected to 2 aluminum and 1 silicon atom. This coordination results in an excess negative charge, which requires a sodium in the vicinity for charge balance. The emergence of a clear Na-TBO peak as the aluminum content increases indicates the prevalence of the 2Al-1Si clusters over 2Si-1Al clusters.

5. Q_n Species

The proportion of different Q_n species in the glass is also a measure of the connectivity of the structure because it describes how each tetrahedron is linked to other system tetrahedra. The Q_n species, as a function of composition, are shown for the sodium silicate glasses in Figure 2-7, and for sodium aluminosilicate glasses in Figure 2-8.

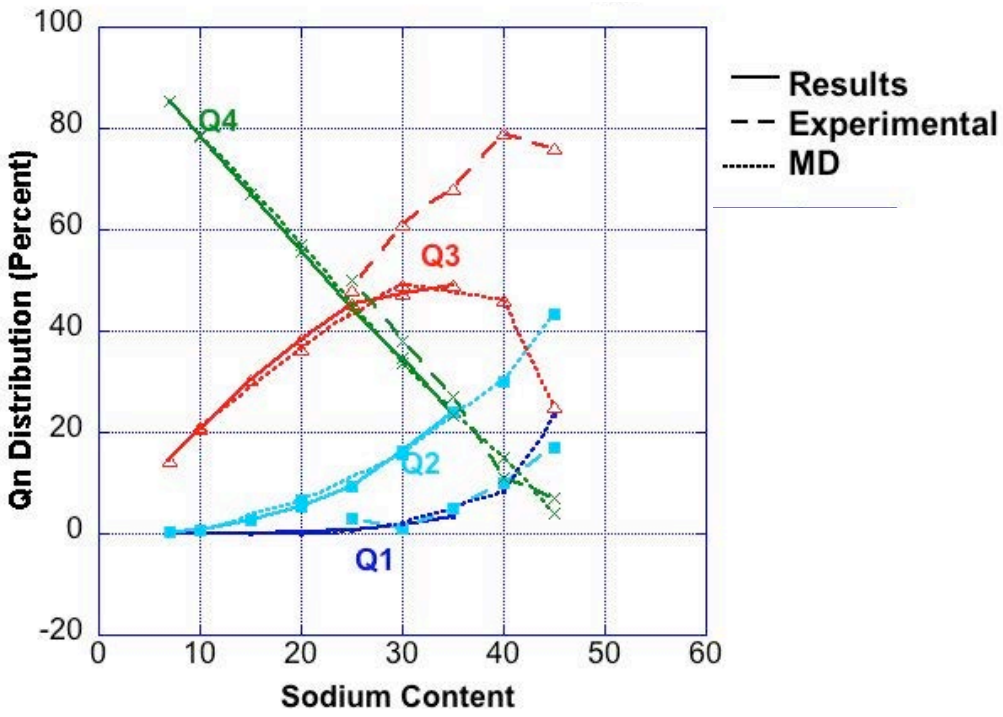

Figure 2-7. Q_n species in the glass for different compositions of sodium silicate glasses are here compared with other MD work[21] and experiment.[74]

The number of different Q_n species found for varying compositions agrees well with another computational simulation[21], but both simulations have values that differ somewhat from those reported in experimental study.[74] This simulation showed a significantly higher number of Q_2 units, and a slightly higher concentration of Q_4 units than determined by experiment, while the number of Q_3 units was lower than expected. In

experiment, glasses that have been cooled more quickly than by traditional experimental cooling and annealing processes show a lower number of Q_3 species while the number of Q_2 and Q_4 species increases.[75] Thus, since a similar shift has been observed in these simulated glasses, it is clear that the structure of the sample also has a higher fictive temperature than a traditionally annealed glass sample.

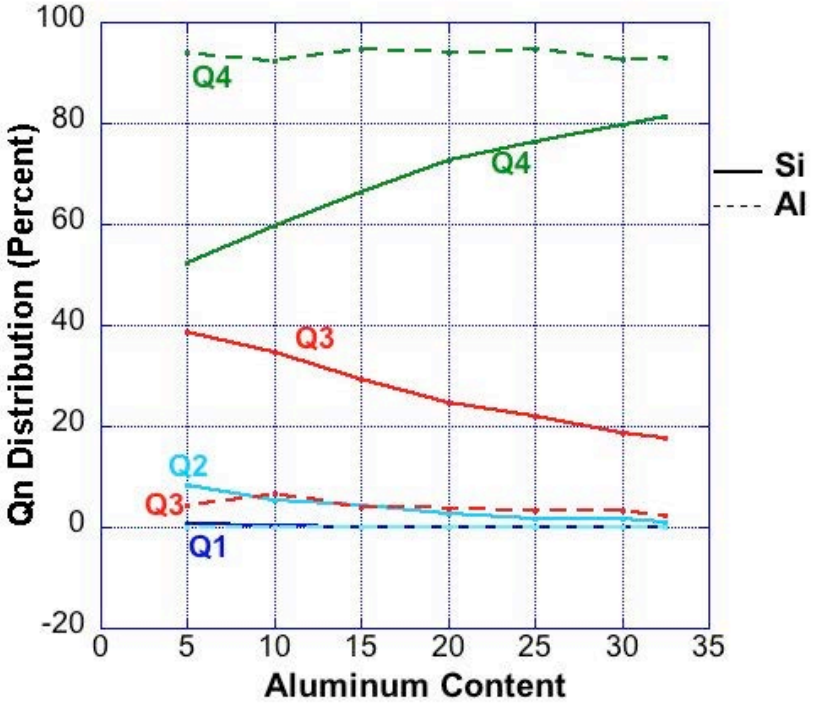

Figure 2-8. Qn species in the glass for different compositions of sodium aluminosilicate glasses, are presented here for both silica and alumina tetrahedra.

From Figure 2-8, it is clear that a majority of the non-bridging oxygens in the structure are associated with silicon, rather than aluminum. Note the relatively constant value of aluminum Q_4 species in the glass with changing composition, in comparison with the increasing number of silicon Q_4 units. It is also expected that these values are shifted slightly from what would be found in experiment in the same manner that Figure 2-5 illustrates, but a lack of experimental data revealing Q_n species in these glasses forbids comparison.

6. Bond-lengths

Bond distances can be illustrated using pair-distribution functions. Examples of pair-distribution functions, for a range of sodium silicate glasses, are shown in Figure 2-9.

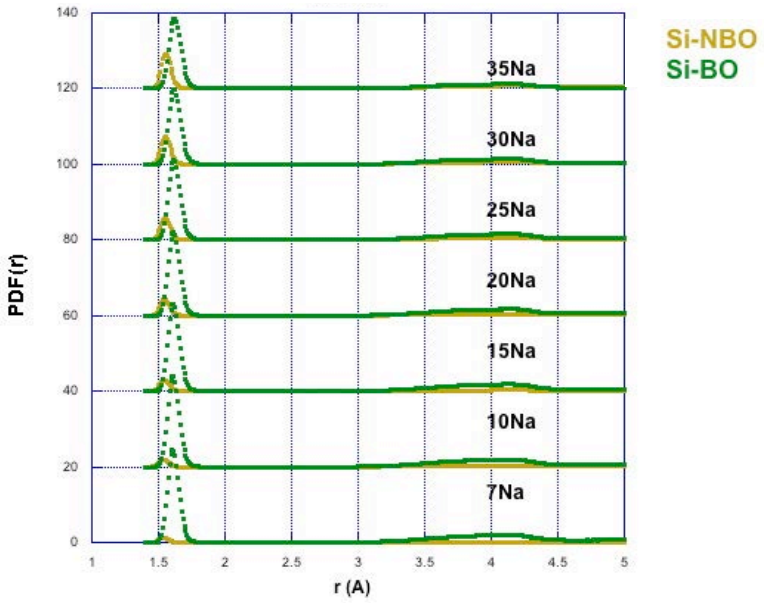

Figure 2-9. This figure shows the pair-distribution functions for silicon and oxygen in the sodium silicate glasses examined.

In the case of Figure 2-9, the pair-distribution has been deconvoluted to separate the bond distances of the bridging and non-bridging oxygens. Prior to this analysis, a pair-distribution function (PDF) was calculated for all Si-O pairs, and the maximum bond distance for the pair was established. Using that maximum bond distance, oxygens could be identified as bridging or non-bridging and were sorted and labeled as such for analysis of the pair-distribution function. As non-bridging oxygen content in the glass increases with increasing sodium content, the Si-NBO peak grows, while the Si-BO peak shrinks. The Si-NBO peak in the PDF shifts to longer bond distances for glasses with increasing NBO content, while the peak position of the Si-BO pair remains largely unchanged. Average bond-lengths for the sodium silicate and sodium aluminosilicate glasses are given in Tables II-I and II-II.

Table II-I. Average Bond-Lengths for Bond Pairs Within the Sodium Silicate Glasses, Ranges Indicate Values from 7Na to 35Na

Species	Sodium Silicates (Å)	Experimental (Å)
Si-NBO	1.53-1.55	
Si-BO	1.61-1.62	
All Si-O	1.605-1.615	1.611-1.622[76]
Na-NBO	2.25-2.30	
Na-BO	2.55-2.51	
All Na-O	2.35-2.36	2.36-2.388[Cited in 21]

The oxygen ions around a sodium ion form a coordination polyhedra, and in this sense the two are bonded, although the bond is usually not displayed graphically in depictions. The average distance between sodium and oxygen is presented in Tables II-I and II-II. Using experimental techniques, researchers cannot easily distinguish between bridging and non-bridging oxygens, and so the data presented are for all of these bonded pairs regardless of their connectivity within the system. A clear difference can be seen in the bond-lengths of bridging oxygen versus non-bridging oxygen. Si-NBO pairs have a much shorter bond-length than Si-BO pairs, for all compositions. Bridging oxygens are being attracted to silicon atoms on both sides, and so find an equidistant point between the two that is slightly stretched from the separation distance of a single Si-O pair. When an oxygen ion is non-bridging, its effective charge is larger, and it is pulled closer to the bonded silicon atom.

An increase in the number of non-bridging oxygens in the structure is noted with increasing sodium content, which would suggest a shortening of the Si-O bonds, yet the overall bond-length increases slightly with increasing sodium. This can be explained through examination of the overall trends of the system with increasing sodium content. As the sodium concentration in the glass increases, there is a lengthening of both the bridging and non-bridging oxygen bonds with silicon, and so, although there is in an increase in the number of shorter Si-NBO bonds, it is not enough to decrease the average length of all Si-O bonds.

Sodium in the structure is primarily associated with non-bridging oxygen for charge balance, and so the trend to increase the bond distance with increasing sodium concentration seen in the Na-NBO pair is mirrored in the overall Na-O bond-length change with composition. Sodium clustering, as mentioned previously, is noted in these glasses. The pair-distribution function for sodium-sodium pairs is shown in Figure 2-10. The strong peak at 3Å suggests a tendency of the sodium in the glass to cluster. This agrees with the results found by Du and Cormack.[21]

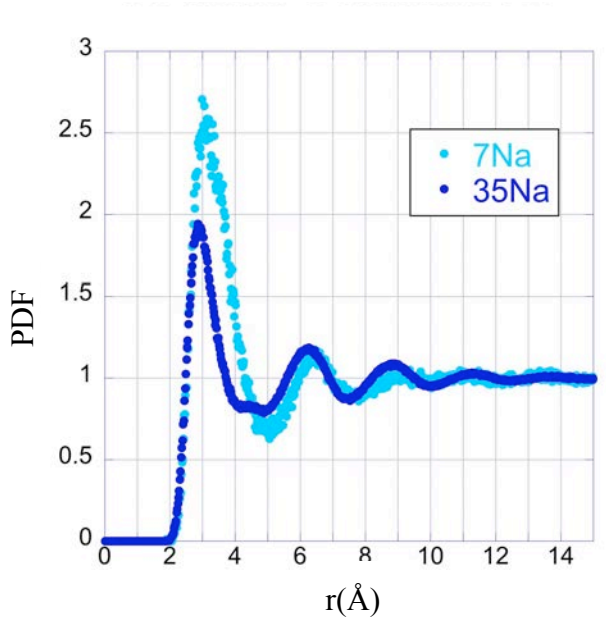

Figure 2-10. This figure shows the pair-distribution function for sodium-sodium pairs in the 7Na and 35Na glasses.

Table II-II. Average Bond-Lengths for Bond Pairs Within the Sodium Aluminosilicate Glasses, Ranges Indicate Values from 5Al to 32.5Al

Species	Sodium Aluminosilicates (Å)	Another MD Study (Å)[70]
Si-NBO	1.55	
Si-BO	1.61-1.60	
Si-TBO	1.65-1.64	
All Si-O	1.60	1.59-1.61
Na-NBO	2.28-2.30	
Na-BO	2.52-2.40	
Na-TBO	2.91-2.53	
All Na-O	2.36-2.41	2.4-2.6
Al-NBO	1.665-1.674	
Al-BO	1.75-1.72	
Al-TBO	1.80-1.77	
All Al-O	1.73	1.74-1.75

Compositional trends in the bond-lengths of the aluminosilicate glasses are less clear than with sodium silicates. In the case of both the silicon and the aluminum, no trend is noted over the compositional range studied in this MD work, and only slight changes are reported from the other MD study cited.[70] Although there are changes in the bond-lengths between glass-forming species and bridging and non-bridging oxygens, the changing proportions of the different species types negates this, resulting in no overall change. The sodium-to-oxygen distance was found to increase slightly, due to an increase in the number of BO and TBO in the system with increasing aluminum content.

7. Bond-angles

Bond-angles within the tetrahedra of these glass systems remained relatively constant for glasses of different compositions. These values are shown in Table II-III

Table II-III. Average Bond-Angles Within the Silica and Alumina Tetrahedra, for Selected Compositions

Sodium Silicates	**7Na**	**35Na**
BO-Si-BO	107°	106°
BO-Si-NBO	109°	109°
NBO-Si-NBO	112°	110°
O-Si-O	107°	109°
Sodium Aluminosilicates	**5Al**	**32.5Al**
BO-Si-BO	109°	108°
BO-Si-NBO	109°	109°
NBO-Si-NBO	111°	112°
O-Si-O	109°	109°
Sodium Aluminosilicates	**5Al**	**32.5Al**
BO-Al-BO	107°	107°
BO-Al-NBO	85°	111°
NBO-Al-NBO	88°	--
O-Al-O	107°	107°

The angles in these tetrahedra vary somewhat depending on the connectivity of the oxygens involved. The angle is widened when the oxygens are not connected to other tetrahedra, and angles tighten somewhat as the tetrahedra are more closely connected into the structure with bridging oxygen. The strained bond-angles seen in aluminum tetrahedra for glasses with small quantities of sodium are associated with small 2- and 3-membered rings in the structure. Although these values are starkly different from those seen in the fully coordinated tetrahedra, the number of alumina tetrahedra linked to non-bridging oxygen in the system is small, and the values do not have a noticeable effect on the average angle.

8. System Size Comparison for Sodium Silicate Glasses

As stated previously, the simulated structures in Chapter One contain a much smaller number of atoms than a physical sample would. Therefore, it is worthwhile to examine the validity of the structures in this study, in comparison with much larger systems, as possible, to see if they have produced a significantly large enough system to be representative. Using a BlueGene/L supercomputer, larger sodium silicate glass

samples, of 614,400 and 1,005,000 atoms, have been examined and compared with the structure of smaller sodium silicate systems.

The number of non-bridging oxygen in the system again mirrored the values predicted by theory as shown in Figure 2-5. The distribution of Q_n species was shifted slightly from experimental values, and bond-lengths and angles were found to agree with expected values, all agreeing with the results reported for smaller systems. The only difference of note between 12,000-atom systems and the larger half million and million atom systems was in the presence of unusually coordinated species. The population of these species in different glasses is shown in Table II-IV.

Table II-IV. Quantities of TBO and Five-Coordinated Silicon in the Glasses

% Defects		**x=7**	**x=20**	**x=30**
12000	*TBO*	0	0	0
	Si_5	0.042	0.017	0.001
614400	*TBO*	0.002	0.001	0.000
	Si_5	0.226	0.166	0.088
1005000	*TBO*	0.000	0.000	0.001
	Si_5	0.026	0.017	0.008

Although triply-bridged oxygen are seen in the sodium aluminosilicate glasses made of 12,000 atoms, they are not found in the smaller scale sodium silicate systems. The presences of these species can be explained by examining their positions within the sample box, illustrated in Figure 2-11.

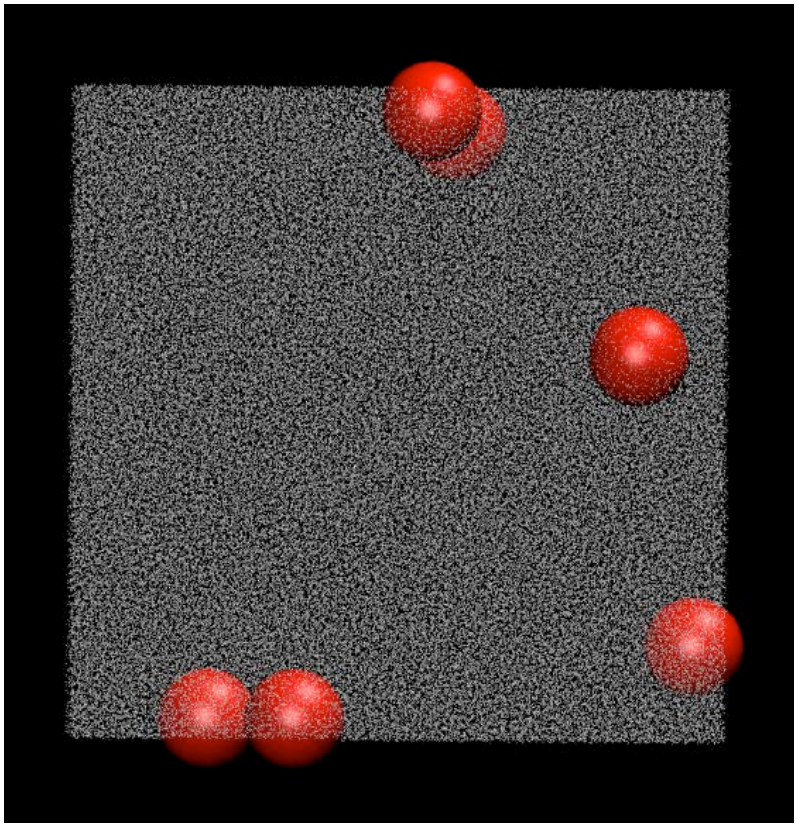

Figure 2-11. This figure illustrates the position of TBO in the 7Na glass sample, by showing them as large red orbs. Note that these TBO are found at the surface of the sample box. This sample contains 614,400 atoms.

The sample box in Figure 2-11 has been rotated to best illustrate that all of the TBO found in the system are found around the box edges. It is possible that these species are present, in part, because of the constraints of the periodic boundary conditions. Periodic boundaries require that any atom at the extreme left edge of the box will also be placed just beyond the right edge of the box. So these atoms must not only coordinate properly and interact with the atoms immediately surrounding them, but they are interacting with a number of images that are similarly constrained. Triply-bridged oxygen in the melt structure may have been unable to recoordinate into a more favorable configuration as the glass cooled, due to these constraints. Given that the percent of triply-bridged oxygen in the larger systems is so low, it is unlikely that any would show up in a system with only 12,000-atoms, even though triply-bonded oxygen are noted in the initial melt structure.

The presence of five-coordinated silicon in the system is a bit more troubling, but perhaps more easily explained. Five-coordinated silicon atoms are seen in the smaller simulations, but in much smaller quantities. Similar to the shifts seen in the Qn species population, the presence of five-coordinated silicon atoms indicates an elevated fictive temperature.

Overall, the structural features of these larger simulations are in good agreement with those observed for smaller systems, and the smaller systems can be considered as characteristic structures.

9. Conclusions

The sodium silicate and sodium aluminosilicate glasses formed in simulation show similar structural features to systems studied in other simulation work, and in experimental research. They differ from analysis of experimental samples only in displaying evidence of a slightly elevated fictive temperature, and so are analogous to samples of quickly quenched glass, rather than traditionally annealed samples. These glass samples have also been shown to be large enough to be considered representative structures.

Chapter Three – The Formation and Structure of Silica Fibers

1. Introduction

While a significant body of work exists on the study of the structure of bulk silica glass[14,15,19,34-37,52,61,62,66,68,77-96], and the structure of surfaces and surface interactions of silica glass using atomistic computational techniques, [25-29,49-51,54,55,59,64,67,97-101] little work has been done to examine the structure of silica fibers. Atomistic studies can be computationally expensive, as system size is increased to experimental ranges, but through the use of a BlueGene/L supercomputer, we have been able to simulate fibers up to 20nm in cross-sectional diameter. Fibers were formed with varying system size and cross-sectional geometry, and the surface structures of these fibers were examined.

2. Sample Formation

Traditional computational processes, as described in the Chapter One, were used to form bulk glass samples of varying sizes, with simulation boxes containing from 3000 to approximately 600,000 atoms, as shown in Table III-I.

Table III-I. Sample Shapes, Number of Atoms, and Dimensions

Fiber Shape	Number of Atoms	Approx. Dimensions (Angstroms)
Box	3,000	L=35 W=34 PD=36
Box	12,000	L=56 W=55 PD=56
Box	19,500	L= 65 W=65 PD=65
Box	599,040	L=202 W=202 PD=205
Cylinder	15,355	R=32 PD=65
Hexagonal Cylinder	20,784	R=40/43 PD=56

R= Radius L=Length W=Width PD= Periodic Depth

At this point, the bulk samples were periodic in the x, y, and z directions, with box images repeating around the sample. In order to create a fiber from the simulated bulk

structure, the periodic boundary conditions were manipulated. At least 20Å of extra space was added on either side of the box, in the x and y directions, leaving the z direction as continuously periodic. This produced individual fibers that were spaced far enough apart in the x and y directions to avoid any interactions between images, but still continuous in the z direction. Images of the separation of two hexagonal periodic boxes in the y direction through the addition of extra box space, and the final fiber, are shown in Figure 3-1.

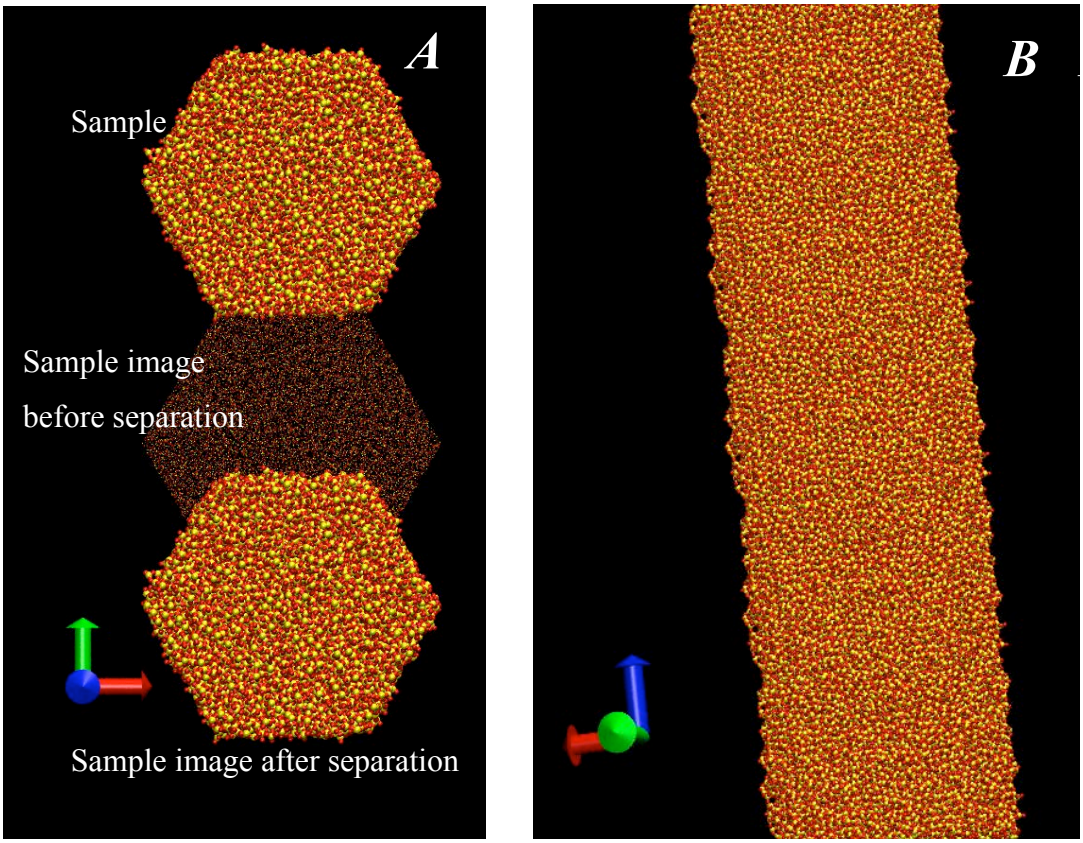

Figure 3-1. A) Hexagonal sample box and one of its y periodic images is shown here, before and after extra space has been added to the sample. B) The final fiber is shown here, periodic in Z.

Since DLPOLY can handle both square and hexagonal periodic boundary conditions, samples with these cross sections were formed directly. To form a fiber with a cylindrical cross section, a sample with cubic periodic boundary conditions was used,

and all atoms beyond a radius of 32 Å were removed. After the cylinder was cut from the cube, a monotonic layer of atoms at the surface of the cylinder was identified, and atoms were chosen randomly to be removed from this layer to balance the stoichiometry of the system. Finally, space was added to the box, as described before, to form the fiber.

3. Annealing

After the fibers were formed, the surface of the fibers were very highly disordered. This disorder is characterized by the presence of unusual structural defect species in the sample, such as non-bridging oxygens (NBO), under coordinated silica tetrahedra (Q_3 units), and under coordinated silicon atoms, $Si^{(3)}$. In order to allow some of these unusual species to re-coordinate back into the surface of the fiber, the sample was reheated to 2,500K, cut, and then held at that temperature for 250,000 timesteps. This process was used to allow the surface of the fiber to form as it would from a melt. The presence of these species, as a function of radial distance from the sample center, is shown in Figure 3-2, for the cylindrical fiber. The two lines on the graph show the change in the presence of these species, as the fiber is initially cut, and then after it was held at temperature.

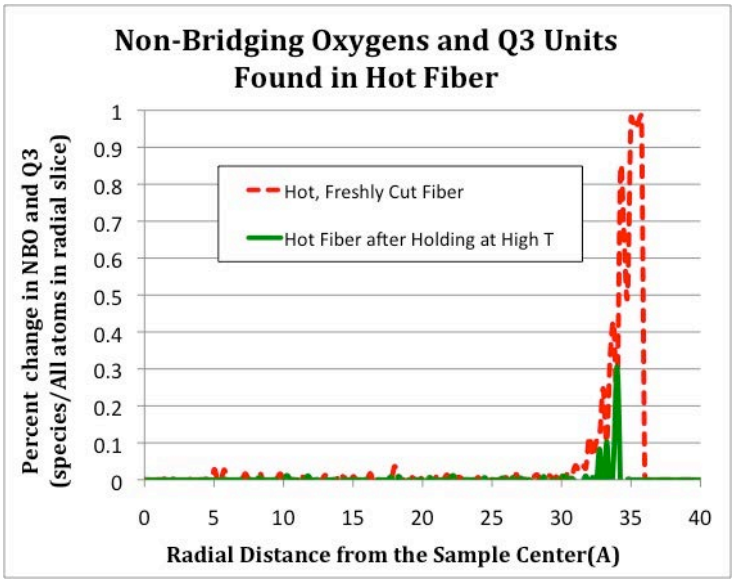

Figure 3-2. The presence of unusual species found in the cylindrical cut fiber is shown in this figure, before and after being held at high temperatures.

The decrease in the quantity of defect species and their movement inward towards the sample bulk after the hold at high temperature is related to the re-coordination of these species into more energetically favorable configurations. The percentages of several species found in the fiber at different stages of the forming process are shown in Table III-II, for the square fiber.

Table III-II. Unusual Species in the Square Fiber at Various Stages of the Forming Process

Forming Step	NBO	Q_3	Q_2	$Si^{(3)}$
Bulk Glass Sample	0.3 %	0.8 %	0.1 %	0.4 %
Hot Bulk Sample	0.6 %	1.9 %	0.3 %	1.2 %
Hot Cut Sample	4.0 %	10.6 %	2.3 %	7.3 %
Hot Annealed Sample	0.6 %	2.1 %	0.1 %	1.1 %
Cooled Final Fiber	0.7 %	2.2 %	0.2 %	1.3 %

From Table III-II, it is clear that a great deal of disorder is added to the system, specifically at the cut edges of the fiber, when it is separated from the bulk. Although a large number of these unusual species are recombined back into the structure in favorable ways by the end of the annealing process, a small portion of the disorder remains in the final sample. As suggested by Figure 3-2, these unusually coordinated species have been found primarily in the outer region of the fiber, defining a surface structure, as described in the next section.

4. Defining Surfaces

In the simulations of silica surfaces, the surface of a sample has typically been defined by the presence of unusually coordinated species.[24] The depth of a surface structure is determined by the population of these species, from the void outside of the sample to the interior structure. One surface defect that has been noted in simulated surfaces has been a bond-angle of 120°. A traditionally coordinated silicon tetrahedron has bond-angles of 109° between each set of O-Si-O atoms. When an O-Si-O bond-angle

of 120° is found in silica glass, it is usually associated with three-coordinated silicon atoms. Trioni et al.[64] found that a peak in the bond-angle distribution around 120° was found for the sample within 5Å of the surface. Similarly, Wilson and Walsh[27] found that the peak at 120° was not noticeable beyond 5.29Å. In an ab-initio MD simulation by Mischler, Kob, and Binder[28] a shift back to a bond-angle around 109° from more strained values was only apparent when they examined a sample which had a surface depth greater than 5Å. Based on three-coordinated silicon atoms, two-membered silicon rings, and non-bridging oxygen in the structure, among other unusual species, Du and Cormack[24] determined that the surface layer extended 5-10Å into the sample.

The concentration of OH that would be formed from the hydroxylation of these defect species on the surface was measured in experiment,[102] using temperature programmed static SIMS, and was found to be 2.6 sites/nm^2. Simulation work by Pantano[54] suggested that as many as 3.9 sites/nm^2 could exist, while work by Du[24] suggested that a range of OH densities were possible, from 4.5 to 2.5 sites/nm^2, depending on the species that are assumed to react to form OH.

Material surfaces can also be defined by the variation in density, as the sample is viewed in thin slices as a function of surface depth.[97] Using this depth profiling technique, Yuan and Cormack found that silica glass had a surface depth of approximately 10-15Å. The surfaces in their study were fracture surfaces, produced from the tensile failure of a bulk glass, and were expected to be rougher than the clean, cut, outer surface of the fibers studied in this work.

5. Fiber Surfaces, examined as a function of system size

a. Defect Population

To define the surface depth in the simulated fibers, 0.5Å thick radial slices were taken from the center outward, mimicking the shape of the cross section, and the number of unusual species found in each slice was noted. For the purposes of defining a surface layer, unusual species included non-bridging oxygen, triply-bridged oxygen, any silicon atom not connected to four oxygens, and any Q species other than Q_4. Although a fiber was made with 3,000 atoms, it became deformed as a result of the annealing process.

The irregular cross section of the finished fiber did not readily lend itself to radial slices a uniform distance from the fiber surface, and so analysis of the surface depth of the 3,000-atom fiber is not included here. The relative sizes and final cross-sectional shape of these fibers are shown in Figure 3-3.

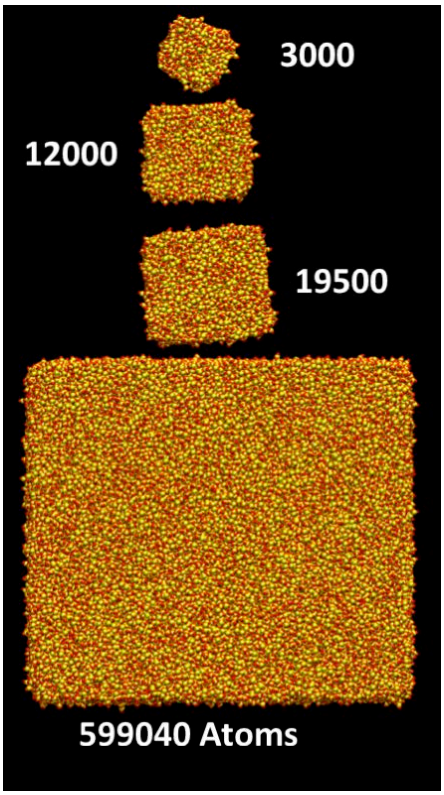

Figure 3-3. This is a cross-sectional view of the differently-sized box-shaped fibers.

Figures 3-4, 3-5, and 3-6 show the presences of the defect species as a function of distance from the box center, for the three differently-sized fibers examined. In each case, the fibers showed a distinctive surface structure that was different from the bulk, where more of the unusual species were found.

In each of these figures, both the number of unusual species and the percent of unusual species for each radial slice of the fiber are shown. This is done to illustrate the point that although some of these unusually coordinated species are found within the bulk, they do not represent a majority of the atoms in the radial slice. This is especially evident in Figure 3-6, where we have a large number of atoms in each slice because of

the system size, and thus, a large number of unusually coordinated atoms in the bulk of the material. However, when the population of unusual species is viewed as a percentage, it is clear that a surface structure has been formed away from the center of the box.

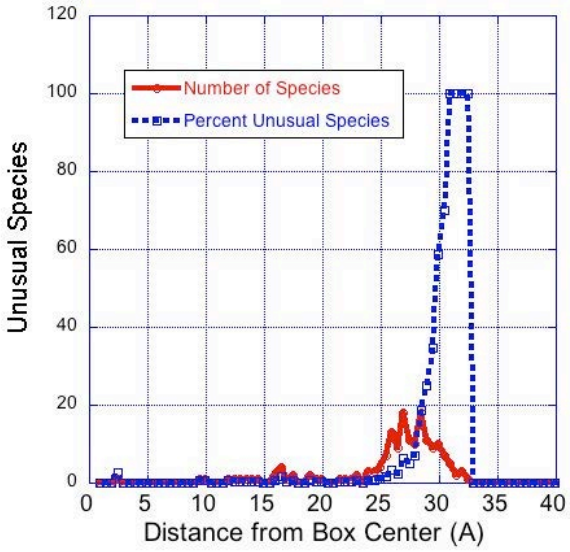

Figure 3-4. Unusual species found in the 12,000-atom box-shaped fiber are shown here as a function of distance from the sample center.

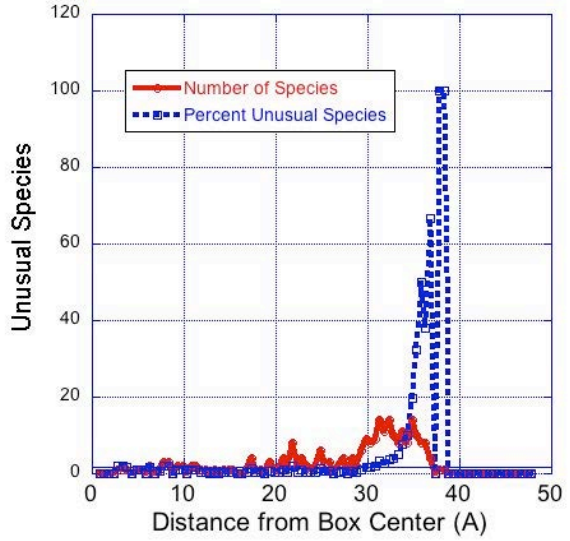

Figure 3-5. Unusual species found in the 19,500-atom, box-shaped fiber, are shown here, as a function of distance from the sample center.

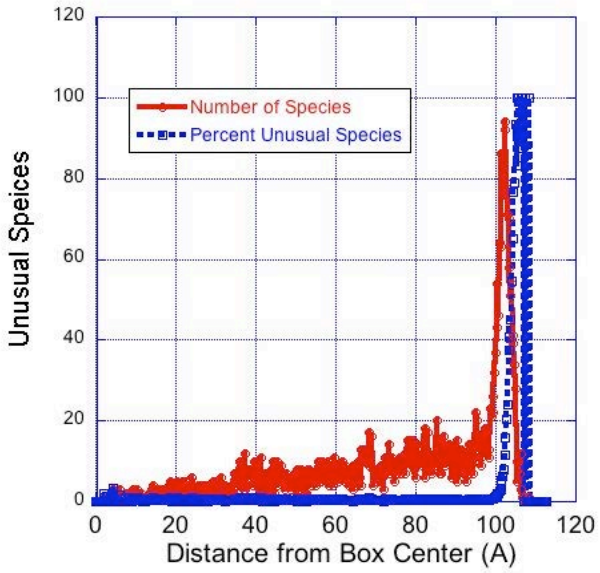

Figure 3-6. Unusual species found in the 599,040-atom box-shaped fiber are shown here as a function of distance from the sample center.

Using the number of unusual species in each half Å slice of the fibers, the surface layers of these three fibers are shown in Figure 3-7. The approximate depths of these surface layers are 9.3±0.2, 9.5±0.6, and 8.4±0.7Å, for the 12,000-, 19,500-, and 599,040-atom fibers. The variation in surface depth of these samples is small, and primarily within a single standard deviation. This does not suggest a trend based on sample size. Since the fibers were free to move in the sample box during the annealing, both the 12,000 and 19,500 box fibers shifted slightly. The resultant fibers shown in Figure 3-3 still retain their box cross-sectional shape but are angled away from the initial box formed parallel to the x and y axes. Thus the radial slices of the boxes, which are taken parallel to the axes, have provided a slightly wider surface layer than would have otherwise been found. Since the 599,040-atom fiber did not shift away from the original parallel position to the axes, the surface structure is slightly thinner.

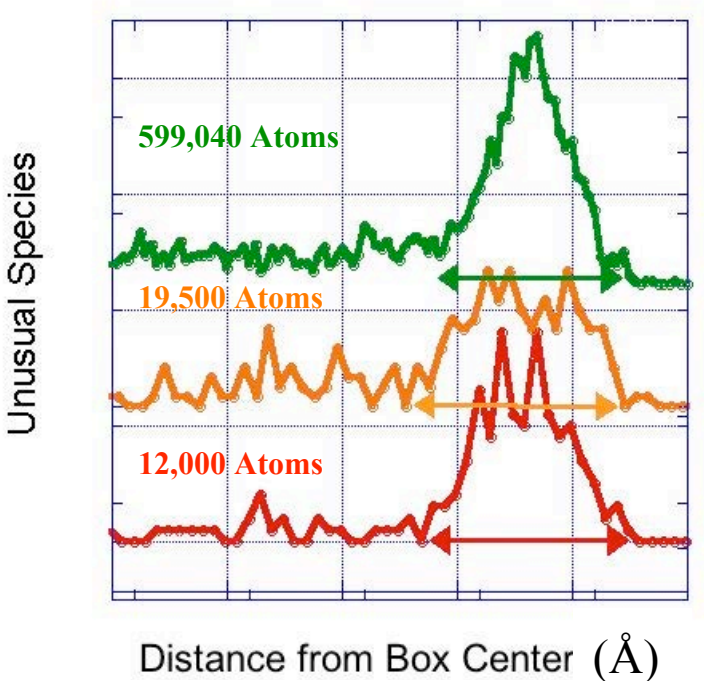

Figure 3-7. The number of unusual species forming the surface of the three differently-sized fibers with square-cross-sections is shown here. Surfaces were found to be 8.4±0.7, 9.5±0.6, and 9.3±0.2Å thick, respectively, for the fibers of increasing size.

b. Density Variation

In addition to a spike in defect species population, low-density areas may also be used to define the surfaces. The densities of these samples, given as function of the depth into the box, are shown in Figures 3-8, 3-9, and 3-10. The surfaces of these fibers, as given by their density variation from the void outside the sample to bulk clearly shows a trend with sample size. The surface thicknesses seen for the samples were found to be 5.7, 8.7, and 11Å, for the 12,000-, 19,500-, and 599,040-atom samples respectively.

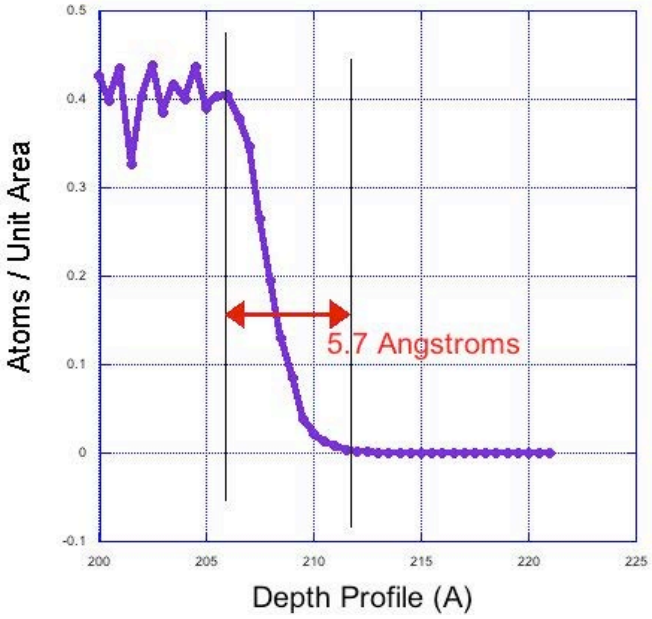

Figure 3-8. The density of the structure, as a function of depth profile for the 12,000-atom fiber.

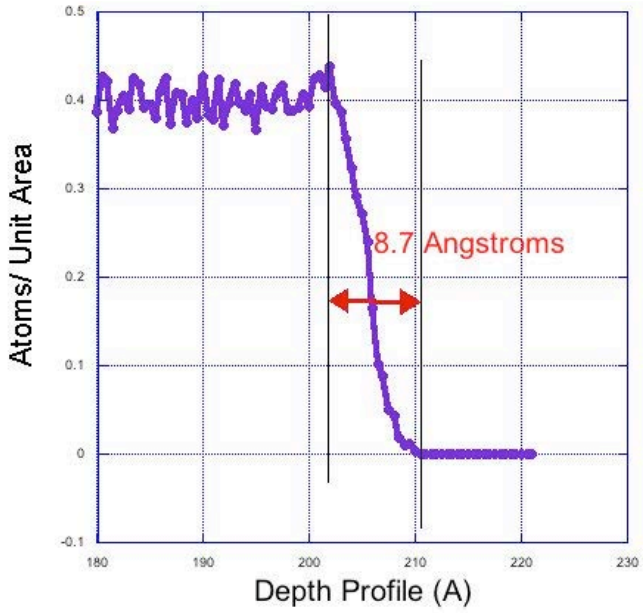

Figure 3-9. The density of the sample, as a function of depth profile for the 19,500-atom fiber.

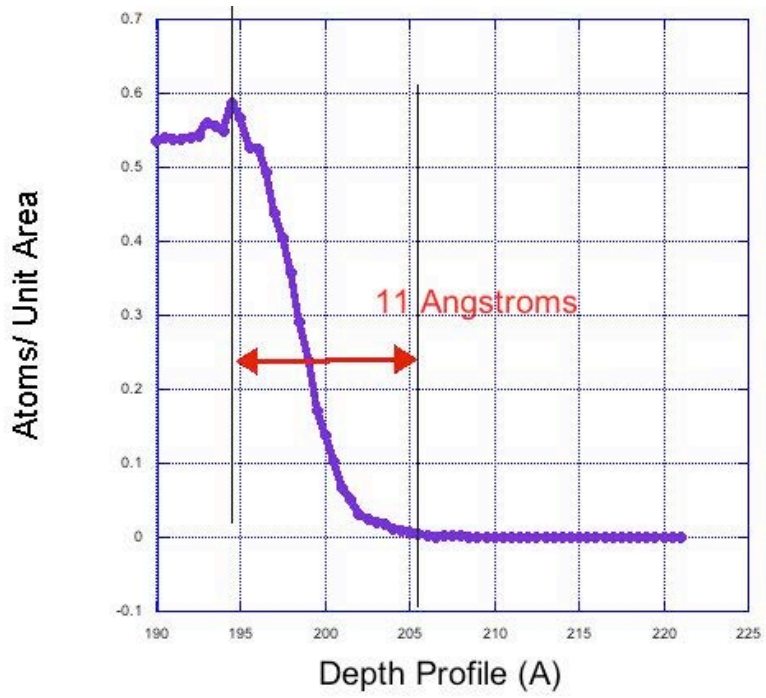

Figure 3-10. The density of the sample, as a function of depth profile for the 599,040-atom fiber is shown here.

Any variation in this analysis due to the slight rotation of the sample would be expected to increase the surface thickness of the two smaller fibers slightly, and so this trend to thicker surfaces in larger samples is clearly not due to the small sample rotation. From the 12,000- to 19,500-atom system, the increase in surface thickness is 0.4 Å/1000 atoms. From the 19,500-atom system to the 599,040-atom system, the increase in surface thickness is only 0.00497 Å/1000 atoms. The increase in surface thickness with increasing sample size tapers off for larger systems. For fibers of experimental size, the surface layer is expected to be thicker than found in these simulations, but only marginally so, due to this decreasing size dependence.

6. Fiber Surfaces, Examined as a Function of Cross-Sectional Shape

In addition to this examination of fibers of different sizes, fibers with differing cross-sectional geometries were also examined. As indicated in Table III-I, fibers were

made with box, hexagonal, and circular-cross-sectional shapes. Cross-sectional views of these fibers are shown in Figure 3-11.

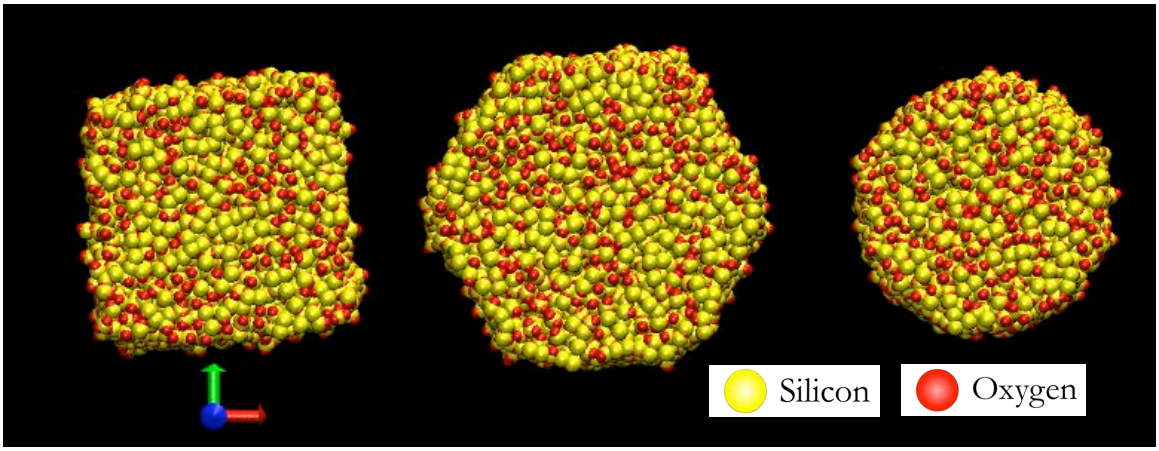

Figure 3-11. Cross-sectional views of differently-shaped fibers are shown here.

a. Defect Population

The populations of defect species in the samples were examined in radial slices, mimicking the cross-sectional shape of each sample. Figures 3-12, 3-13, and 3-14, show the defects in these fibers for the square, circular, and hexagonal fibers respectively.

For each of the fibers (with differing cross-sectional area), we again see a distinct surface layer, indicated by the higher population of unusual species near the surface. Although some of these defect species are found within the bulk of the sample, they do not account for a majority of the atoms in the slice. These bulk defects were present in the structure before the fiber was formed, as evident from Table III-II.

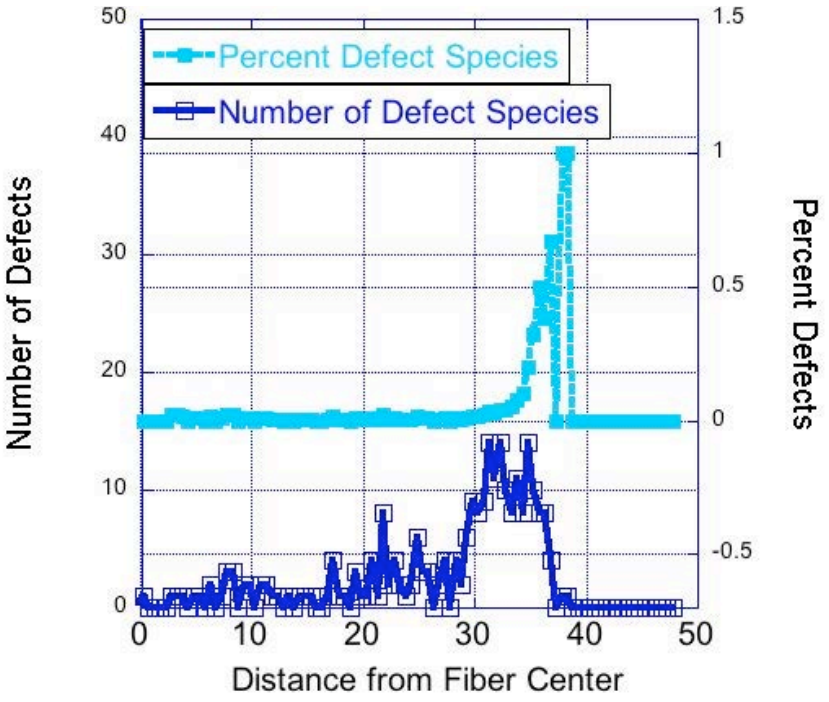

Figure 3-12. The defect species in the fiber with a square-cross-section are shown here.

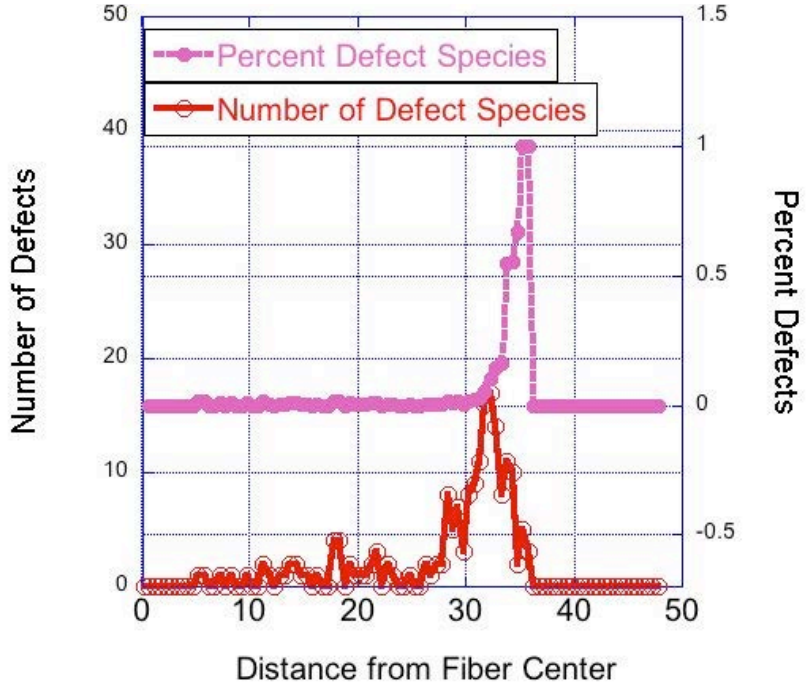

Figure 3-13. The defect species in the fiber with a circular-cross section are shown here.

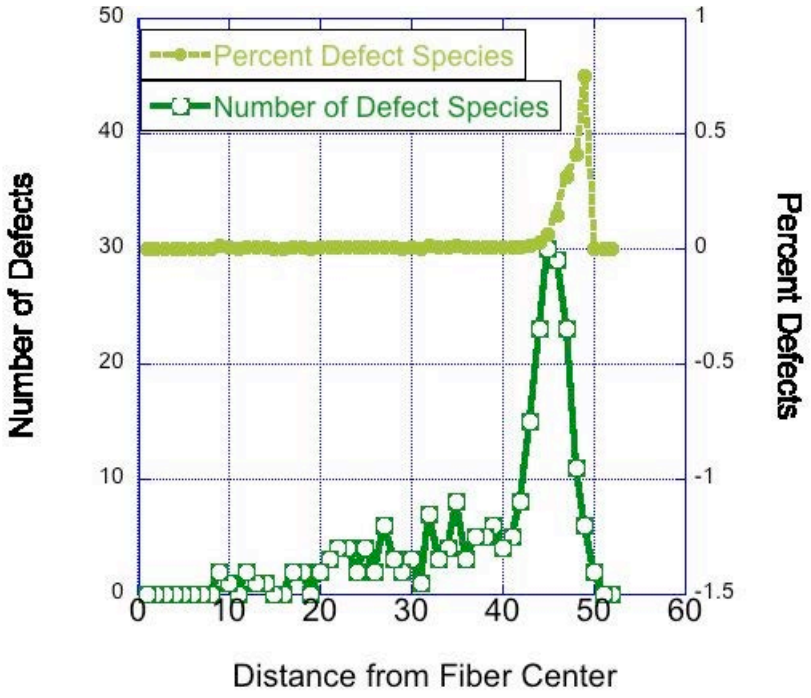

Figure 3-14. The defect species in the fiber with a hexagonal-cross section are shown here.

A comparison of the three fibers together, shown in Figure 3-15, reveals that the square, circular, and hexagonal fibers have surface thicknesses of 9.7±0.7, 9.4±0.9, and 10.6 ±0.5Å, respectively. These values were calculated from ten measurements of the full peak width of each sample. The apparently thinner surface layer in the circular fiber is again likely due to the slight rotation of the hexagonal fiber before analysis. Rotation of the circular fiber did not affect the match between the radial slice shape and the fiber shape. No significant difference is seen in the surface layer thickness for these samples of varying cross-sectional shape, as measured by the presence of unusual species.

The concentration of these defect species in the glass, including small-membered rings, if fully converted to OH in a wet atmosphere, would lead to a surface with 2.7, 2.6 and 2.4 OH/nm^2 for the square, circular, and hexagonal fibers respectively. This agrees well with the results of the experimental work referenced earlier that suggested an OH concentration of 2.6/nm^2.

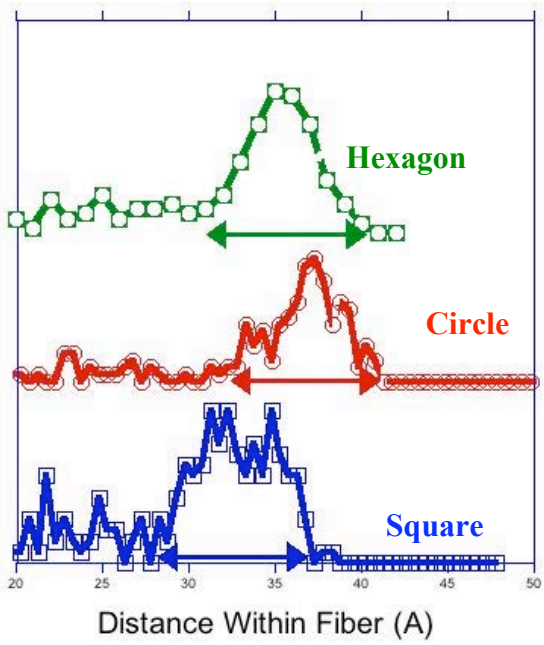

Figure 3-15. The number of unusual species forming the surface of the three differently-shaped fibers is shown here. Surface thicknesses were found to be 9.7±0.7, 9.4±0.9, and 10.6 ±0.5Å, thick, for the square, circular, and hexagonal fibers, respectively.

b. Density Variation

The variation in the sample densities as a function of radial distance from the center of the fiber was also studied for these fibers with different cross-sectional shapes. The surface layer thicknesses for the fibers, as defined by the area with these density variations, are shown in Figure 3-16. Because of the distinct difference seen between the 12,000-atom and the 19,500-atom fibers, it is clear that differences in the number of atoms in each of these systems is expected to influence their surface thickness. The trend in density variation is expected to produce increasingly thicker surface layers in the circular, square, and hexagonal fibers, since they contain 15,355, 19,500, and 20,784 atoms, respectively.

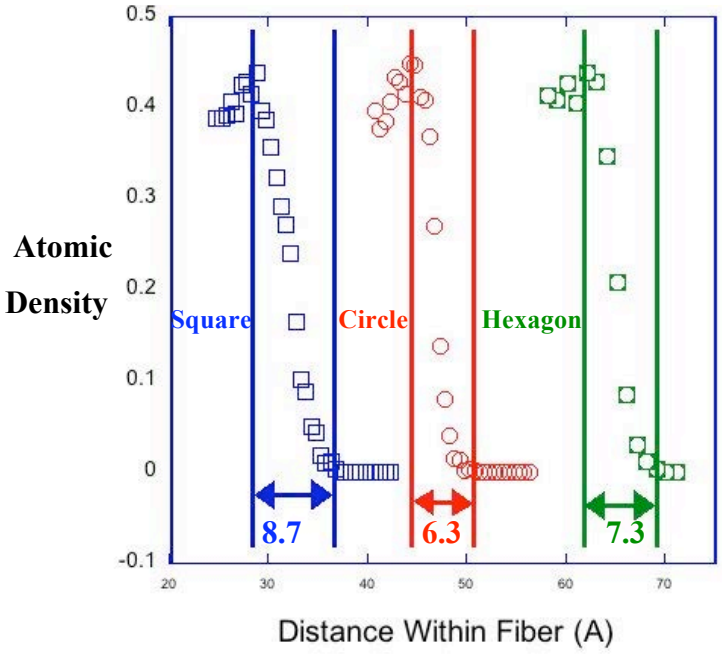

Figure 3-16. Sample surfaces defined by density variation for fibers with different cross-sectional shapes are shown here.

As expected, the circular fiber has the smallest surface thickness as defined by density fluctuations, at 6.3Å, but the square fiber has a larger surface thickness than the hexagon, despite the hexagon having a slightly larger number of atoms. This might be attributed to several different causes. The rotation of the square away from parallel to the axes may be more significant than any rotation of the hexagon, increasing the surface thickness measurement of the square fiber more than the hexagonal fiber. It may also be that the shape of the hexagon, with internal angles of 120˚ instead of the sharp 90˚ angles of a square acts to better hold the atoms in place when exposed to a vacuum. This may also suggest that the smaller surface thickness of the circle is due not only to the smaller number of atoms, but also to the interactions between neighboring atoms on the surface.

7. Conclusions

Silica glass fibers of different sizes and cross-sectional shapes have been formed and examined in simulation. A distinct surface layer has been formed in each sample studied, and can be identified by the presence of unusually coordinated species and

variations in sample density. Although no significant differences were observed in the surface thickness of fibers with varying size, based on defect species, they were found to have an increasing surface thickness with system size, when density variation was considered. This change in surface thickness is significant for smaller systems, but appears to taper off for larger systems.

Some small variation in surface layer thickness is seen with varying cross-sectional shape based on density variation within the sample, although again, no variation is found the based on the presence of defect species. The less-dense surface layer of the sample appears to be thinner for samples without sharp angles, decreasing in thickness from the square to hexagon to circular samples. This would suggest that more naturally shaped samples, such as the circle and hexagon, produce fibers that retain the ideal density of the material throughout the structure.

Chapter Four – Breaking the Silica Fibers Under Tension

1. Introduction

Computational modeling is an excellent technique for examining the process of quick failure in a brittle material because the small timestep used in simulation makes it possible to observe individual bonds breaking as cracks are formed. A number of computational studies have been conducted to examine the failure of silica glass under stress.[37-39,52,57,58,63,65,66,103-107] A majority of these studies have used bulk glass, where periodic boundary conditions are used to avoid surface effects.[37,38,52,57,58,103,106,107] Failure was found to occur through the coalescence of nano-scale voids inherent in the structure of the glass.[38,103,107]

Other researchers have studied the progress of a crack as it propagates through the material from an initial void or notch in the surface of a simulated sample.[61,65] In these notched studies, cracks were found to proceed through the glass due to the growth and coalescence of nanoscale damage. Small cavities were found to open up in the crack path, up to 20nm ahead of the crack tip.

This work is the first to examine the failure process and crack initiation in pristine silica fibers using Molecular Dynamics simulations.

2. Straining Process

After the silica fibers were formed, as described in Chapter Three, they were strained under tension until failure, to examine the fracture process as it occurred. Rather than apply stress and measure the resultant strain, as is commonly done experimentally[71,108-110], computationally, the simulation box and atoms were strained, and then the stress of the system was calculated from the new atomic positions, forces and velocities. Strain in a single dimension is calculated as the change in length of the sample in that direction divided by the original length, and is reported as a percent change. In the straining process, an expansion of sample box in the z-direction is followed by a small shift of z coordinate of each atom, away from z=0 at the box center. Interatomic forces are calculated for these new positions and the atoms are free to shift in the x, y, and z

directions in order to move to energetically favorable positions. Since the sample box contains empty space in the x and y directions, as explained in Chapter Three, the sample can contract naturally in the unstrained directions, as a response to the strain applied in z.

The samples were strained at a rate of 0.001/picosecond. Although this strain rate is fast relative to experimental strain rates, it is one of the slowest that has been used in computational simulation of fracture of silicate glasses.[103] The use of a fast strain rate is required by the computational resource constraints. Fracture of the sample typically occurred within 300,000 timesteps, and the runs were allowed to continue to 600,000 timesteps, the equivalent of 1.2 nanoseconds in real time. Real time between recalculation of forces, a single timestep, is 2 femptoseconds, and so, to run these calculations for a single second of real time, would require 5×10^{14} iterations of the calculations, and is too computationally expensive to be feasible using current technologies.

3. Choice of System Size

From the results of Chapter Three, we noted that a difference in surface structure can be seen for systems of differing size. The largest changes to the surface structure are seen when the sample size is still small, and the surface thickness increases rather significantly, from 5.7 to 8.7Å , as sample size increases from a 12,000-atom system to a system containing 19,500-atoms. The increase in surface layer thickness from the 19,500-atom system to a system with 599,040-atoms is considerably less, only 2.3Å thicker, although the larger sample is over 30 times the size of the smaller one. The dependence of surface layer thickness on system size clearly becomes less significant as the size of the sample is increased. A half-million-atom system is formed in approximately 67,404 CPU hours, 136 times the number of hours required to form the 12,000-atom system.

The12,000-atom system represents a significant change in the depth of surface structure from the half-million-atom system, and so, these samples are not acceptable for further, despite the large computational savings. The approximately 20,000-atom systems, however, represent a compromise between computational economy and

reasonable surface structure. The samples chosen to examine the failure of silica glass fibers under tension are shown in Table IV-I.

Table IV-I. Fiber Samples to Undergo Tensile Failure

Fiber Shape	Number of Atoms	Approx. Dimensions (Angstroms)
Box	19500	L= 65 W=65 PD=65
Cylinder	15355	R=32 PD=65
Hexagonal Cylinder	20784	R=40/43 PD=56

R= Radius L=Length W=Width PD= Periodic Depth

4. Elastic Properties

As the systems were strained, they deformed elastically before failing in a brittle manner. Graphs of the stress-strain curves for each of the fibers are shown in Figures 4-1, 4-2, and 4-3, for the square-, circular- and hexagonal-cross-section fibers, respectively.

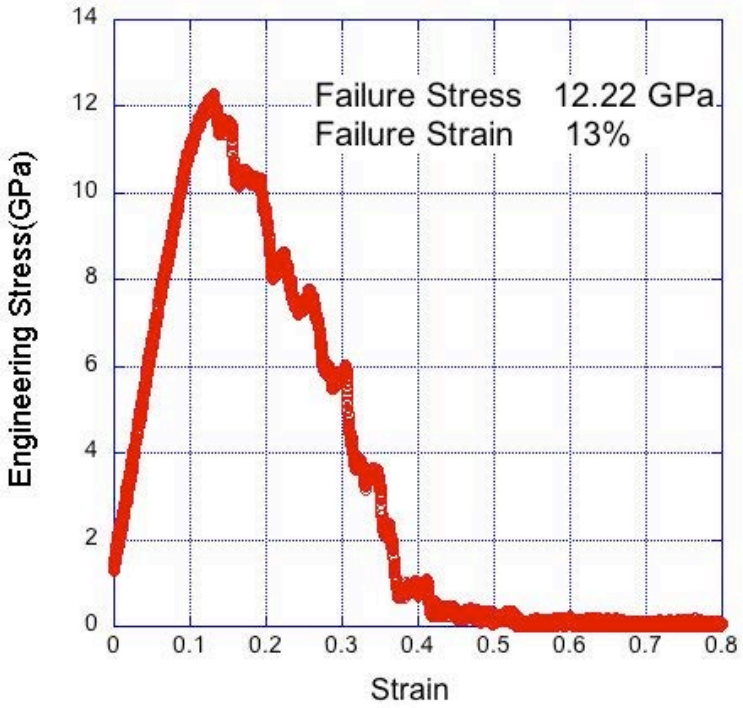

Figure 4-1. A stress-strain curve for the 19,500-atom square-cross-section fiber.

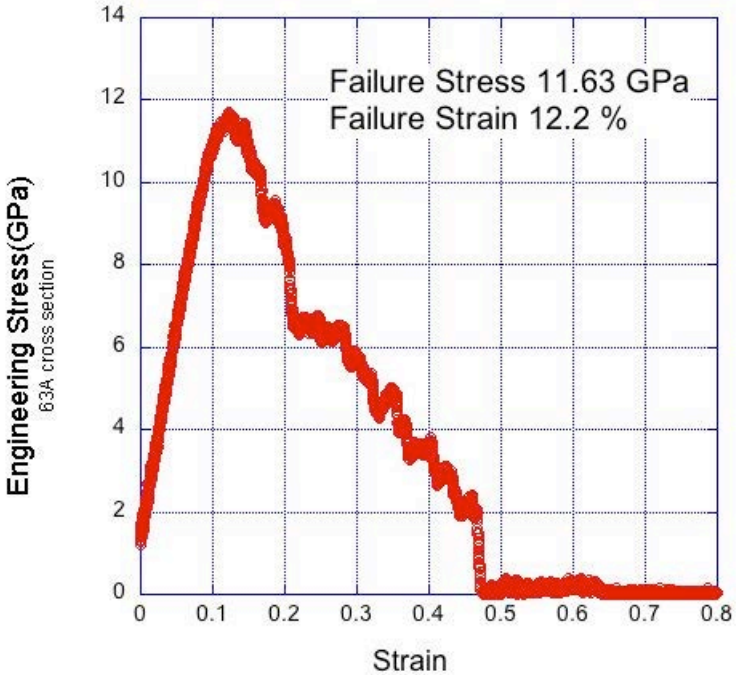

Figure 4-2. A stress-strain curve for the 15,355-atom circular-cross-section fiber.

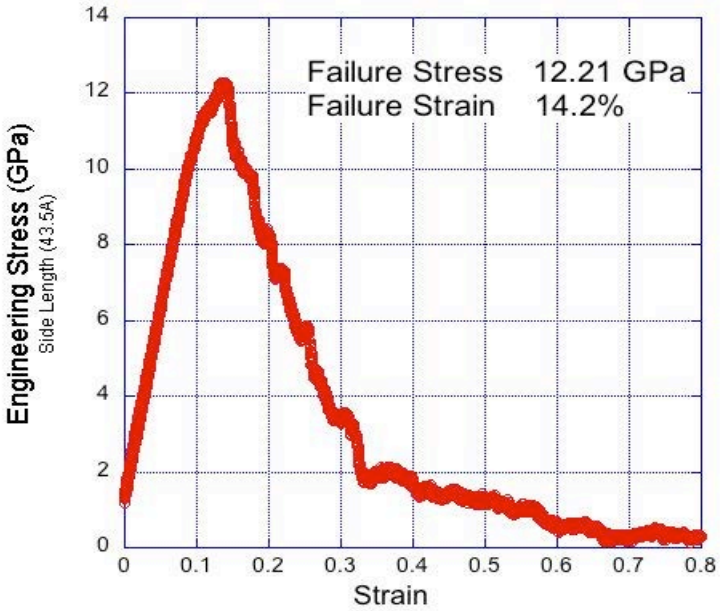

Figure 4-3. A stress-strain curve for the 20,784-atom hexagonal-cross-section fiber.

The values of failure stress and failure strain found in this work are compared with the results of simulations of bulk glass and experimental study in Table IV-II.

Table IV-II. Failure Stress, Failure Strain, and the Elastic Modulus for the Fibers, Previous Bulk Silica Work, and Experimental Study

Property	MD Bulk Silica[103]	Experimental Fiber[109]	MD Fiber Square	MD Fiber Circular	MD Fiber Hexagonal
Failure Stress(GPa)	10.8	12.77	12.21 ± 0.04	11.63 ± 0.05	12.21 ± 0.06
Failure Strain(%)	15.3	17.73 ± 0.16	13.04	12.20	14.17
Young's Modulus (GPa)	69.9	71.99 ± 0.65	90	86	86

The stresses at failure for these systems agree reasonably well with the results of experimental study shown here, and are closer to the experimental values than the results of a similar study using bulk silica glass. Failure strains for these fibers were lower than any values found either by the experimental study or the MD simulation of bulk silica, leading to a value of Young's modulus that was higher than expected. Although the stress-strain curve shows apparently linear behavior as the fiber is initially deformed, non-linear behavior is clearly noted as the strain of the system is increased and the fiber approaches failure. In concordance with this behavior, also noted by Gupta and Kurkijan,[111] Young's modulus was calculated by fitting a third-order polynomial to the curve, up to a strain of 13%

5. Fracture Surface Structure

When each fiber is broken under tension, two new surfaces are formed in addition to the surface already present around the circumference of the fiber. These new surfaces have not been annealed, and thus the atoms that are unusually coordinated are given no extra energy with which to recombine back into the structure in more energetically favorable ways. Although the surface areas created are small when compared with the

fiber surface, this fresh fracture surface significantly increases the number of defect species in the system. An example of this increased population of defect species is shown in Table IV-III.

Table IV-III. Defect Species Population Before and After Failure for the Square Fiber

Sample	NBO	Q3 Units	3-Coordinated Silica	Q2 Units
Initial Fiber	0.55%	1.42%	0.80%	0.25%
Failed Fiber	1.53%	3.85%	2.25%	0.72%

6. Distortion of Structure Under Strain

Under strain, it is expected that the structure of the glass will undergo some distortion. Changes to the Si-O bond-length and intertetrahedral bond-angle, Si-O-Si, throughout the fracture run for the three fibers are shown in Tables IV-IV, and IV-V. In these tables, box elongation is shown up to 78%, at which point the fiber is completely broken.

Table IV-IV. Changes to the Average Si-O Bond-Length for the Fibers Under Tension

Box Elongation in Z	Square	Circle	Hexagon
0.0 %	1.618 Å	1.619 Å	1.619 Å
4.0 %	1.623 Å	1.624 Å	1.623 Å
8.3 %	1.630 Å	1.631 Å	1.630 Å
12.7 %	1.636 Å	1.635 Å	1.635 Å
17.3 %	1.634 Å	1.633 Å	1.633 Å
22.1 %	1.632 Å	1.629 Å	1.630 Å
34.9 %	1.625 Å	1.629 Å	1.622 Å
49.1 %	1.620 Å	1.620 Å	1.621 Å
64.8 %	1.620 Å	1.621 Å	1.620 Å
78.5 %	1.618 Å	1.620 Å	1.619 Å

Table IV-V. Changes to the Average Si-O-Si Bond-Angle for the Fibers Under Tension

Box Elongation in Z	Square	Circle	Hexagon
0.0 %	150.1°	150.0°	150.5°
4.0 %	150.6°	150.7°	151.1°
8.3 %	151.4°	151.3°	151.7°
12.7 %	151.6°	151.2°	151.9°
17.3 %	150.4°	150.0°	150.7°
22.1 %	149.6°	149.1°	149.8°
34.9 %	148.0°	148.4°	148.1°
49.1 %	147.1°	146.8°	148.3°
64.8 %	146.9°	146.7°	146.9°
78.5 %	147.1°	146.7°	147.4°

For each sample, distortion is seen due to the tensile strain acting on the fiber. The Si-O bond-lengths increase as the fibers are strained, but then return back to the initial values, as the fibers are broken. Failure of the fiber is initiated at approximately 12-14% strain, and so the bond-lengths begin to decrease, indicating elastic recovery, after this point. As the fracture is completed by 70% elongation, the bonds are no longer extended due to stress.

The changes that occur to the intertetrahedral bond-angle are somewhat different. At zero strain, the intertetrahedral bond-angle of 150° matches the peak position seen by Du and Cormack in their surface structures of silica glass.[24] Looking at the progression of the Si-O-Si angle as the sample is strained, we do see initial distortion associated with the stressing of the structure, but this distortion does not disappear with the failure of the fiber and the release of systemic stress. The final Si-O-Si bond-angle is significantly changed from its initial value. This is probably due to the formation of small rings on the freshly formed fracture surface.

With failure of the 19,500-atom square fiber, the number of two- and three-membered rings increases from approximately 0.8% to 1.5%, and a similar increase is

noted for the fibers with other cross-sectional geometries. This partially accounts for the bond-angle shift.

Small-membered rings are also found on the surface in small quantities, in addition to the defect species mentioned in Table IV-III. These rings have much tighter bond-angles than those found in five- and six-membered rings. An illustration of two and three-membered rings is shown in Figure 4-4, with the bond-angles noted.

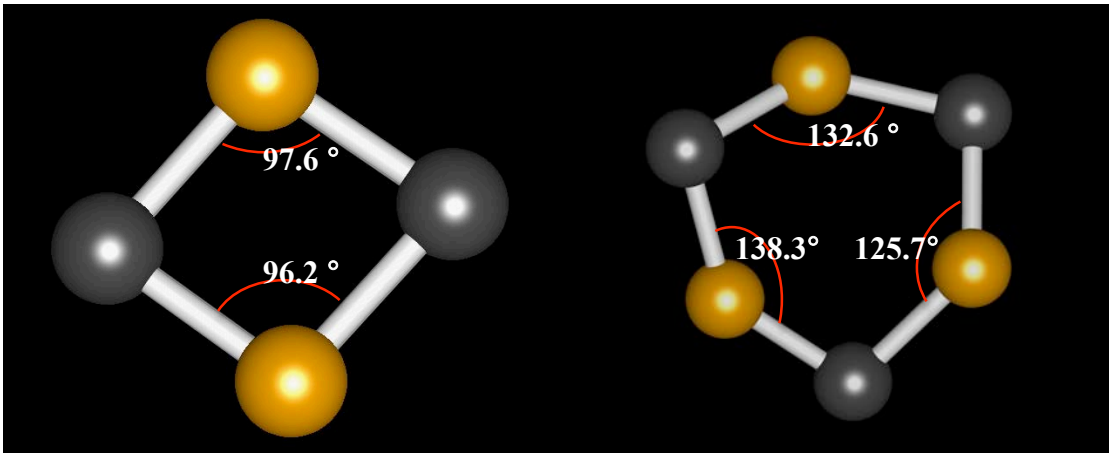

Figure 4-4. Examples of two- and three-membered silica rings are shown here, with the Si-O-Si bond-angles indicated.

The rest of this shift in Si-O-Si bond-angle is accounted for by the formation of triply-bonded oxygen on the new fracture surface. The concentration of triply-bonded oxygen found in the initial fiber was 0.19%, but after failure the concentration increased to 0.49%. An example of a triply-bonded oxygen is shown in Figure 4-5, and shows that the Si-O-Si bond-angles associated with such an oxygen are distorted to lower values.

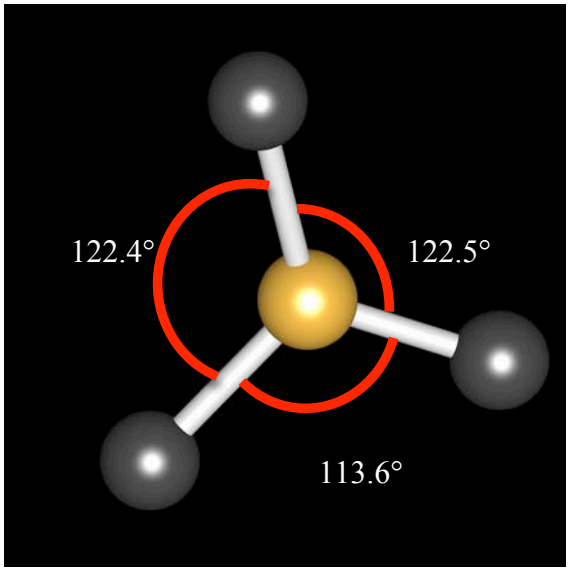

Figure 4-5. An illustration of the Si-O-Si bond-angles found associated with a triply-bridged oxygen is shown here.

Although the area of the fracture surface is small when compared with the external surface of the fiber, it contains many more small-membered rings and TBO than the fiber surface because the fracture occurred at room temperature, and the species on the fracture surface have less energy with which to reconnect back into the structure in favorable ways. These small, strained bond-angles in the two- and three-membered rings shift the average bond-angle of the system to lower values. As the fracture process proceeds, the population of these rings and TBO increases and the average bond-angle decreases, remaining lower than in the unstrained fiber.

7. Failure Process

In order to examine the process of failure in these fibers, each fiber has been deconstructed to show the surface areas separate from the core of material. The deconstruction of the periodic image of the square fiber is shown in Figure 4-6.

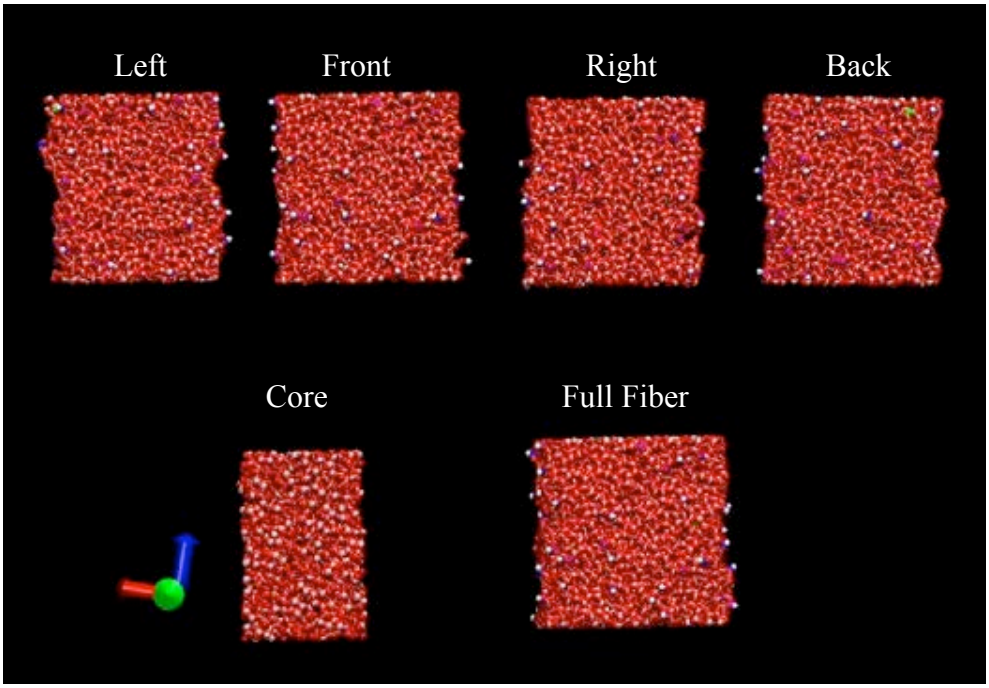

Figure 4-6. The square fiber, deconstructed into surface panels, core, and full fiber, as indicated, is shown here, without periodic images in the z direction.

In Figure 4-6, the surface panels are approximately 10 Å thick to include the full surface layer thickness indicated by both defect species and lower-density structure. Snapshots of the fracture process are shown in Figure 4-7. As the fiber is strained under tension, a void begins to open up in the right surface panel, illustrated in Figure 4-7A. Voids continue to open, propagating the crack on the surface of the fiber, in Figure 4-7B. This crack continues to progress along the surface, as it also moves through the bulk of the fiber. The center of the fiber is broken, in Figure 4-7C, while some of the surface remains intact, Figure 4-7D. Finally, the fiber is completely broken, shown in Figure 4-7E.

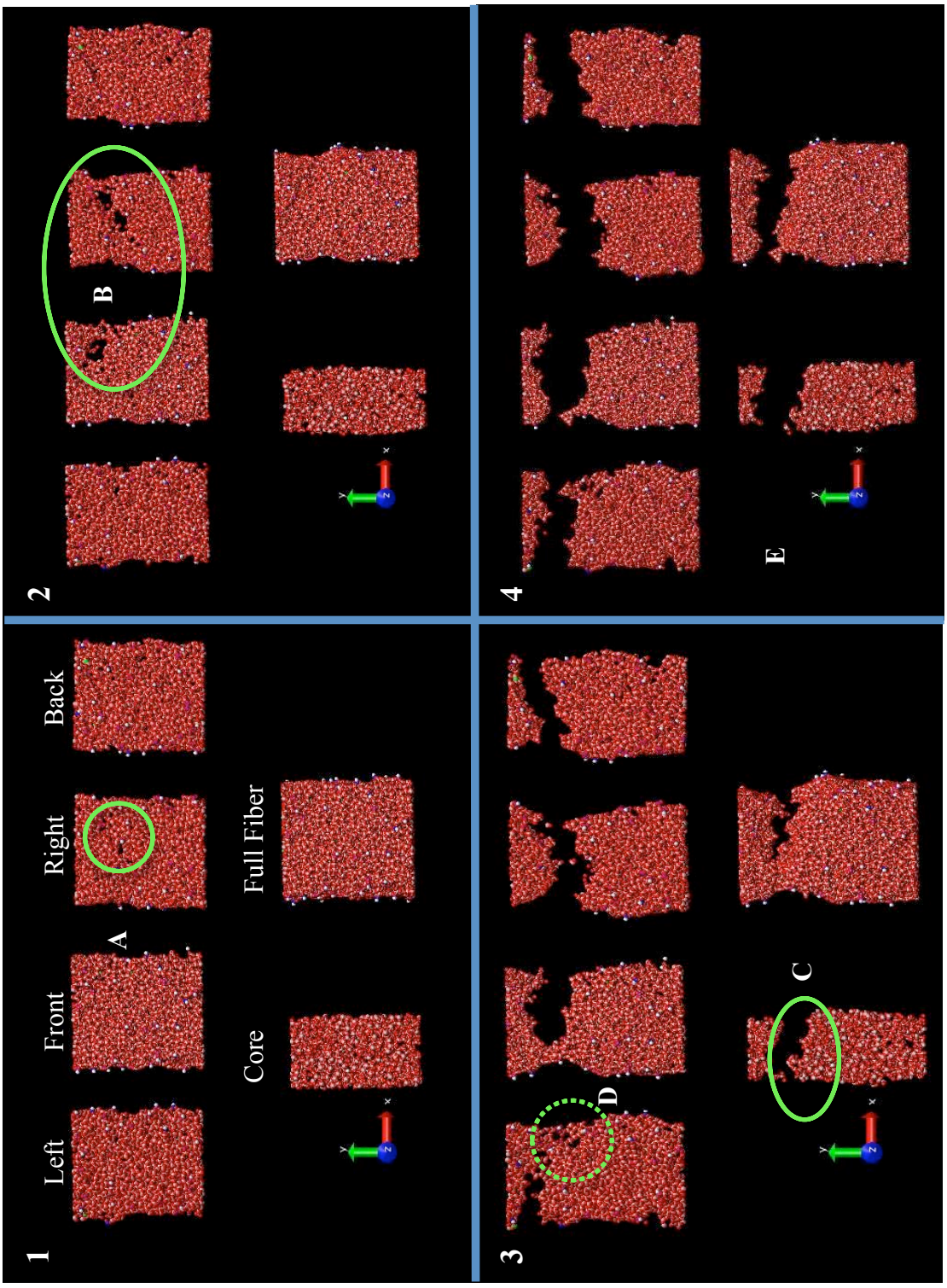

Figure 4-7. Failure of the square fiber is shown here, in stages. The panels are numbered in sequential order and show; A) Initial void formation, B) Cracks propagating in the surface of the fiber, C) Failure in the core of the fiber is completed, D) Part of the surface of the fiber is still intact, at the same time C is observed, E) Failure of the fiber is complete.

From this, it is clear that the fiber starts to break from a crack that forms on the surface. The crack runs completely through the bulk of the sample before it breaks through to the opposite side of the fiber.

A similar fracture process has been examined for the circular- and hexagonal-cross-section fibers, and is shown in Figure 4-8 and 4-9. Because of the rounded nature of both the circular and hexagonal fibers, they are displayed in thin sleeves, rather than being cut into panels as the square fiber was, for illustrative purposes. In each case, the interior material of the sleeve is colored grey so as to show only the sleeve surface facing out of the page, instead of looking through the whole fiber to the other side.

In each example, the fracture initiated at the surface. A crack was formed on the surface and that crack moved through the bulk of the material until the fracture process was completed at the surface. Although the sample geometries were different, the failure process was the same. This suggests that some structural feature of the surface, such as the unusually coordinated species, and/or the lower-density regions of the glass, is responsible for initiating the failure.

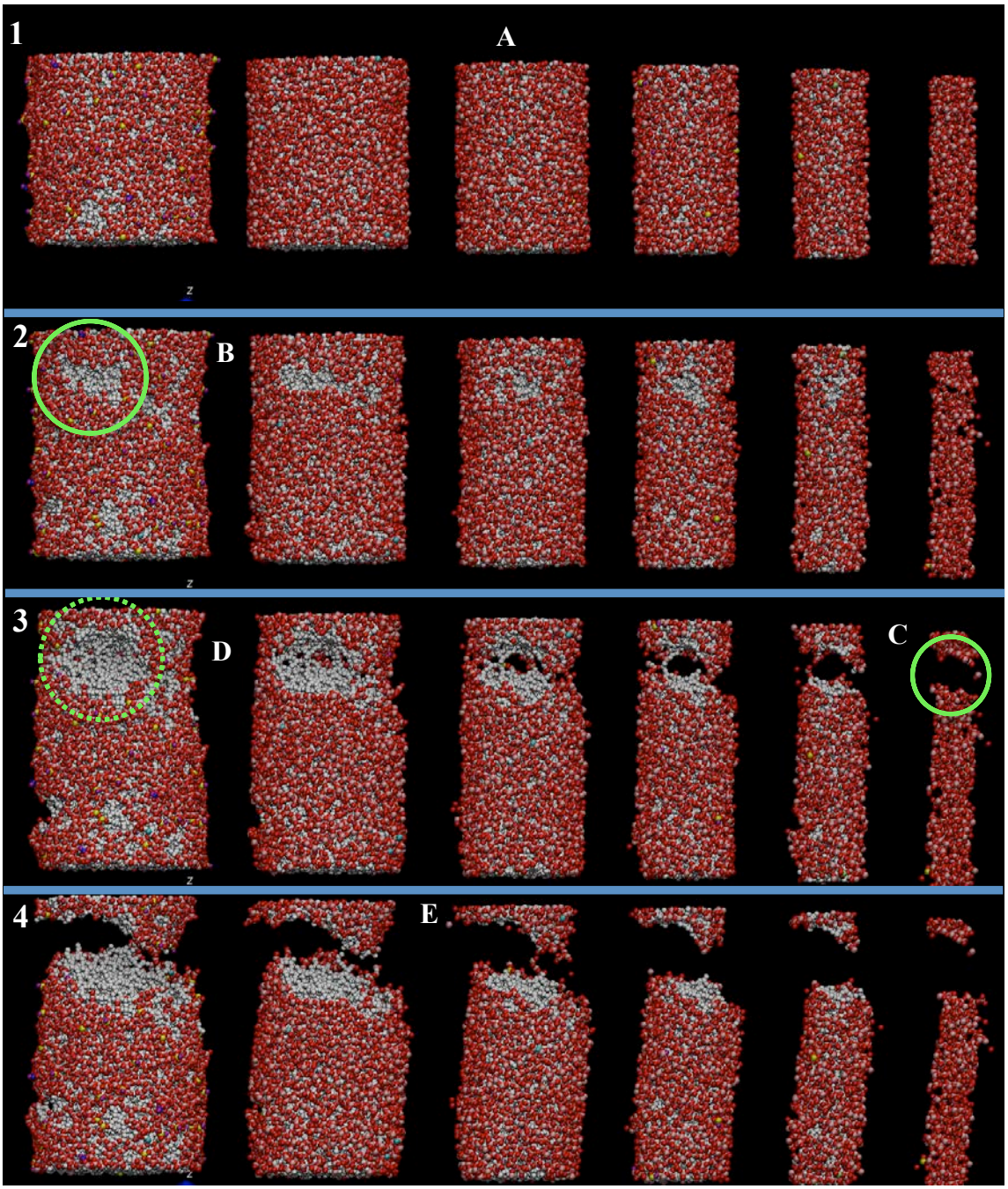

Figure 4-8. Failure of the circular-cross-section fiber is shown here. The panels are numbered in sequential order and show; A)Initial fiber sleeves, 5Å thick, B) Void formation on the fiber surface, C) Failure completely through the center of the fiber, D) Sections of the fiber surface are still intact as C is observed, E) Failure of the fiber is complete.

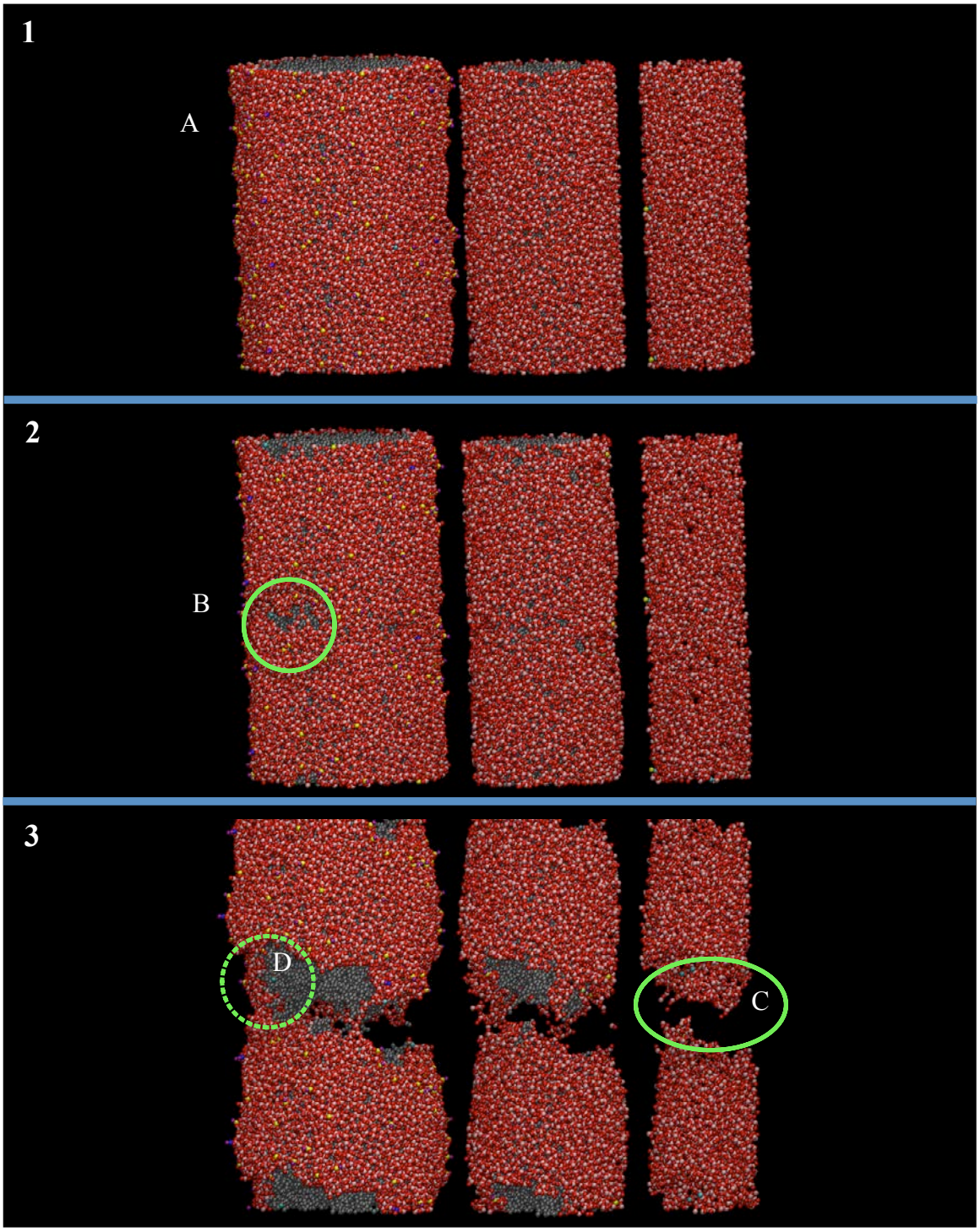

Figure 4-9. Failure of the hexagonal-cross-section fiber is shown here. The panels are numbered sequentially and show; A) Initial fiber sleeves, B) Void formation on the fiber surface, C) Failure completely through the center of the fiber, D) Sections of the fiber surface are still intact as B is observed.

8. Bond Breaking and Reforming

Table IV-VI. Species Coloration

Species	Color
NBO	Purple
TBO	Light Blue
Q1 Units or 1-coordinated Si	White
Q2 Units or 2-coordinated Si	Dark Blue
Q3 Units or 3-coordinated Si	Yellow
Q4	Pink
BO	Red

Bond breaking and reforming was observed within the fibers, and is discussed using examples from the square-cross-section fiber. In these snapshots of the structures, unusual species are re-colored after their recoordination as indicated in Table IV-VI to highlight the changes as they occur.

Before the failure strain was achieved, a significant amount of bond breaking and reforming was noted within the glass. An example of this is shown in Figure 4-10 for a tetrahedron found in the square fiber.

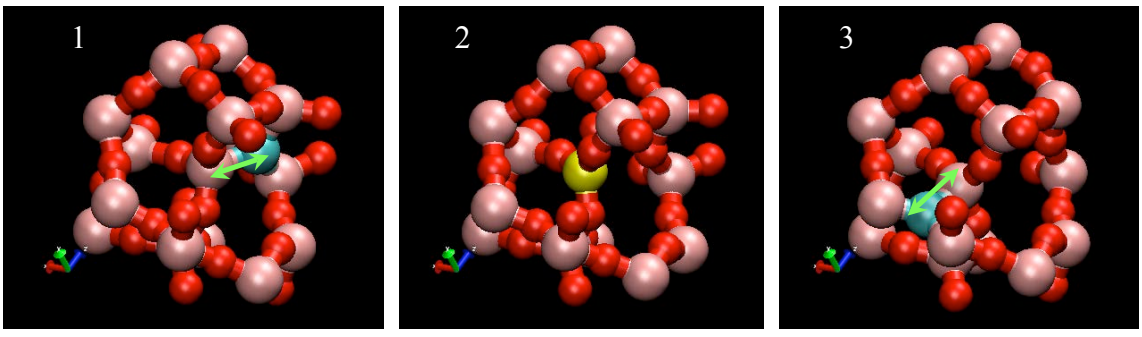

Figure 4-10. An example of the breaking and reforming of bonds within the square-cross-section fiber is shown here. 1) This arrow indicates a bond shared between a silicon and a triply-bonded oxygen. 2) Separation of the two atoms produces a three-coordinated silicon. 3) The three-coordinated silicon attaches to a bridging oxygen on the other side, indicated by the arrow, creating another TBO.

The bond breaking and reforming noted in Figure 4-10 occurred below a strain of 2%. This type of bond rearrangement within a local area was found to be somewhat repetitive. The movement of the three-coordinated silicon as it bonds with surrounding bridging oxygens is an attempt to achieve a fully coordinated tetrahedron. Since triply-bonded oxygens are also not energetically favorable, thermal vibrations and movement of the atoms under strain supply enough energy to repulse the silicon again, returning it to only three-coordination.

Although this localized action does not appear to lead directly to any immediate catastrophic failure, or even to the coalescence of voids within the structure when it occurs at such a low strain value, the phenomenon is significant. Bond breaking and reforming is a process typically associated with plastic deformation of materials, and any bond rearrangement during elastic deformation is expected to occur through the twisting and stretching of existing bonds. Figure 4-10 clearly illustrates bond breakage during the course of elastic deformation. This is not entirely unexpected, since the bonds that are changing are associated with defect species in the glass, but challenges our assumptions about atomistic motion during elastic deformation of a brittle solid. An atomistic computational study of the structural changes occurring in silica glass under an indenter[112] noted similar behavior in a region of elastic deformation.

Throughout the straining process, bond breaking without reforming was noted on the surface of the fiber in several places. Upon examination of the upper right face of the square fiber, where failure was noted to begin in Figure 4-7, bonds break without reforming, at a strain of approximate 6%. This is shown in Figure 4.11.

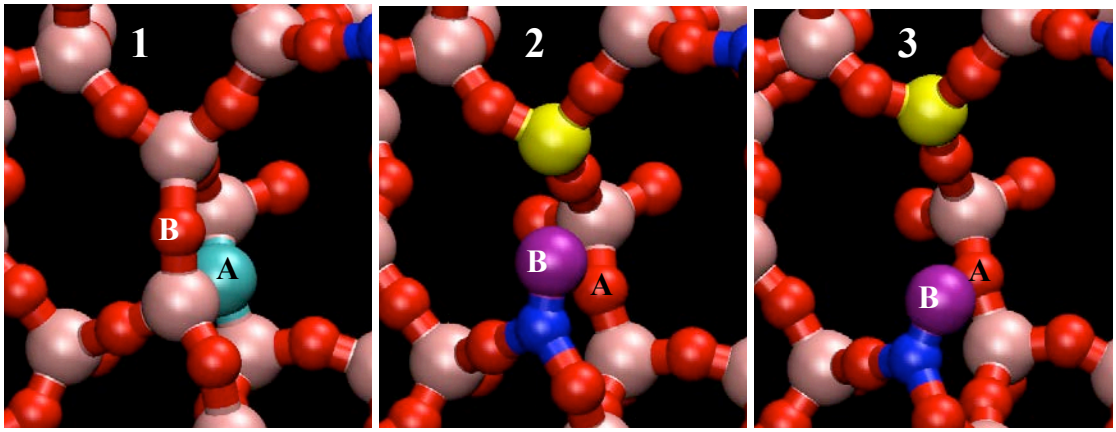

Figure 4-11. Bond breakage within the surface of the square fiber at 6% strain is shown here. 1) Oxygen A is a triply-bonded oxygen and oxygen B is a bridging oxygen. 2) Oxygen A becomes a bridging oxygen, and oxygen B becomes a non-bridging oxygen. This bond breaking produces two three-coordinated silicon species. 3) As the system is strained, oxygen B remains a non-bridging oxygen and moves further away from its position in frame 1. It is not reconnected back into the local structure.

The bond that breaks in Figure 4-11, transforming oxygen B into a non-bridging oxygen, does not re-form to connect B back into the structure where it was previously. Eventually, this non-bridging oxygen is recoordinated back into the structure as shown in Figure 4-12.

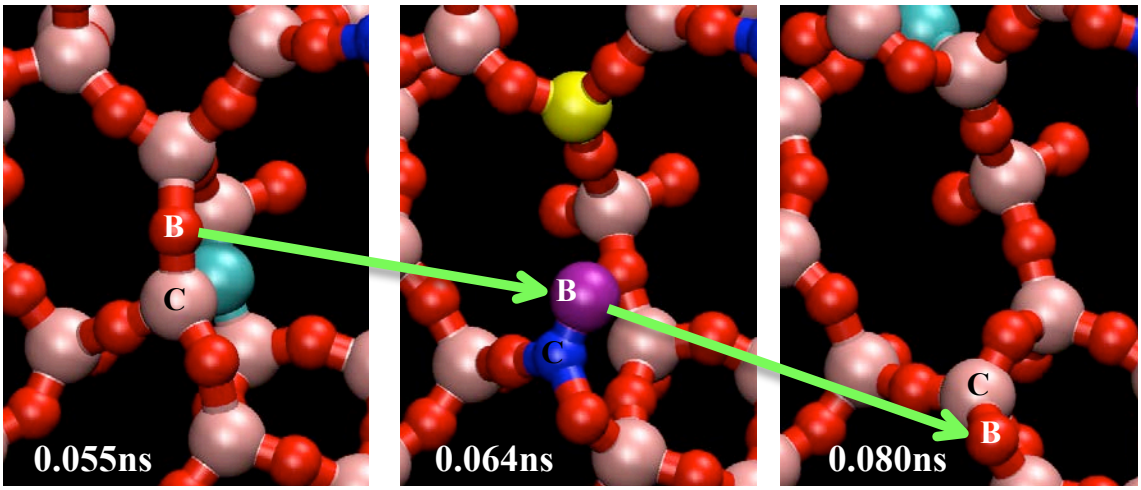

Figure 4-12. Movement of oxygen B to a new position in the structure, within the surface of the square fiber is shown here. Oxygen B moves a distance of 4.42Å to recoordinate back into the structure into a two-membered silicon ring. Silicon C moves away from its initial position as well.

As oxygen B moves away from its initial position, its associated three-coordinated silicon atom, C, also moves. In an intermediate step not shown in Figure 4-12, silicon C coordinates with a bridging oxygen, to create a triply-bridged oxygen. This action also creates a two-membered ring. The combination of a triply-bridged oxygen as a constituent of a two-membered ring, both energetically unfavorable structures, does not last. The TBO subsequently breaks away from one of its original silicon atoms, and is retained by silicon C when it becomes a bridging oxygen. Since silicon C has retained the oxygen, it is no longer three-coordinated, but has formed a tetrahedron. Oxygen B rotates out of the page and down, as it shifts away from the newly acquired oxygen that used to be the TBO. The tetrahedron rotates, and another two-membered ring is formed as the tetrahedron of silicon C shares two oxygen with a neighboring tetrahedron. This recoordinates oxygen B as a bridging oxygen again, 4.42Å from its original position in the structure.

9. Crack Formation in the Square Fiber

The square and hexagonal fibers both broke in the same manner. A single crack was formed on the fiber surface, which then propagated through the fiber to the other side. This process is illustrated in detail for the square fiber.

As Figure 4-10 shows, oxygen B is not recoordinated into the structure in a local position, so the local number of bonds over which stress is divided is decreased, creating a void that concentrates stress in the surrounding bonds. This stress concentration causes another bond to break involving an atom that was within the same ring, four tetrahedra away.

As the glass is further strained, more bonds begin to break, especially in areas of increased stress due to previously broken bonds, or areas containing three-coordinated silicon. Multiple bonds break at the same time, precluding any possibility of those atoms re-bonding back into their initial positions, opening up large gaps in the structure of the glass at the surface. The large gaps lead to further stress concentration at the edges, and the "crack front" moves from the glass surface into the bulk beneath. This process is shown in detail in the snapshots presented in Figures 4-13 through 4-22. In these figures, the timestep and box elongation are noted in each figure caption. Black markings are used to indicate action that is occurring in the timestep shown, and grey markings are

used to indicate locations in the figure where bonds have been broken in earlier figures. Figures 4-14 through 4-22 all show the same sample area as Figure 4-13.

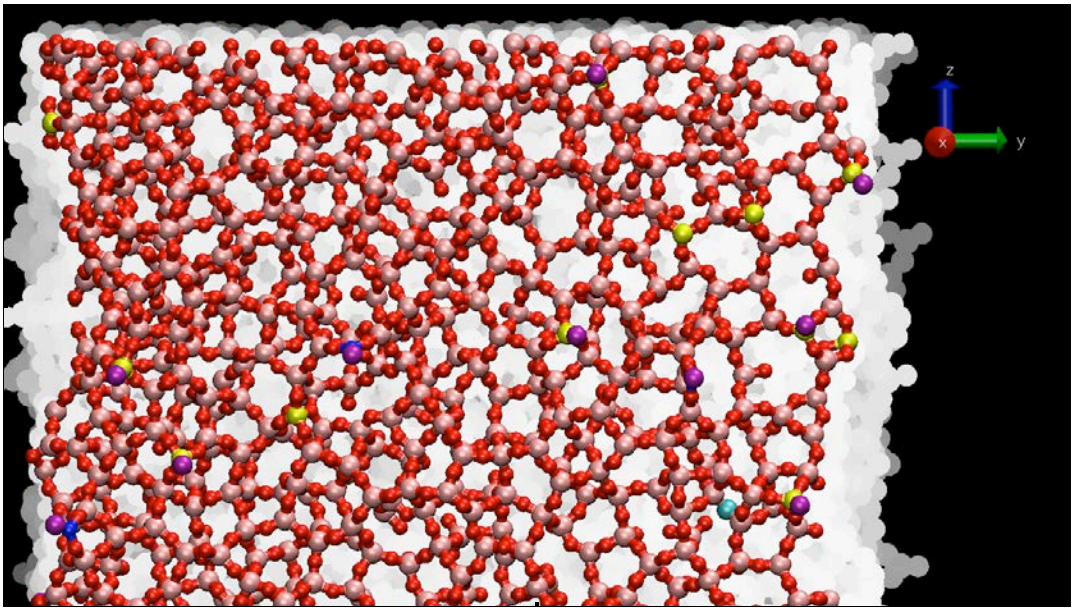

Figure 4-13. The top section of the right face of the square fiber is shown here. This area is where failure is shown to begin in Figure 4-7. Timestep 0, elongation 0%.

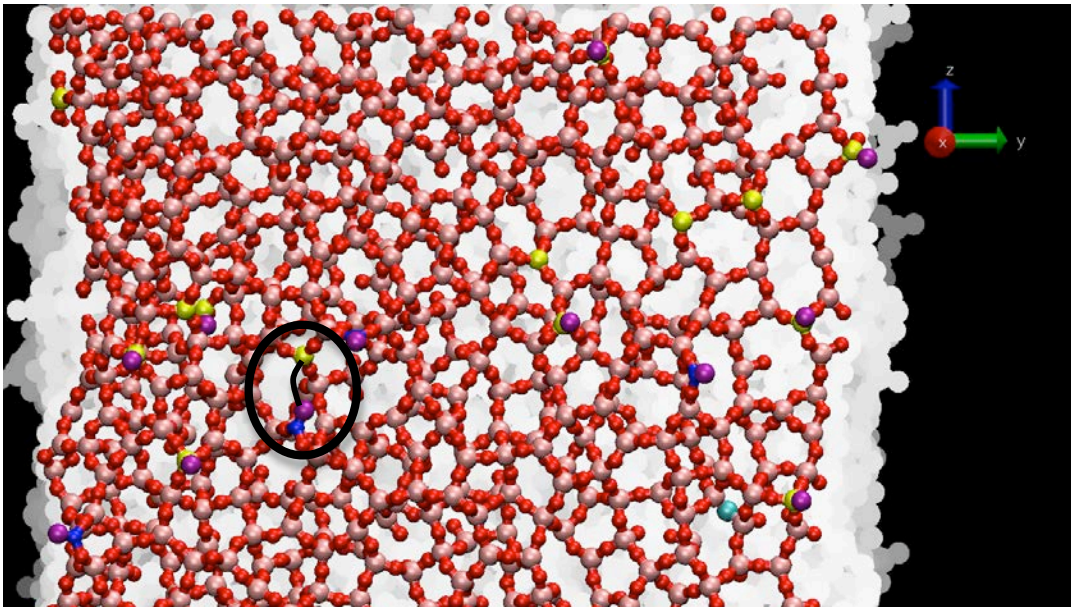

Figure 4-14. The black oval indicates the location of the failure of the bond shown in Figures 4-10 and 4-11. A black line bridges the open space between the two atoms that were previously bonded. Timestep 32,000, elongation 6.6%.

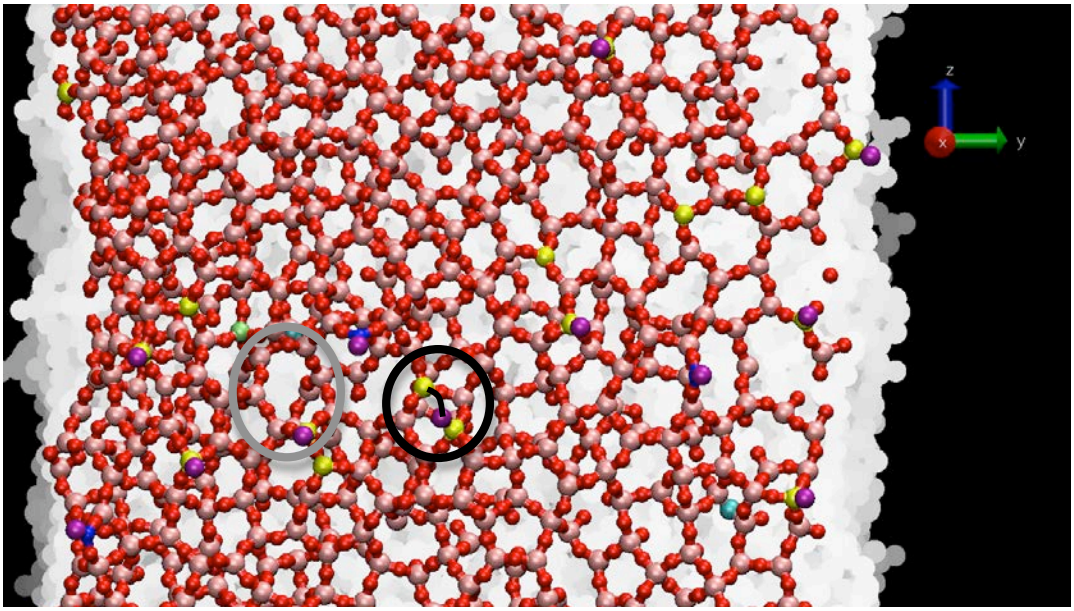

Figure 4-15. The black circle indicates the failure of a bond, and a black line is used to bridge the gap between the now separated atoms. The four-coordinated silicon is pulled away from one of the bridging oxygens to become a three-coordinated silicon, in yellow. Note that this silicon is a member of a ring that was enlarged by the bond breakage in Figure 4-14. Timestep 39,000, elongation 8.1%.

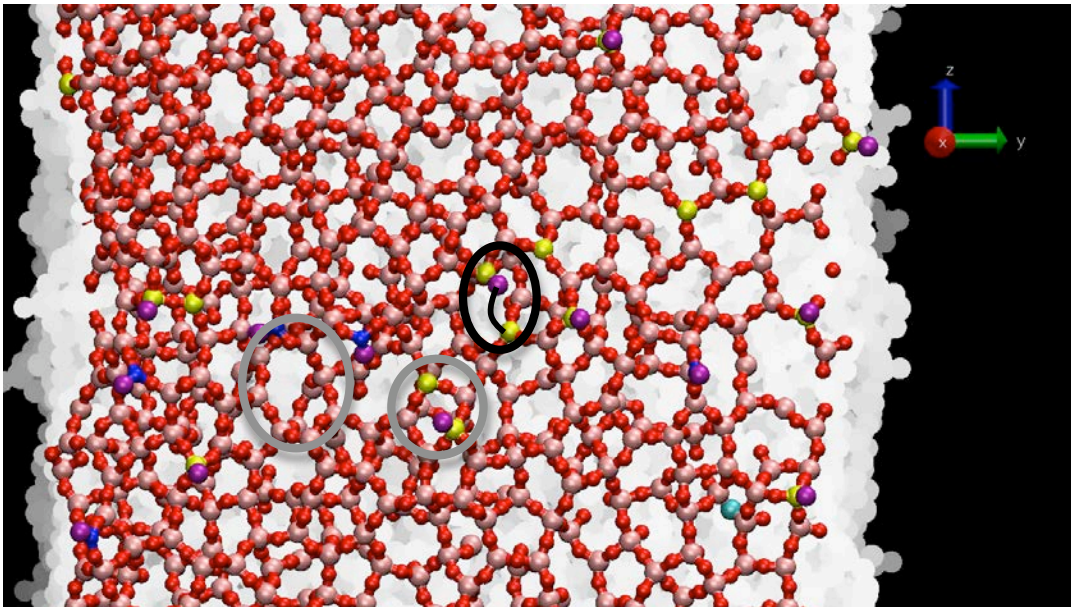

Figure 4-16. The black oval indicates the area where a bond has now been broken, and a black line bridges the separation between the atoms. What was a four-coordinated silicon is pulled away from one of the bridging oxygens to become a three-coordinated silicon, in yellow. Note that this silicon is a member of a ring that also contains the silicon transformed to three coordination in Figure 4-15. Timestep 48,500, elongation 10.2%.

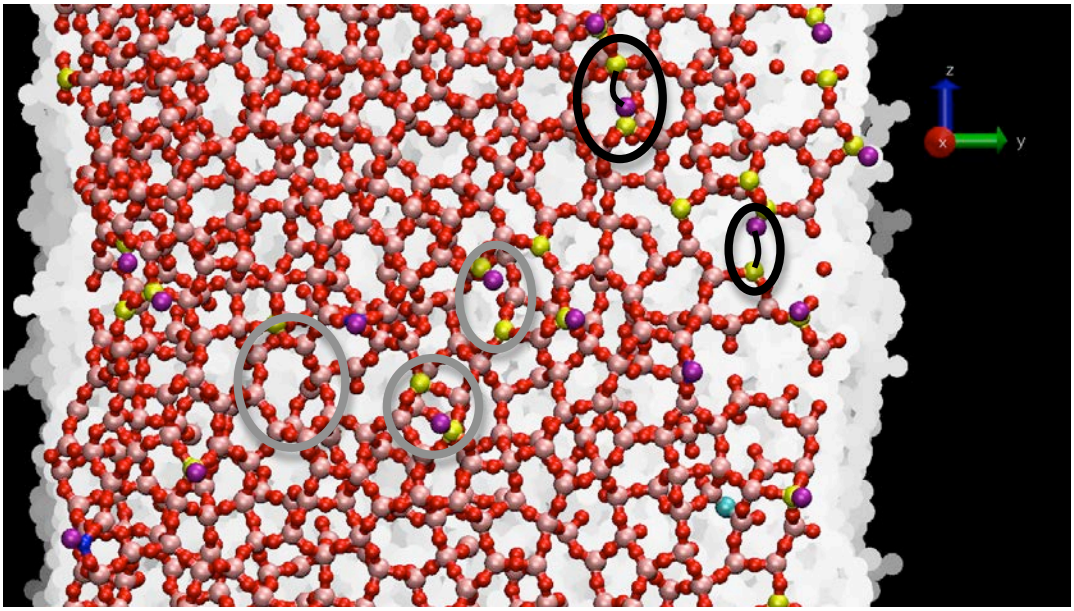

Figure 4-17. From right to left these two black ovals indicate where new bond breakages were noted at timesteps 53,000 and 53,500, and black lines bridge the gap between the newly separated atoms. Both bonds were closely associated with previously existing three-coordinated silicon atoms, shown in yellow in the previous figures. Timestep 54,000, elongation 11.4%.

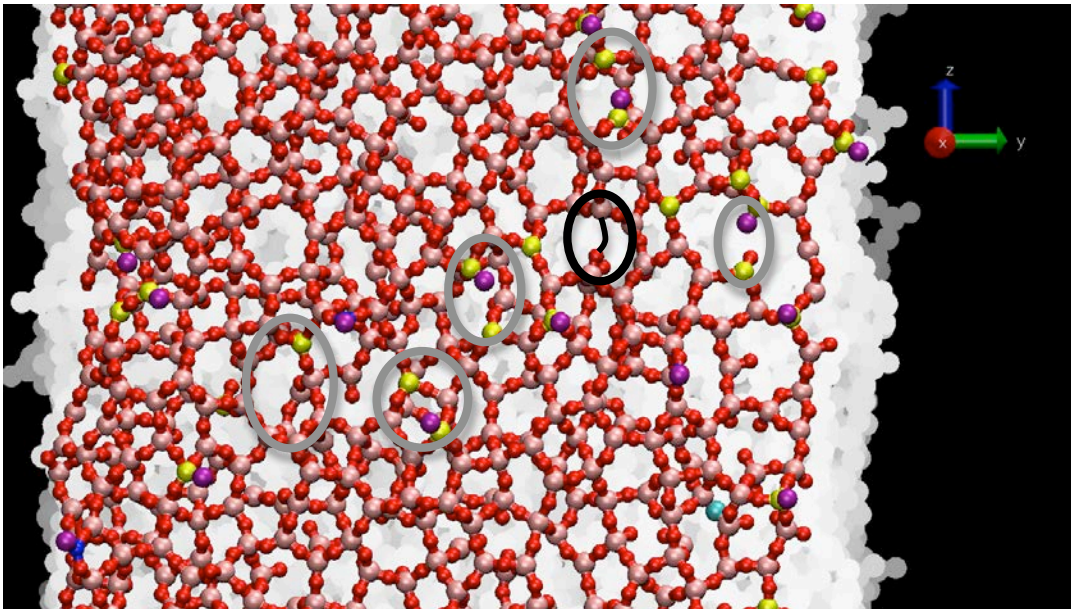

Figure 4-18. The black oval indicates the location of a newly broken bond, and a black line is used to bridge the space between the newly separated atoms. Timestep 60,500, elongation 12.8%.

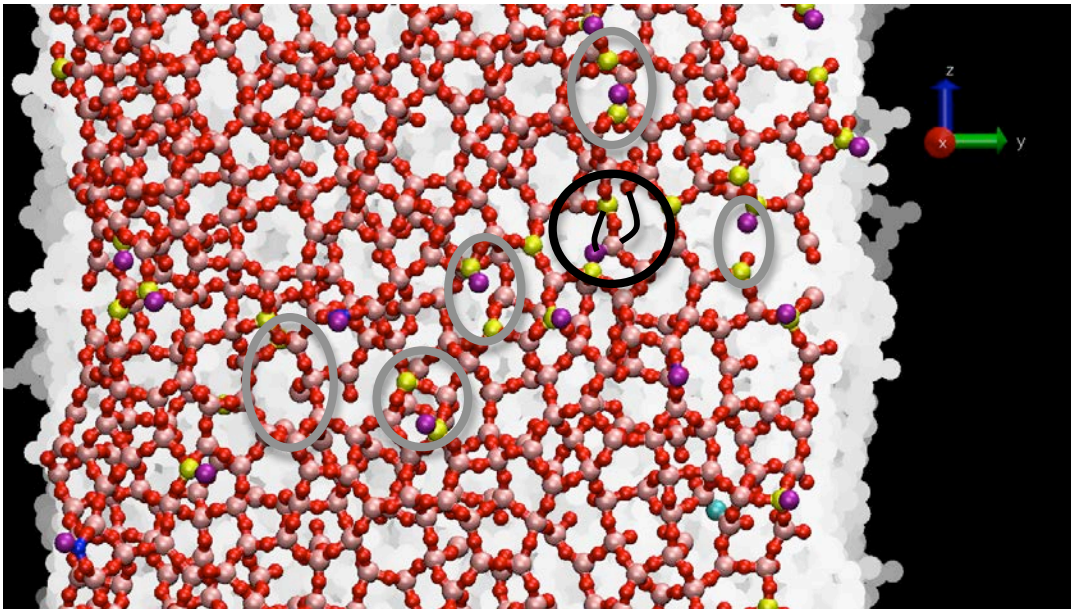

Figure 4-19. The black oval indicates a location with bond breaking and reforming. A silicon tetrahedron directly to the right of the three-coordinated silicon formed in Figure 4-18 loses a bridging oxygen and swings down to bridge the gap previously formed in Figure 4-17. Black lines are used to indicate the original atom pairs in both bond failures. Timestep 61,000, elongation 13.0%.

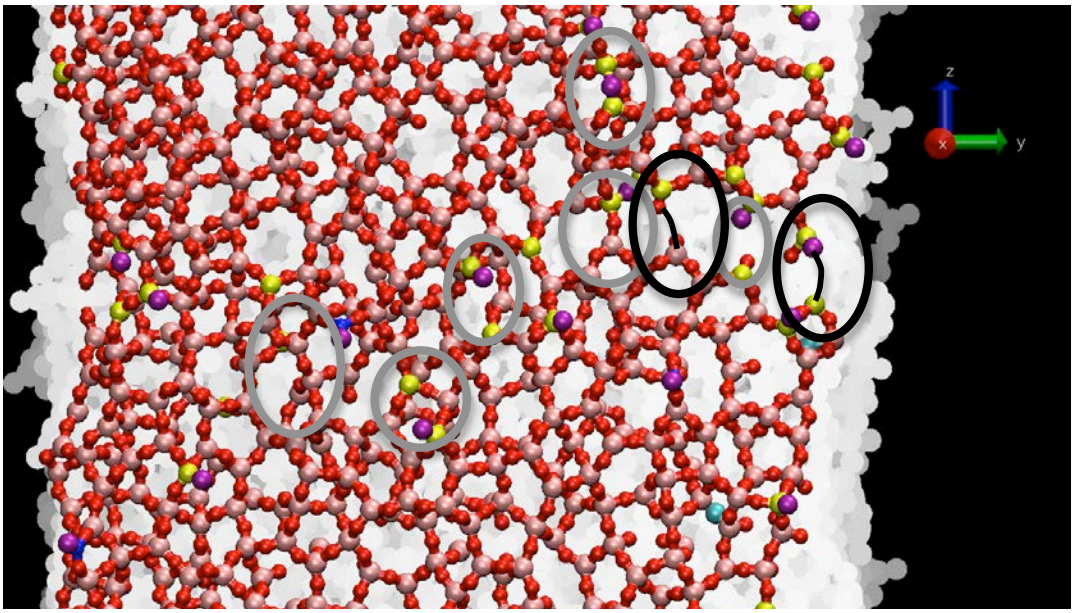

Figure 4-20. Black ovals are used here to show the location of two more bonds that have broken. Black lines connect the atoms that were bonded. Timestep 61,500, elongation 13.1%.

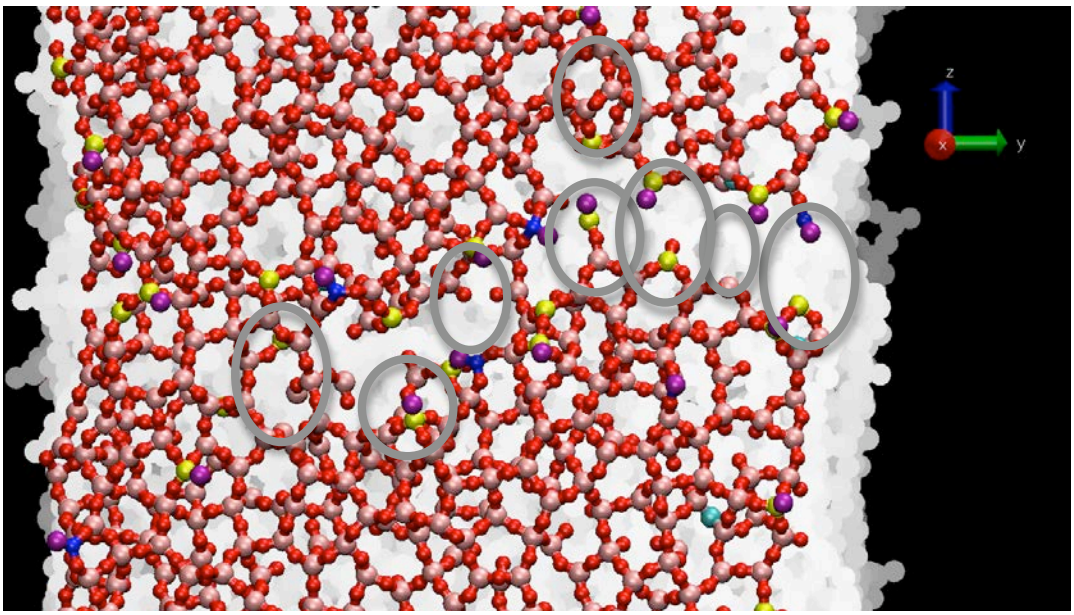

Figure 4-21. As the glass is strained, more bonds near the breakages highlighted in the grey circles ovals break, creating a crack along the surface of the face. Timestep 64,500, elongation 13.7%.

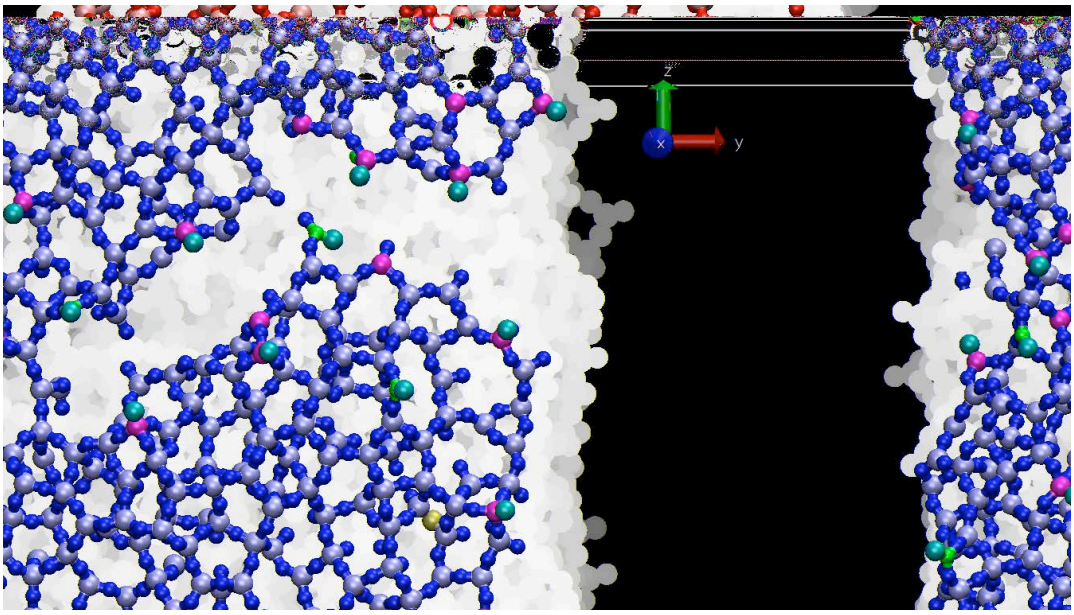

Figure 4-22. The crack moves into the bulk of the glass from the surface. Timestep 79,000, elongation 17.1%.

a. Summary of the Failure Process for the Square Fiber

In this sample, the crack was formed through a series of bond breakages, associated with undercoordinated silicon atoms and overcoordinated oxygen atoms. The initial bond failure occurred in a region that was missing an oxygen atom. As a three-coordinated silicon moved into tetrahedral coordination, a triply-bonded oxygen was formed, and as the triply-bonded oxygen broke away from a four-coordinated silicon, a three-coordinated silicon was formed. Subsequent bond failures occurred in regions where strain was increased due to this initial failure, and in other regions containing three-coordinated silicon and triply-bonded oxygen. These failures formed a fairly continuous line on the fiber surface, producing an region of concentrated stress. The remaining bonds within this line of broken bonds fractured from the high stress, and a crack was formed on the surface. This crack propagated through the bulk of the sample, and, breaking through to the other side of the sample, the sample was fractured.

10. Breaking the Cylindrical Fiber

Under stress, the cylindrical fiber also shows bonds breaking and reforming within the structure, as illustrated in Figures 4-10, 4-11, and 4-12. These processes are seen to occur in the presence of undercoordinated silicon and overcoordinated oxygen atoms, as they do in the square fiber. However, the square fiber breaks through the formation of a single large crack that moves through the structure, as previously shown. Bond breakages unrelated to the failure process were small and typically limited to a single bond. In the cylindrical fiber, the fracture process is not as simple.

As the cylindrical fiber is strained, three distinct and separate voids open up in the surface structure. This is illustrated in Figure 4-23.

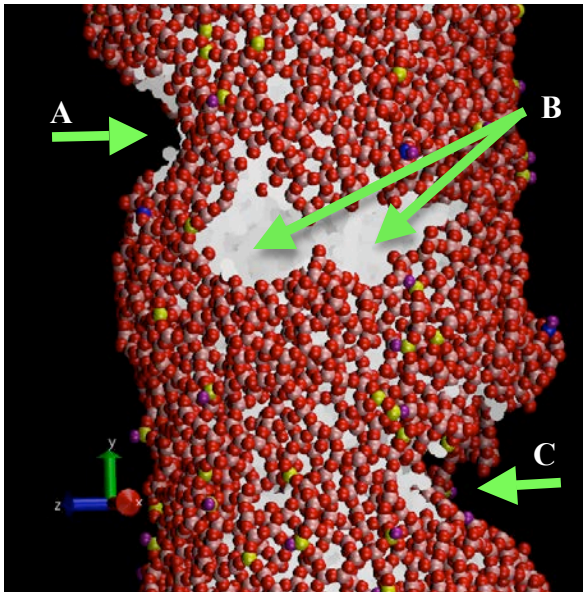

Figure 4-23. Three distinct voids, A, B, and C, have formed on the surface of the cylindrical fiber, indicated by the arrows. A single periodic image is shown in the z-direction.Timestep 159,500, elongation 37.5%.

These cracks do not coalesce into a single fracture plane. Instead, crack C alone runs through the width of the fiber to cause failure. After the fiber has broken, voids A and B are still visible in the fiber surface, as shown in Figure 4-24.

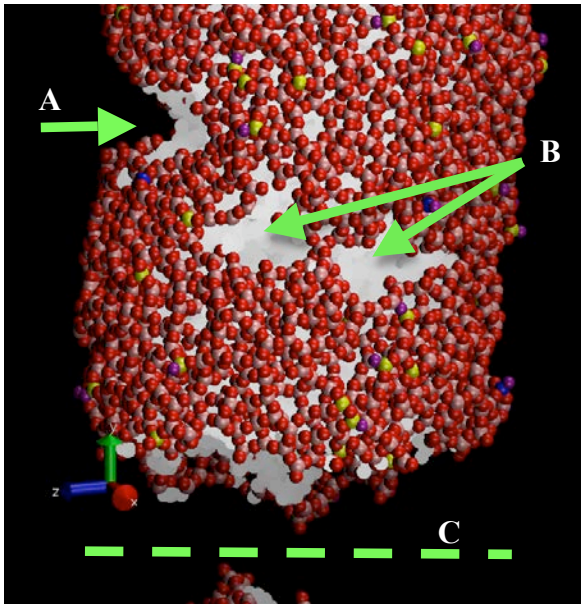

Figure 4-24. The fiber has broken, yet two distinct voids on the surface, marked as A and B, remain. Timestep 262,000, elongation 68.8%.

Since the fiber has broken by this timestep, the remaining structure is no longer under strain, and voids A and B have closed slightly. Through this process, void B has become separated into two regions.

a. Formation of Void A

Void A is formed in a similar manner to the crack in the square fiber. Bond breakages accumulate in a localized area over time until the stress concentration is great enough to cause multiple bond failure, opening the void. This process is detailed in Figures 4-25 through 4-35.

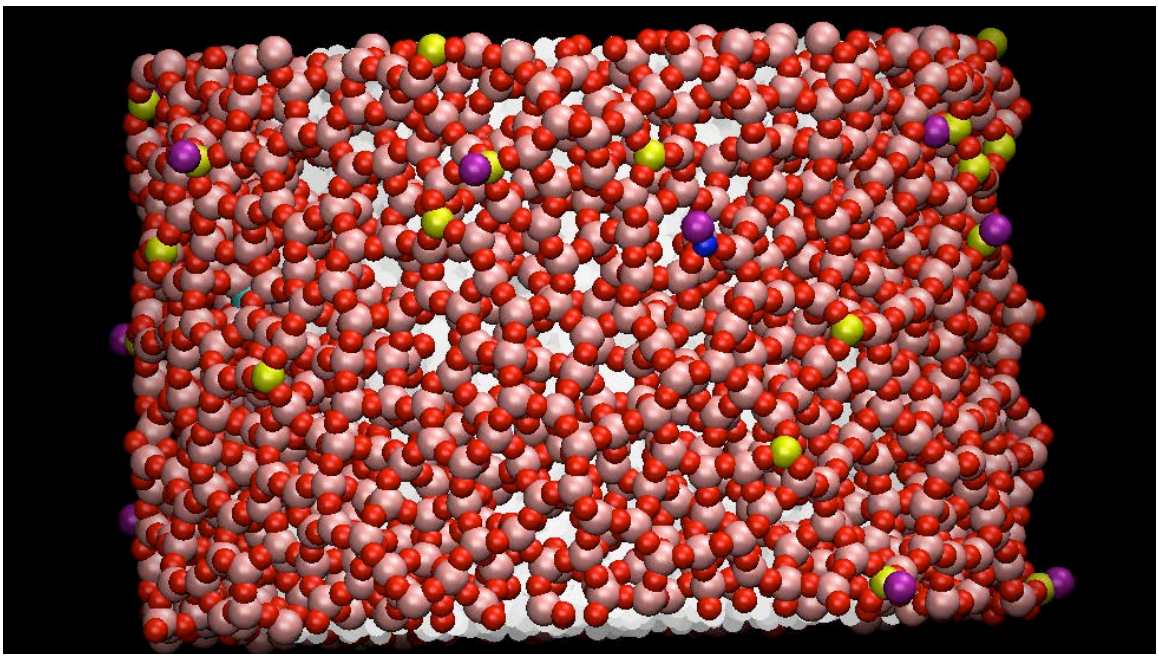

Figure 4-25. The fiber surface, for $z \leq 8$, is shown here, rotated to show the location of the formation of void A. Timestep 0, elongation 0%.

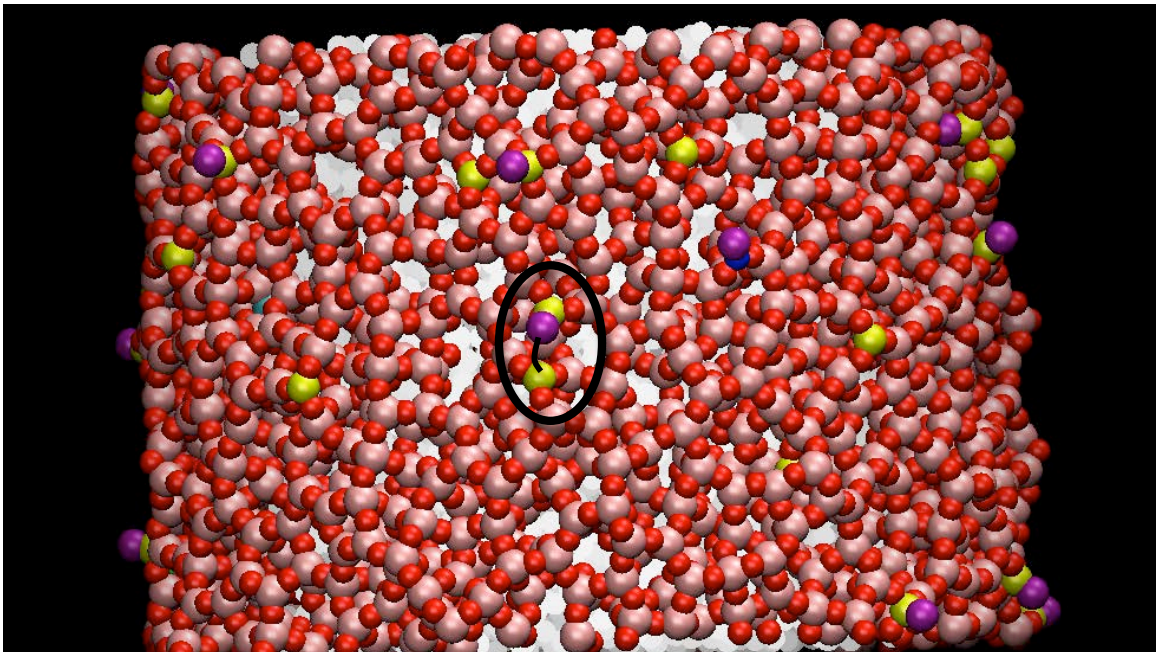

Figure 4-26. The first bond broken within the area of the formation of void A is shown here. This bond was not associated with either an overcoordinated oxygen or undercoordinated silicon, neither was it a part of any ring smaller than 4-membered. This bond was, however, aligned almost parallel to the z-axis. Timestep 30,000, elongation 6.2%.

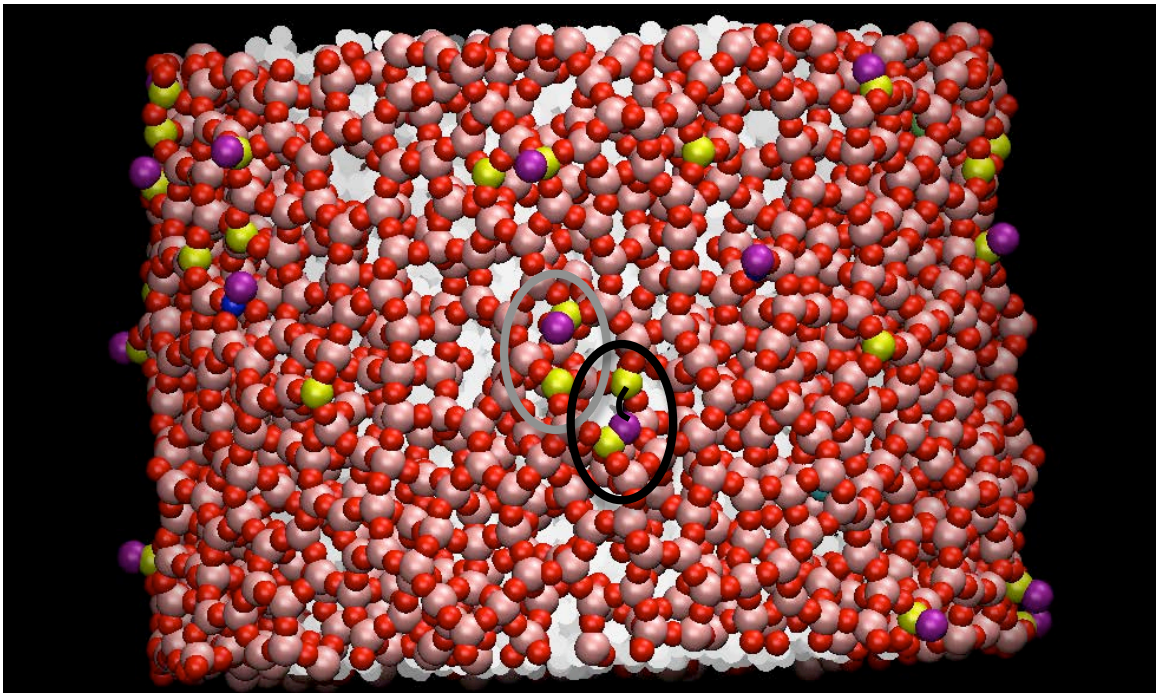

Figure 4-27. The second bond broken within the area of the formation of void A is shown here within the black oval. Timestep 43,500, elongation 9.1%.

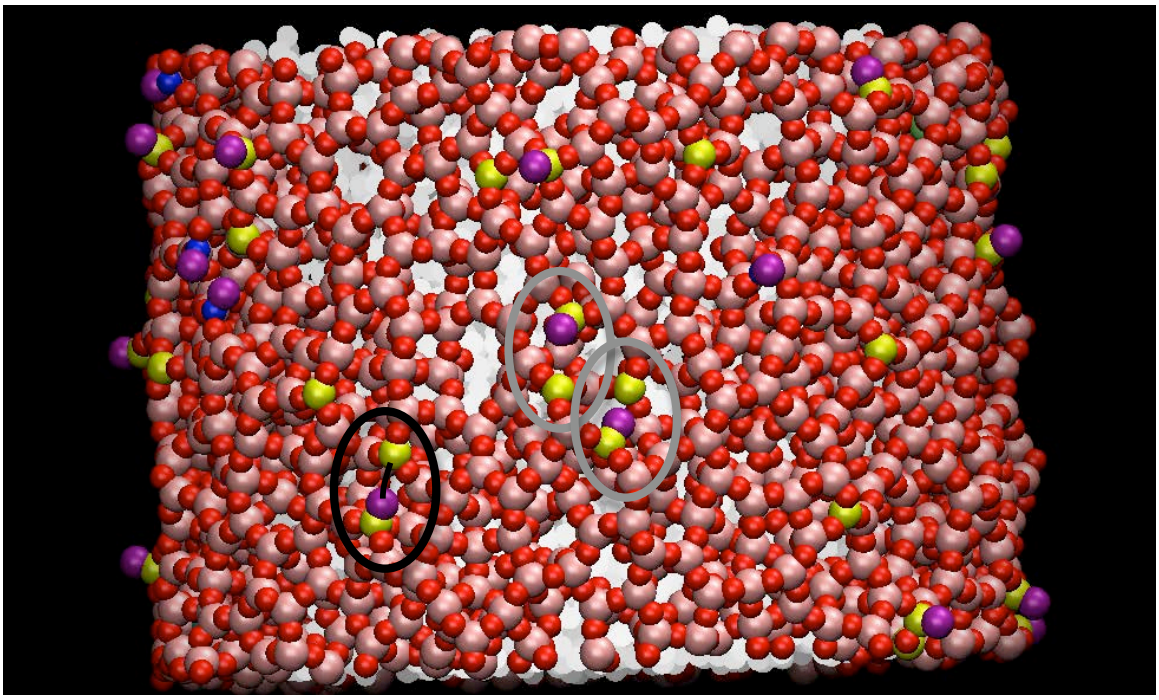

Figure 4-28. A broken bond is shown within the black oval. This bond was aligned with the stressed z-axis. Timestep 46,500, elongation 9.7%.

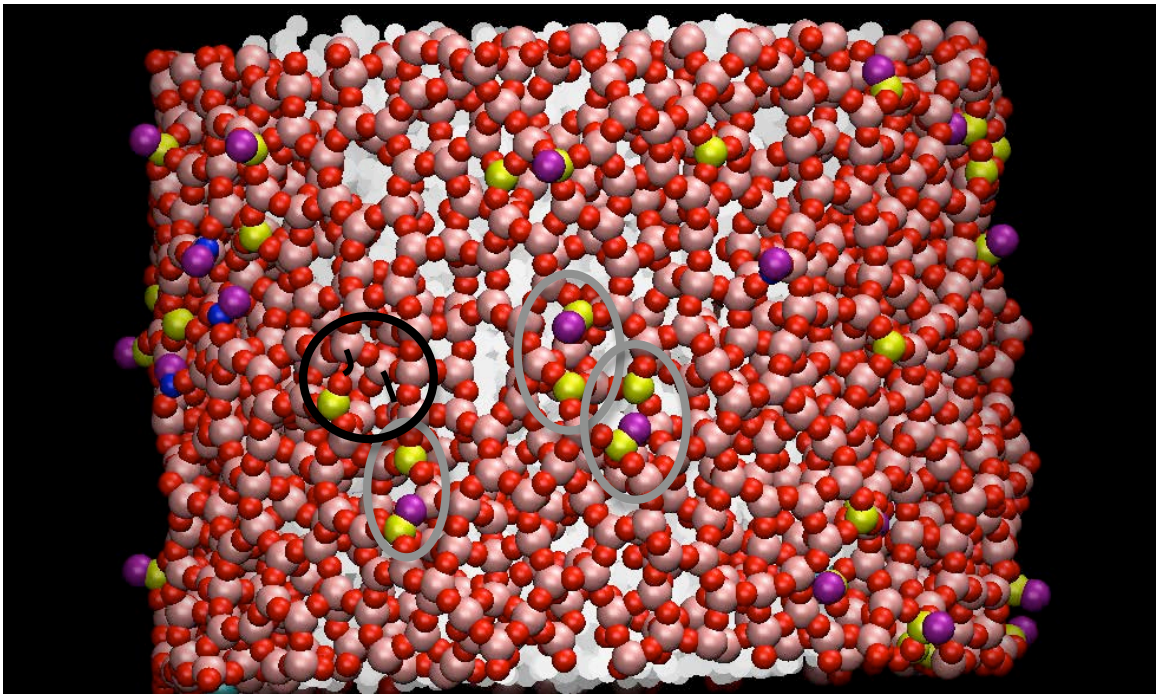

Figure 4-29. Two bond failures occur in this image, as indicated. Timestep 55,500, elongation 11.7%.

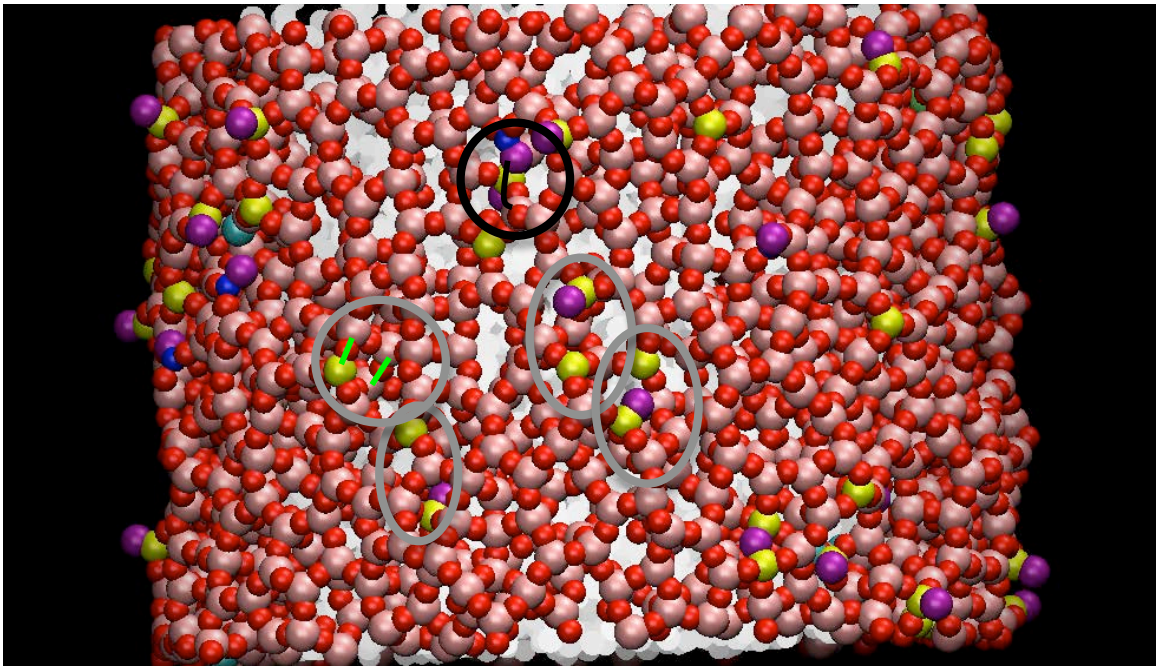

Figure 4-30. The two bond failures noted in Figure 4-29 have been recoordinated back into the structure, roughly in the same position as before the failure. Straight green lines are used to indicate these re-formed bonds within a grey oval. A bond associated with a three-coordinated silicon is broken in the black oval. Timestep 56,500, elongation 1.9%.

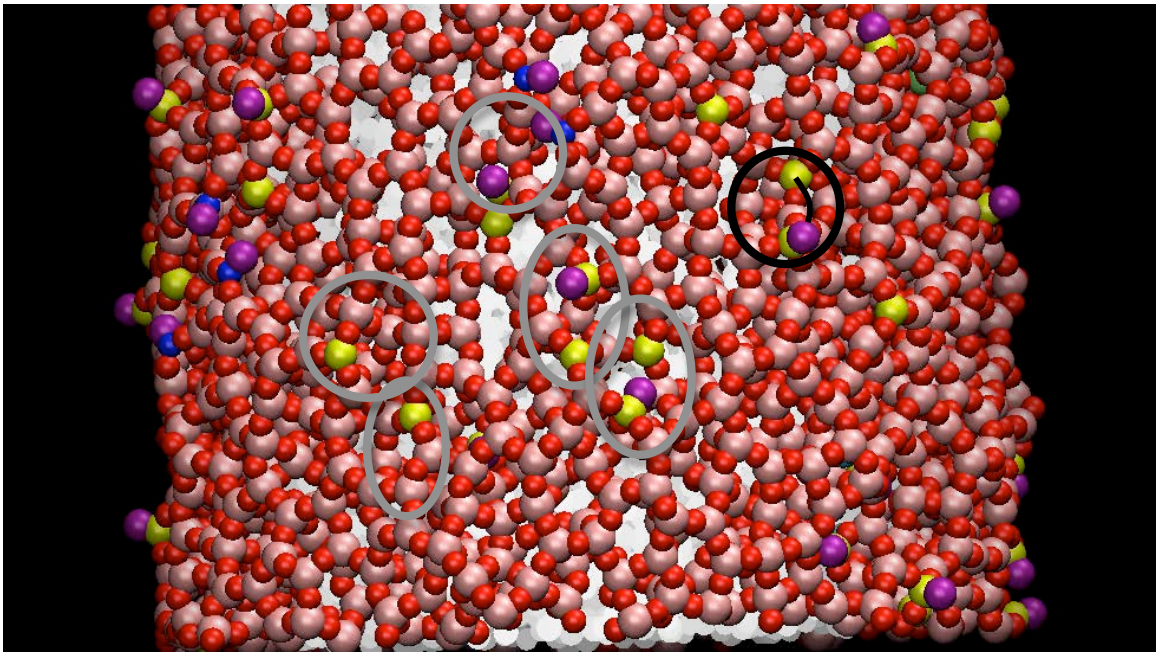

Figure 4-31. In this figure, bond failure associated with a three-coordinated silicon is noted. The maximum strain has already occurred at an elongation of 12.2%. Timestep 59,500, elongation 12.6%.

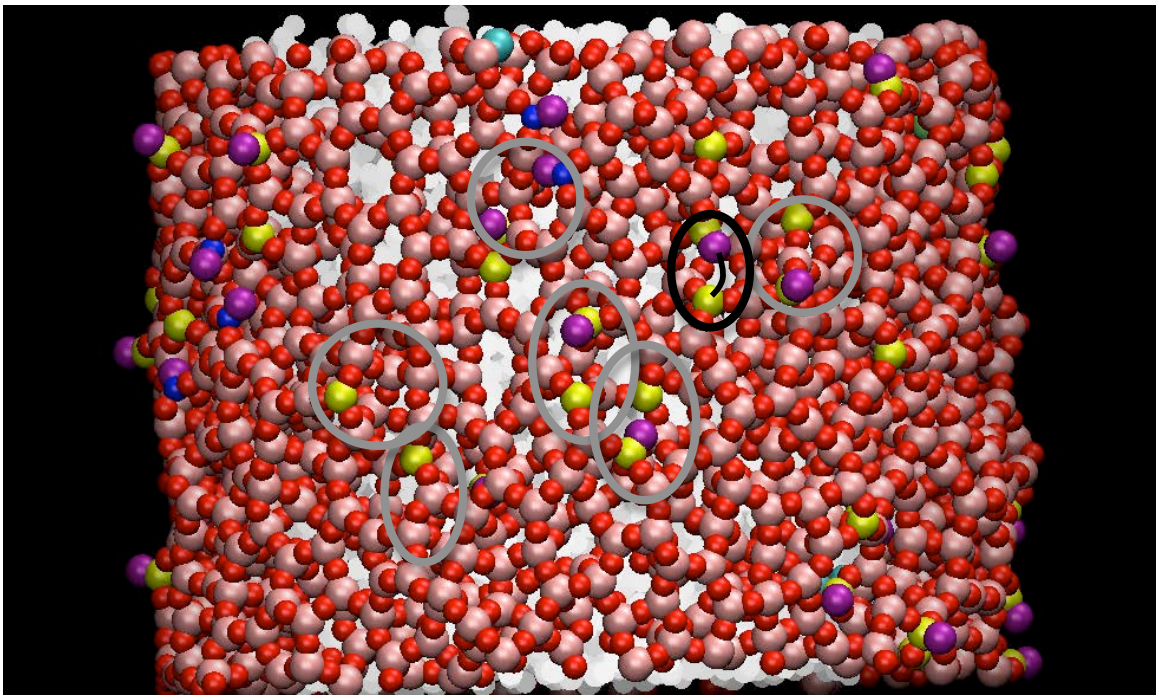

Figure 4-32. In this figure, another bond fails, close to the location of the bond failure in Figure 4-31. Timestep 60,500, elongation 12.8%.

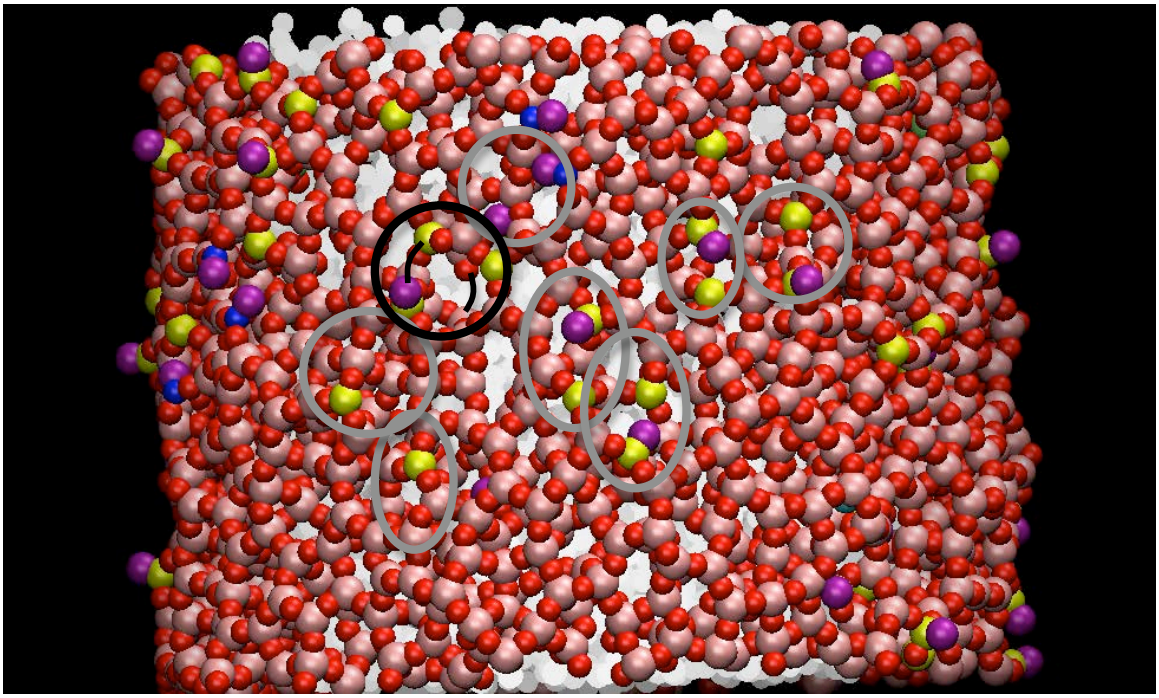

Figure 4-33. In this figure, two broken bonds are shown in the black oval. Bonds are now beginning to break more rapidly in the vicinity of the stress concentration due to previously broken bonds. Timestep 61,500, elongation 13.1%.

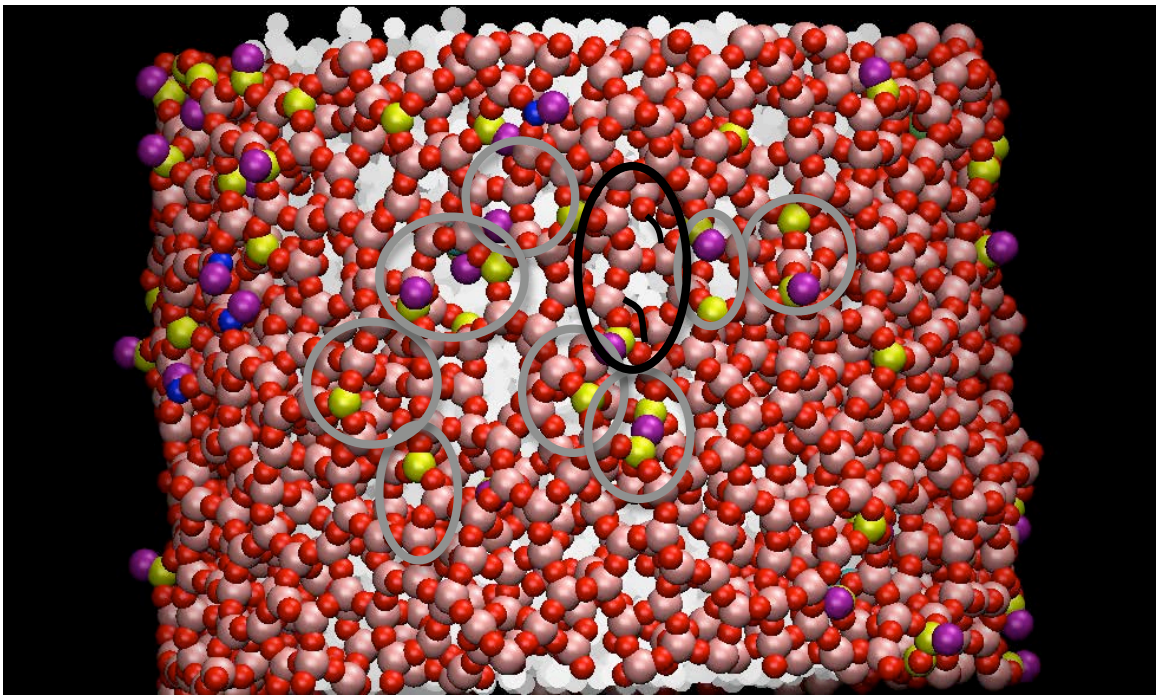

Figure 4-34. In this figure, two more bonds can be seen to have broken. Timestep 62,500, elongation 13.3%.

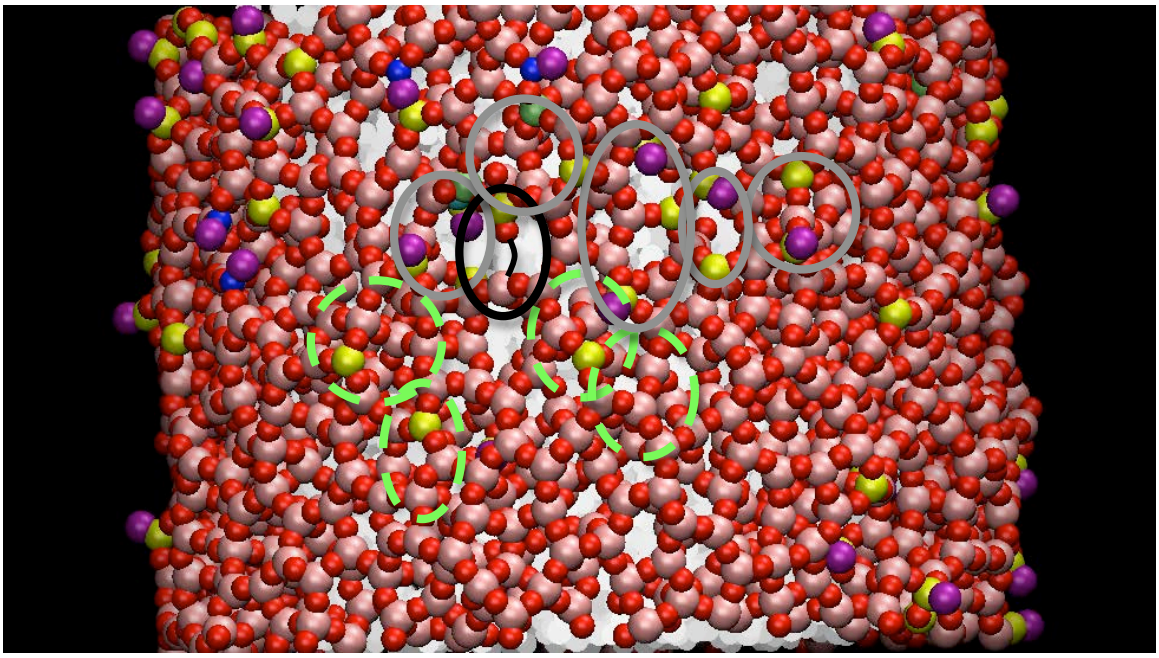

Figure 4-35. In this figure, another broken bond is shown, within the area of concentrated stress. Four of the grey ovals indicated in Figure 4-34 have been replaced with dashed green ovals to indicate the recoordination of the non-bridging oxygen atoms back into the structure. The bonds that broke in these locations reformed as other bonds broke. Timestep 64,500, elongation 13.7%.

In Figure 4-35, a clear area of concentrated stress has been formed, as indicated by the grey and black ovals. As bonds in this region continued to break, void A was formed, first as a small void, as shown in Figure 4-36. As the fiber was strained the void opened up into a larger area, as shown in Figure 4-37.

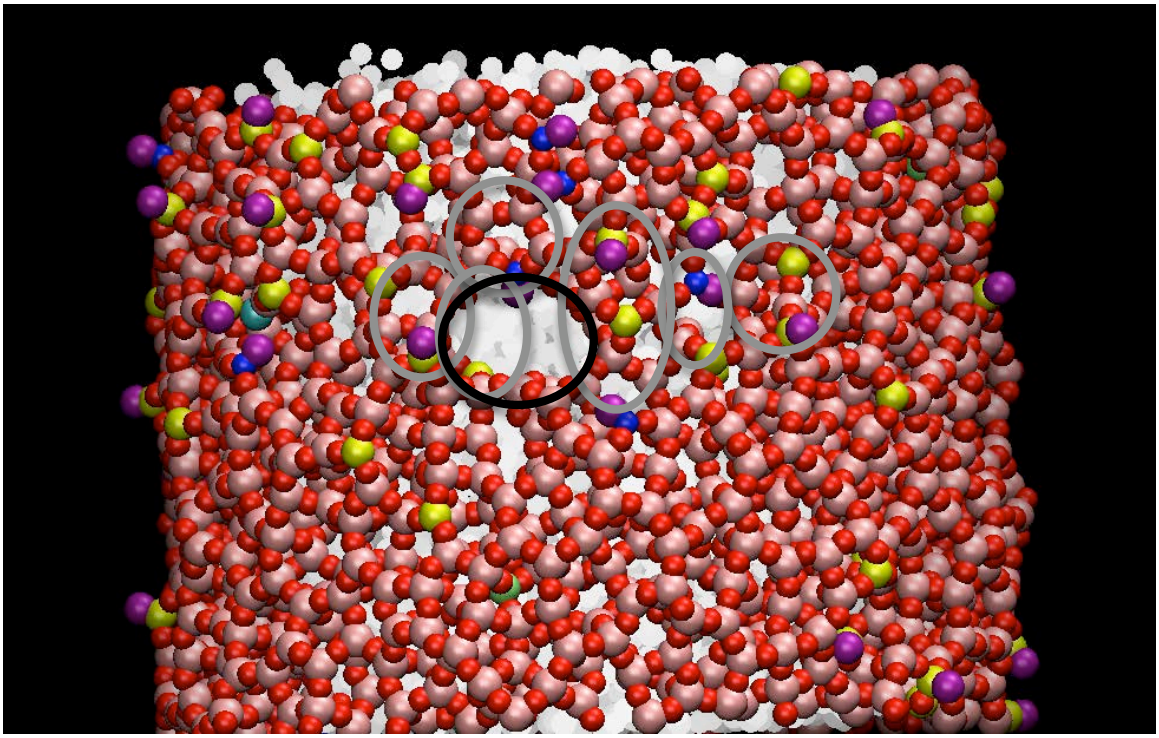

Figure 4-36. In this figure, the beginning of void A is shown. Grey ovals indicating areas of bond breakage have been superimposed over the void, from Figure 4-35 and the black oval indicates the void. Timestep 69,500, elongation 14.9%.

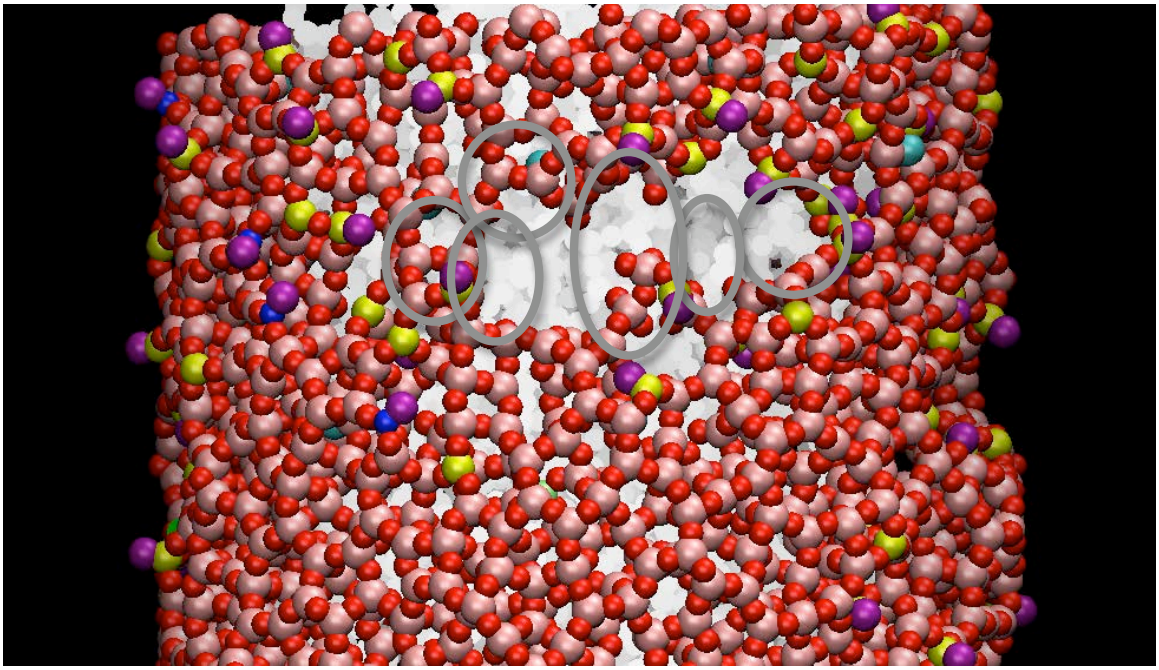

Figure 4-37. In this figure, a widened void A is shown. Timestep 92,000, elongation 20.0%.

Void A continues to increase in size as the sample is strained, becoming wider, taller and deeper into the bulk, until timestep 144,500, at which point the void maintains its size until the fiber is broken.

b. Formation of Void B

Void B is formed in a similar manner to void A through the formation of an area of concentrated stress from previously broken bonds. Individual bond breakages were noted at timesteps 25,500 and 59,000 before a noticeable void was formed. Void B is formed from the coalescence of two smaller voids, as suggested by its shape in Figures 4-25 and 4-24. The first of these is shown in Figure 4-38 at timestep 79,500.

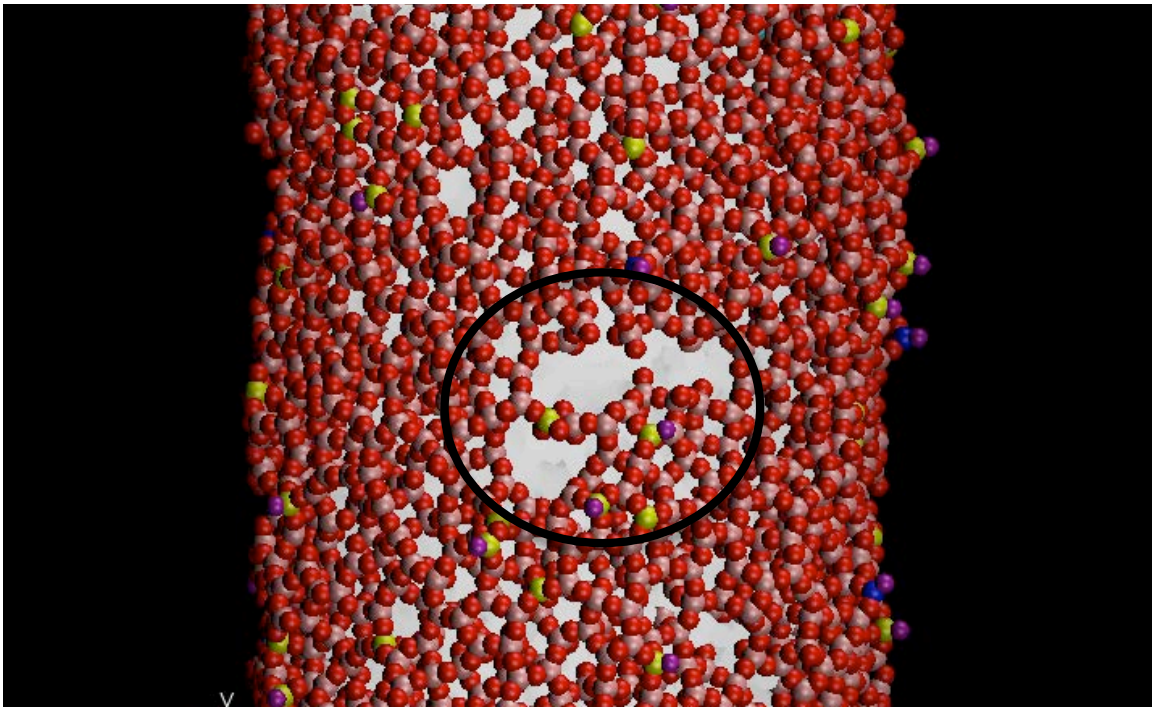

Figure 4-38. In this figure, the beginning of void B is shown. The void is shown in a black oval. Timestep 79,500, elongation 17.2%.

The lower left portion of the void shown in Figure 4-38 appeared first, around timestep 73,500, and the initial bonds that were broken were associated with three-coordinated silicon and triply-bonded oxygen.

Separately, a void opens to the upper left of the void shown in Figure 4-38, as shown in Figure 4-39, and the two coalesce into void B. The initial bonds that were broken to form this void were also associated with three-coordinated silicon.

When void B is fully formed, the lower portion of the void shown in Figure 4-39 has closed. As the bonds above this void broke to join the two sections of void B, the stress in the surface was released, allowing these atoms to relax back into the structure. The absence of this section of the void as void B is formed is illustrated in Figure 4-40.

Void B continues to grow in size until crack C runs the width of the fiber, fracturing it.

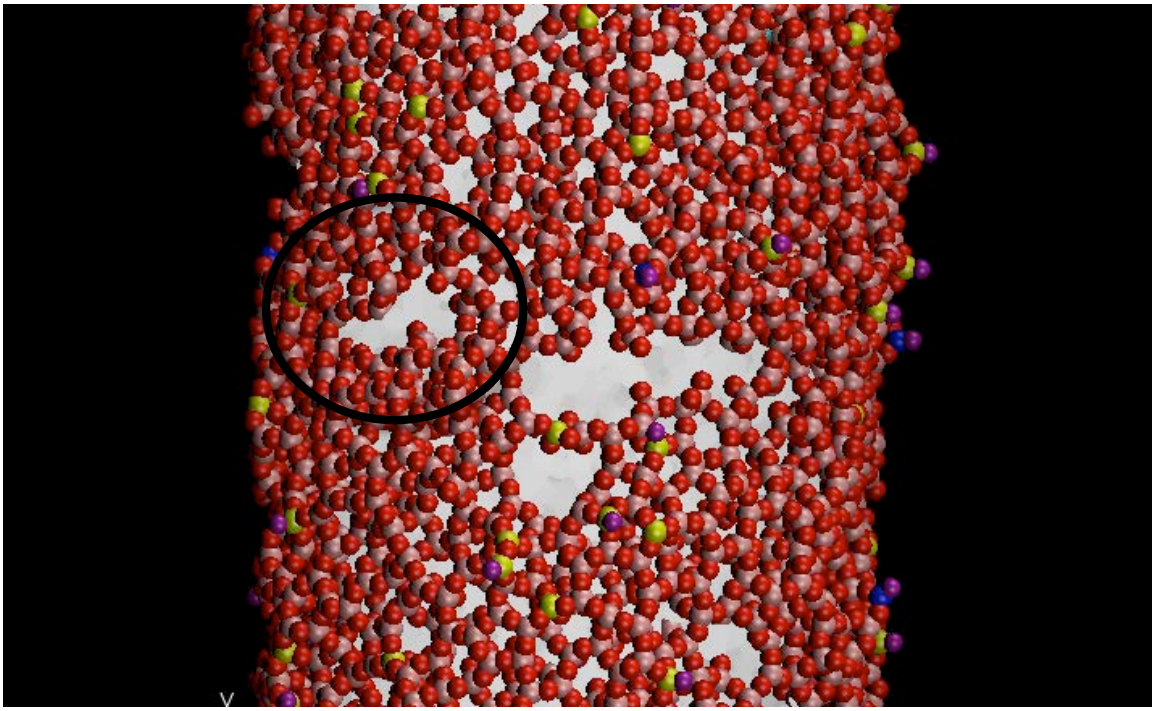

Figure 4-39. In this figure, the beginning of the second section of void B is shown, highlighted by a black oval. Timestep 94,500, elongation 20.8%.

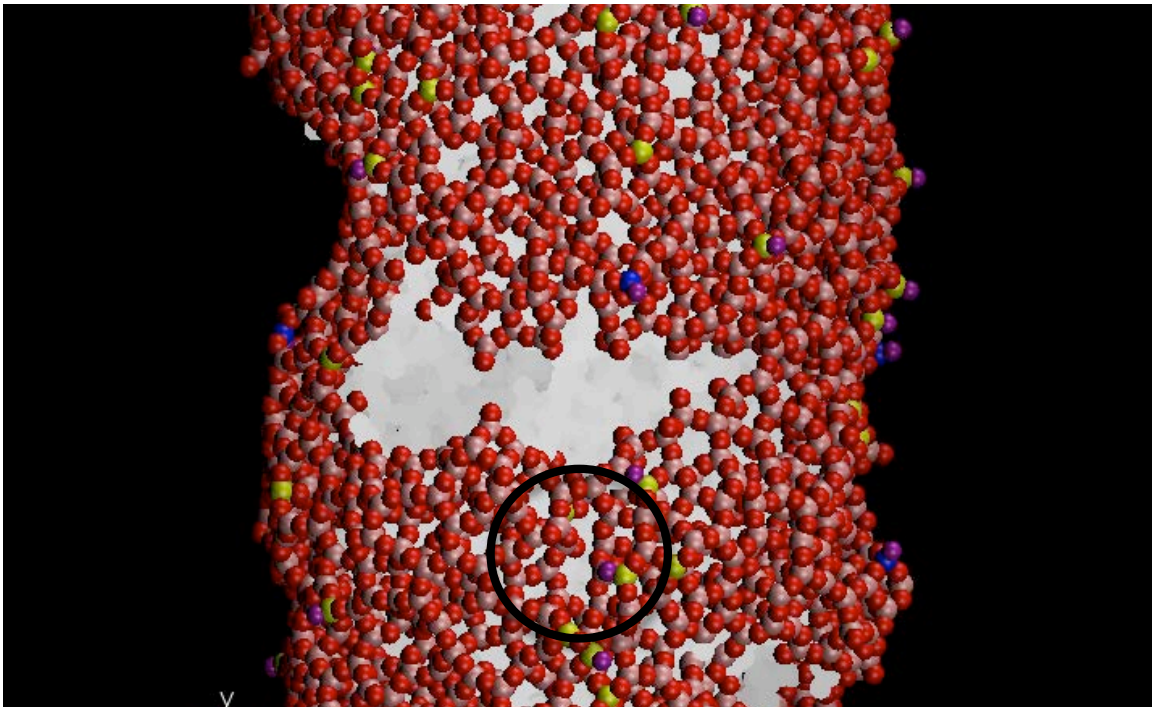

Figure 4-40. In this figure, void B has coalesced from the two voids shown in Figures 4-38 and 4-39. The bottom of the void shown in Figure 4-38 has closed, and the area it used to be in is shown in the black oval. Timestep 150,000, elongation 35.0%.

c. Formation of Crack C

Crack C is formed in a similar manner to the other voids in the fiber. However, bonds associated with crack C only begin breaking at timestep 40,000. This is later than the initial breaks for voids A and B at timesteps 30,000 and 25,500 respectively, and means that when the first bond broke in the area of crack C, local stresses were greater than in A or B. Overall stress on the fiber at step 30,000 is 7.6 GPa, but by timestep 40,000 has increased to 9.6GPa. Detailed analysis of the formation of crack C is shown in Figures 4-41 through 4-50.

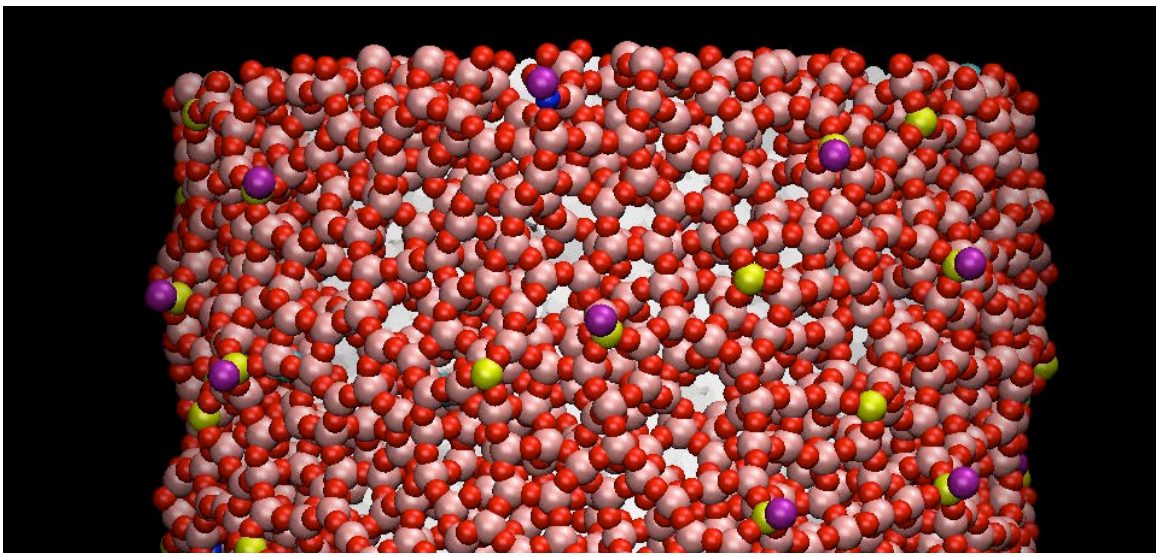

Figure 4-41. The cylindrical fiber is presented here, rotated to show the area in which crack C is formed. Timestep 0, elongation 0%.

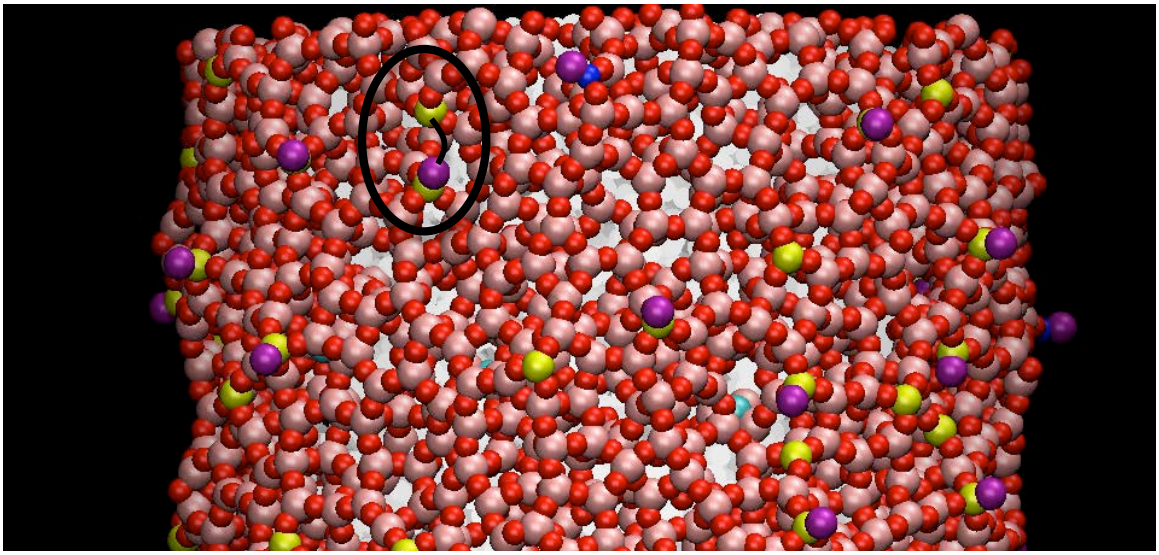

Figure 4-42. The first bond to break in the vicinity of crack C is shown here. Timestep 40,000, elongation 8.3%.

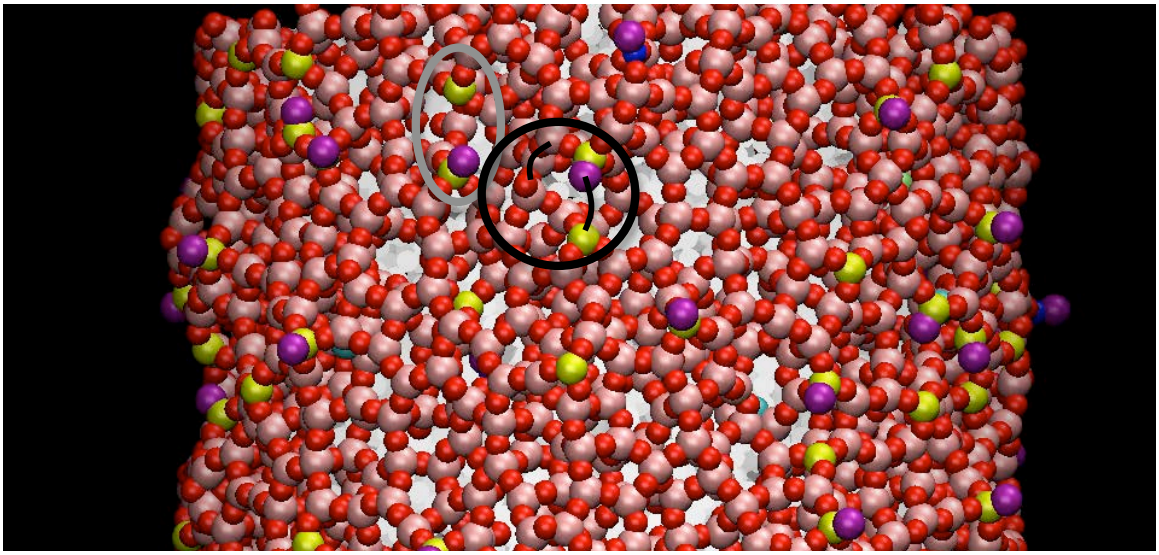

Figure 4-43. Two more bonds break, near the initial bond breakage shown in Figure 4-42. Timestep 62,000, elongation 13.2%.

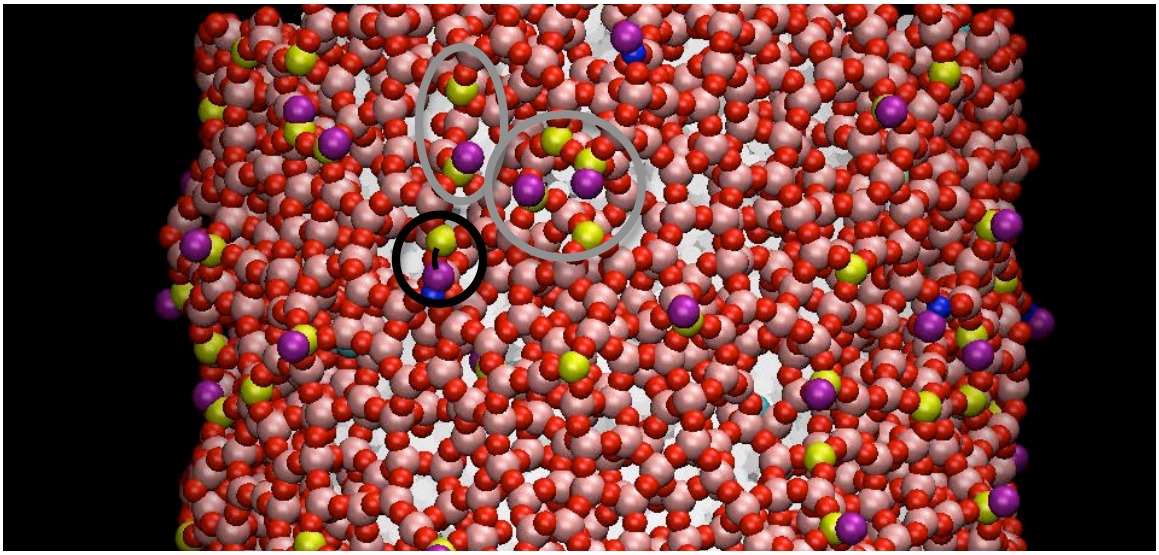

Figure 4-44. Another bond associated with a three-coordinated oxygen breaks on the surface. Timestep 64,000, elongation 13.6%.

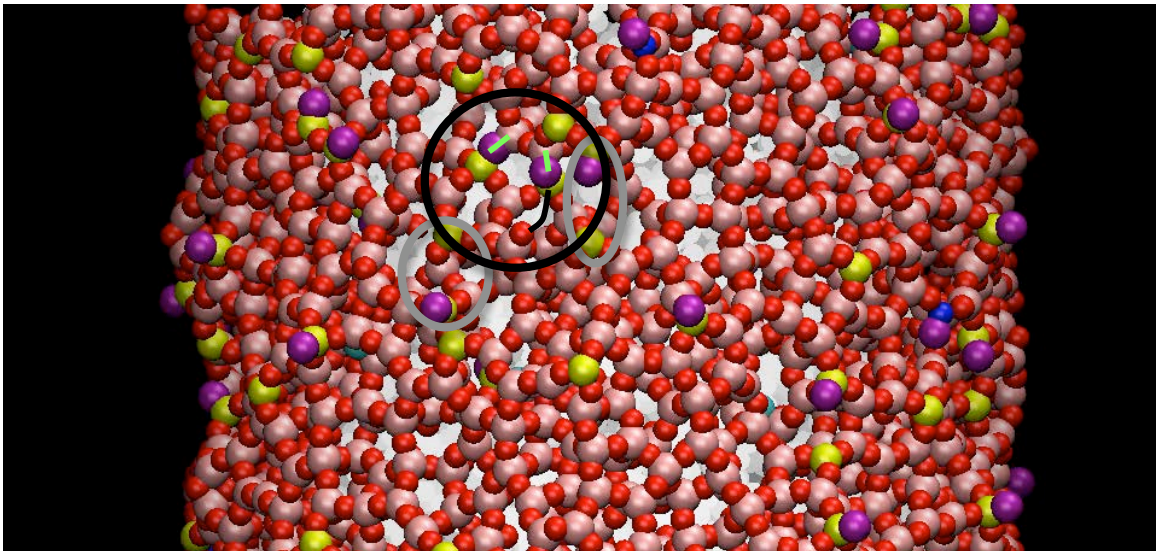

Figure 4-45. Two of the previously created non-bridging oxygens, from Figures 4-42 and 4-43 are reincorporated back into the structure, indicated by the two straight green lines in the black oval. The black curved line indicates a bond breakage that allows this reincorporation to occur. Timestep 69,500, elongation 14.9%

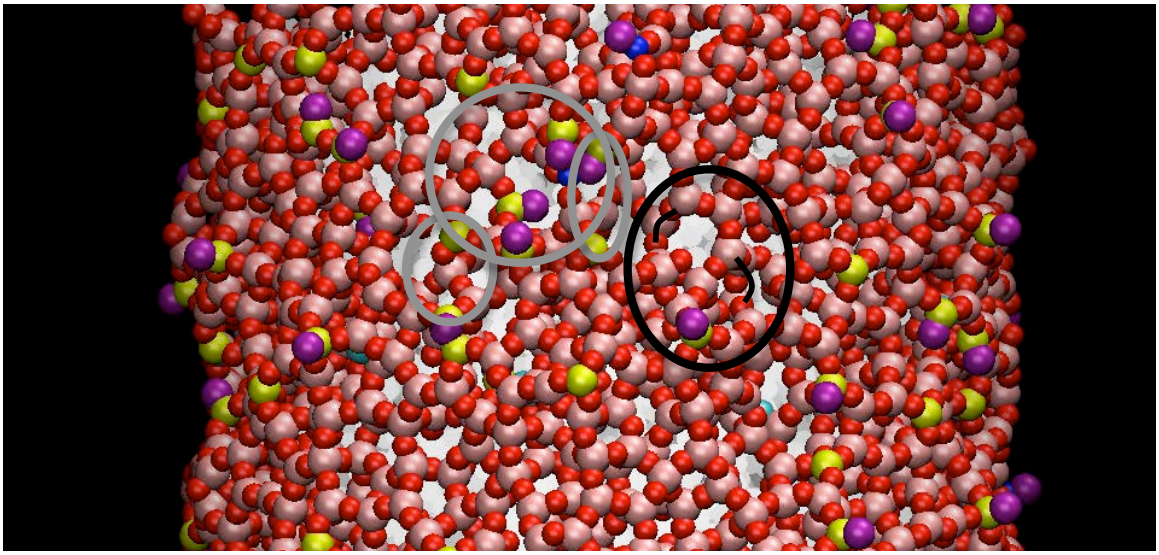

Figure 4-46. Two new bond are shown broken within the black oval. Timestep 70,000, elongation 15.0%.

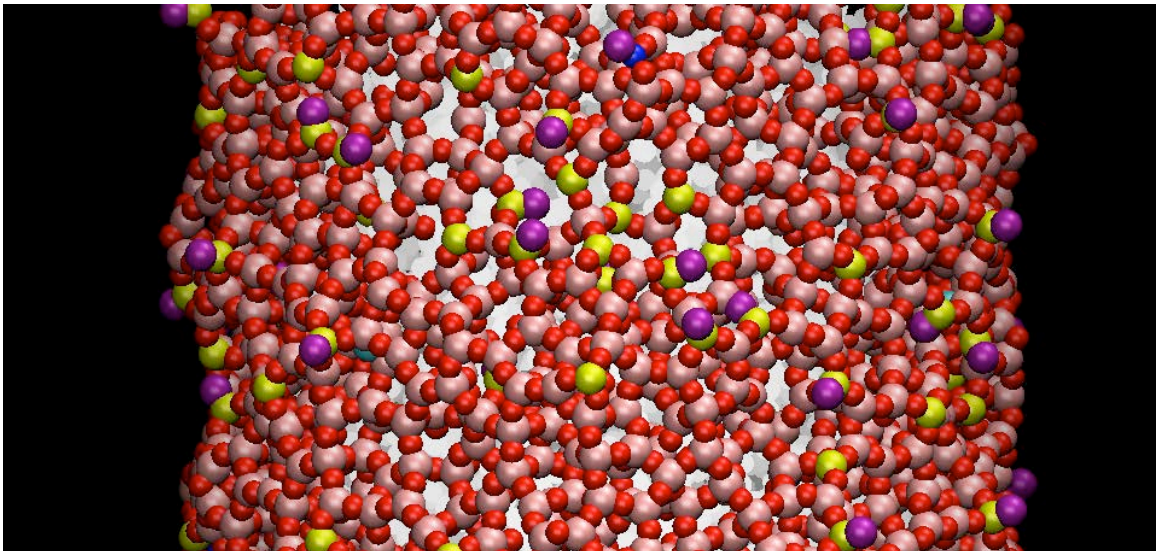

Figure 4-47. As the fiber is strained, bonds continue to break, as evidenced by the large number of three-coordinated silicon atoms shown in yellow, now on the surface. Timestep 71,500, elongation 15.3%.

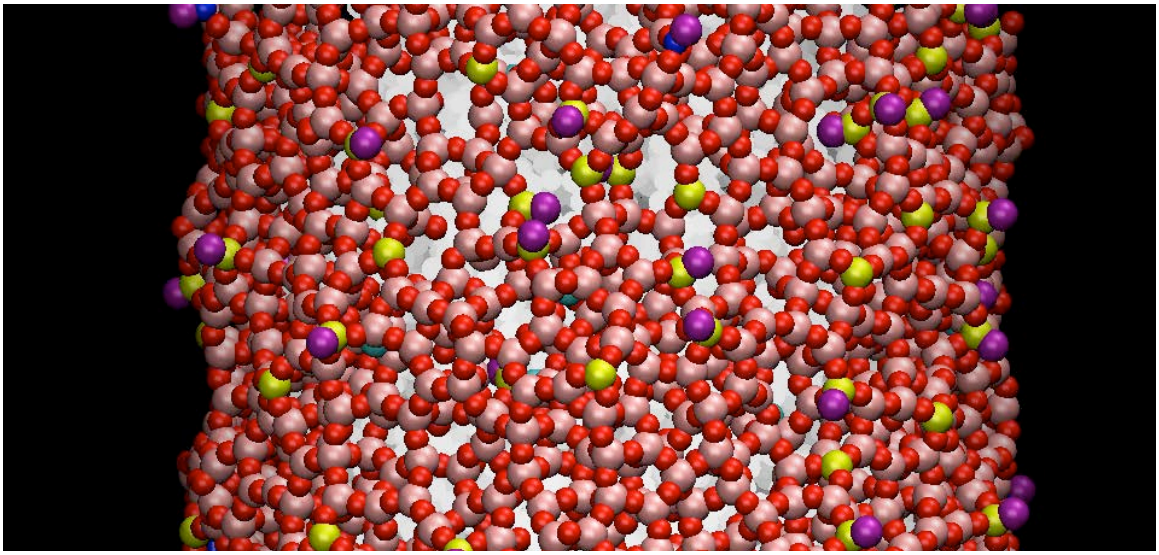

Figure 4-48. Despite the bonds on the surface that break, the overall surface structure remains intact, and no voids appear on the surface for some time. Timestep 81,000, elongation 17.6%.

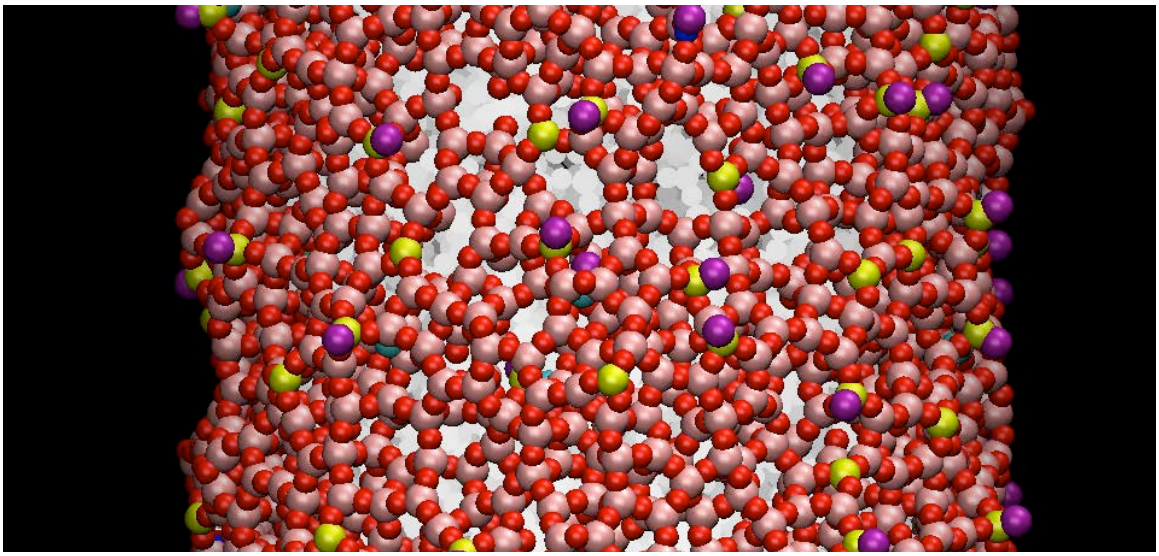

Figure 4-49. Fiber surface right before failure. Timestep 93,500, elongation 20.5%.

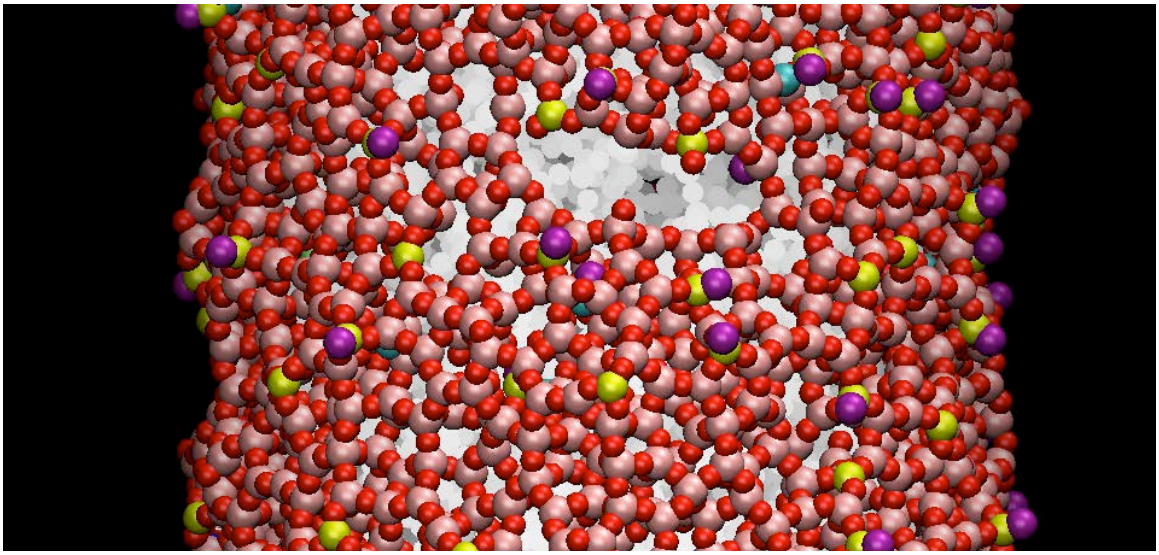

Figure 4-50. Crack C opens on the surface of the fiber. Timestep 94,500, elongation 20.8%.

Aside from the difference in the stress of the system at the time of the first bond failure, the formation of crack C appears to progress in a similar manner to the formation of voids A and B up to Figure 4-47. Beyond this point, a significant number of bonds break, as evidenced by the change in coordination of the atoms, but no voids open up in the surface. The atoms at the surface of the fiber are being recoordinated back into the structure from atoms within the bulk. This creates a porous region of the bulk sample, behind the surface structure visible in Figure 4-49.

This sub-surface formation is shown in Figures 4-51 and 4-52. Figure 4-51 shows timestep 71,500, where bond breakage on the surface was noted. In this figure, there is no apparent void in the sub-surface. In Figure 4-52, shown at timestep 90,000, a void has clearly formed below the surface, where atoms have been pulled to the surface to heal broken bonds.

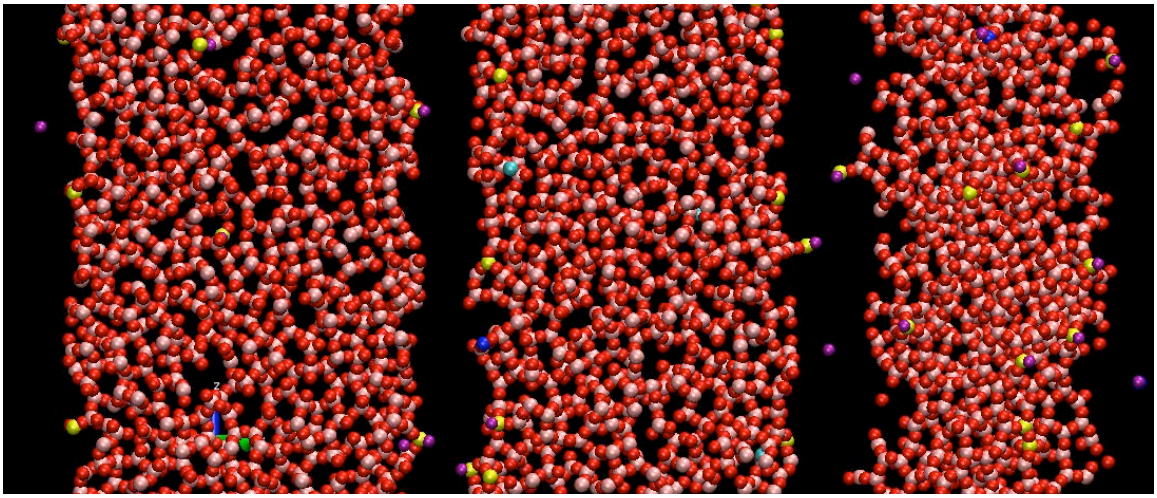

Figure 4-51. Three slices of the fiber are shown in this figure. From right to left they show progressively deeper views of the fiber, 7Å thick each. The structure appears to be intact, as it was before elongation of the fiber occurred.Timestep 71,500, elongation 15.3%.

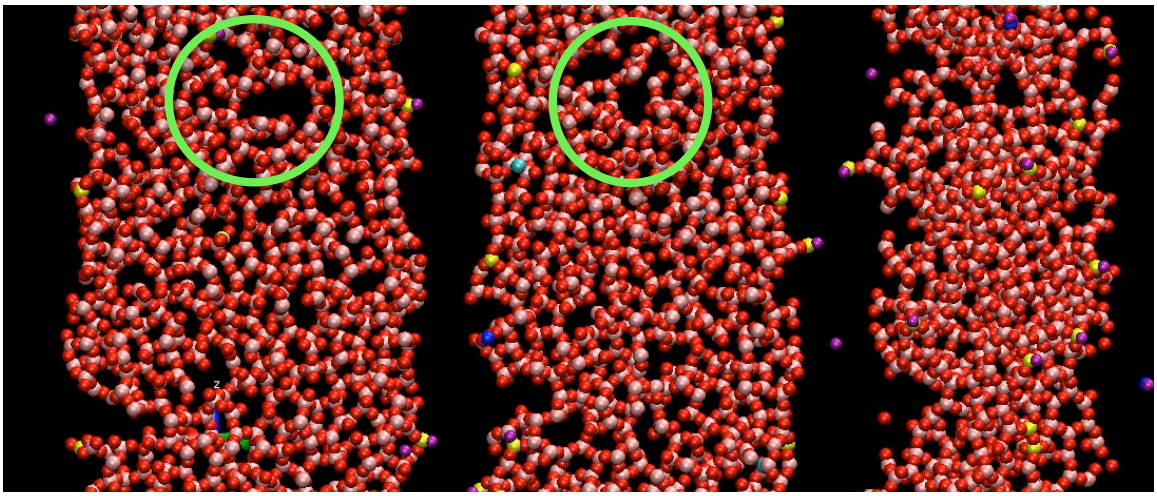

Figure 4-52. Three slices of the fiber are shown in this figure. From right to left they show progressively deeper views of the fiber, 7Å thick each. Voids are noted in the two deeper slices, and highlighted with green ovals. Timestep 90,000, elongation 19.7%.

This sub-surface void formation behind the weakening surface serves to create a less-dense region. When the remaining bonds at the surface fail, and crack C is formed, few bonds remain behind the crack front to slow the propagation of the crack into material, and it moves quickly into the bulk. The crack then runs the width of the fiber,

breaking the fiber in two. As the crack passes below voids A and B, stresses are released and they start to relax slightly, into a more closed position.

d. Summary of the Failure Process for the Cylindrical Fiber

In this sample, the crack and voids were formed through a series of bond breakages on the surface. The bonds that broke were associated with undercoordinated silicon, overcoordinated oxygen and bonds running parallel to the strain axis. Voids A and B opened up progressively throughout the straining process, visible on the surface, and their progress through the bulk of the sample was slowed by the network of bonds below the surface. As bonds broke on the surface of the fiber in the vicinity of crack C, atoms were pulled from the space behind the surface to heal these bonds. Crack C only visibly formed when the density of both the surface and the sub-surface regions was significantly reduced. When crack C opened, it moved quickly through the less-dense region behind it and into the bulk of the fiber at a higher speed than voids A and B. Crack C moved through the full width of the fiber, fracturing it.

11. Conclusions

As the simulated silica glass fibers were strained under tension, the bond-angles and lengths were distorted. Upon failure, bond-lengths returned to normal values, while bond-angles remained distorted due to the formation of fracture surfaces that contained small-membered rings and other defect species.

The samples broke from the surface layer, with a crack traveling from the surface inward, through the bulk, and across to the other side of the sample. This crack was formed through the failure of individual bonds, mostly those associated with three-coordinated silicon, triply-bonded oxygen and those running parallel to the strain axis. In the cylindrical fiber, several voids were formed in the surface, but only one crack ran the width of the fiber to cause failure. In addition to this failure process, bond breaking and reforming was noted in the fibers, at strain values well below the limit for elastic deformation.

Chapter Five – The Behavior of Sodium Silicate and Aluminosilicate Glasses Under Tension

1. Introduction

In Chapter Two, a range of sodium silicate and sodium aluminosilicate glasses were formed, and their structures were evaluated and compared with theory, experiments, and other simulations. The 12,000-atom systems studied were found to be of a reasonable and expected structure for the compositions studied, although they had an elevated fictive temperature. Thus, these samples were judged to be appropriate candidates for study under tensile strain, in a manner similar to the one used for bulk silica[36] and the silica fibers presented in Chapter Four. However, complications arose as these samples were tested under tensile strain. This chapter contains the analysis of these complications and suggestions as to their cause.

2. Straining Method

The straining method for these samples was the same as described for bulk samples in Chapter Three. When the silica fibers were strained, the extra space in the box allowed them to thin out naturally, with a non-zero Poisson's ratio, even though the simulations were run without modification of the box width in the x and y directions. To allow for that same behavior in the bulk samples, these simulations were run using NPT conditions to ensure that the x and y dimensions of the box could react appropriately to the strain in the z direction. These conditions were the same as those which have been previously used in a study of bulk silica glass.[36]

3. Distortion of the Structure Under Strain

As a first step towards modeling glasses with more compositional complexity, the sodium silicate glass samples were subjected to tensile strain. Under strain, the average bond-length between silicon and oxygen atoms and the bond-angle between silicon tetrahedra were tracked. The resultant values for the 10Na glass sample are shown in Table V-I.

Table V-I. Bond-angle Between Tetrahedra and Average Si-O Bond-Length for a 10Na Sodium Silicate Glass

Timestep	Box Elongation in Z	Bond-angle Si-O-Si	Average Si-O Bond-length (Å)
1	0.0 %	151.67	1.6127
10000	1.97 %	151.51	1.6220
50000	10.4 %	152.64	1.6127
100000	22.1 %	150.58	1.6252
150000	34.9 %	149.24	1.6252
200000	49.1 %	148.91	1.6262
250000	64.8 %	148.42	1.6252
290000	78.5 %	148.19	1.6252

Bond-angles and lengths were compressed and elongated under stress, respectively, but no release was seen, despite the fact that failure of the glass was expected at a strain of approximately 16%. [109] Visual examination of the fiber under strain revealed no failure of the material. Snapshots of the structure at different times in the straining process are shown in Figure 5-1.

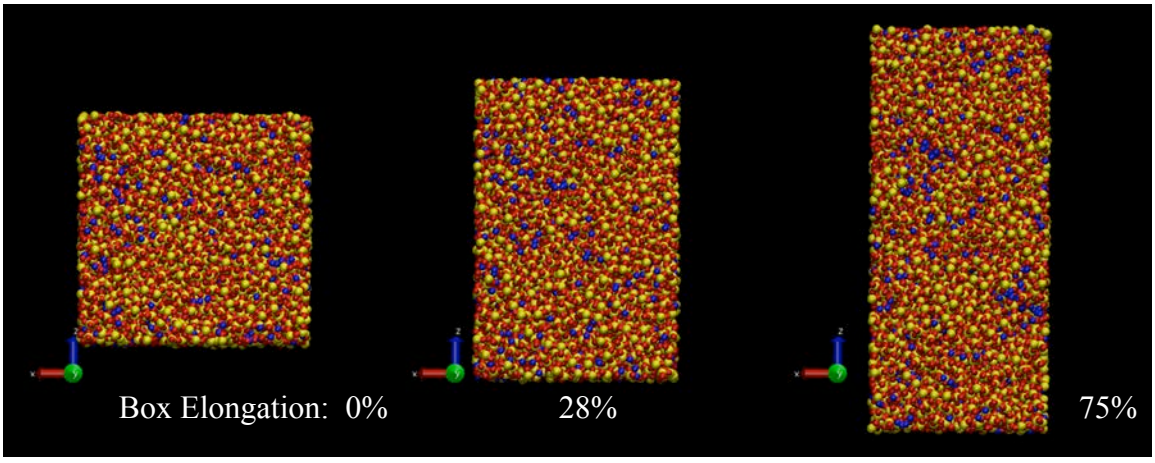

Figure 5-1. The 12,000-atom 10Na glass is shown here under tensile strain.

Although the glass was strained past the expected failure point, it continued to elongate and thin without breaking. Bond breaking and reforming was noted in the silica glass

fibers observed in Chapter Four, but such phenomena were somewhat localized, and did not appear to have an impact on the overall properties of the sample. This excessive elongation was not the behavior expected of a brittle solid, and was reminiscent of a viscous material. To test the type of deformation observed under strain, the sample was strained for 60,000 timesteps, to a strain of approximately 12%, and then released. In a brittle solid, only elastic deformation would be expected from tensile-straining process below the failure strain, and so full recovery of the original sample dimensions was expected. The initial and final geometries are shown in Figure 5-2, compared with a 12,000-atom bulk silica glass sample under the same testing conditions.

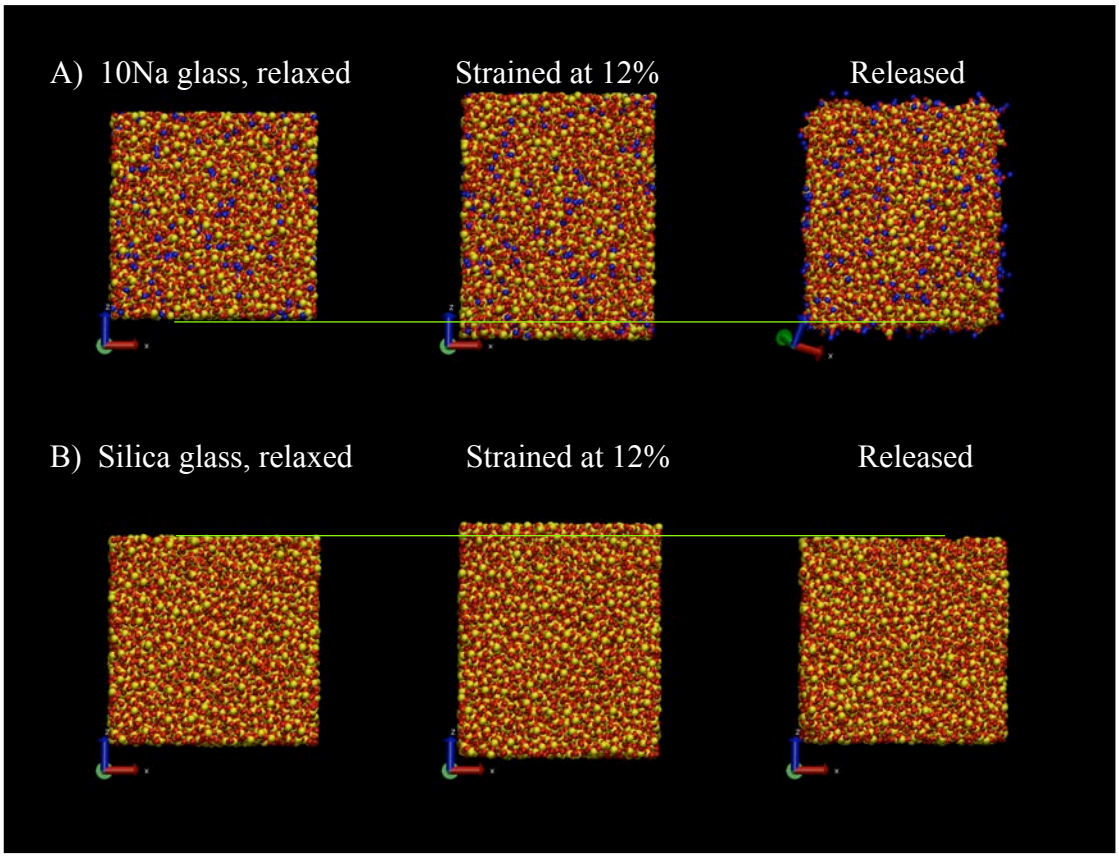

Figure 5-2. A) 10Na and B) silica glass samples are strained within the region of elastic deformation and released. The straight lines drawn across each sample illustrate the changes to sample geometry from the initial configuration, under strain, and the permanent change upon release.

In Figure 5-2B, the silica glass sample is seen to return to its original length, while in Figure 5-2A, the sodium silicate glass remains deformed after it was strained and

released. The sample was strained to 12%, but after the stress was released, the box still exhibited a strain of approximately 9%. Some of the deformation has been recovered elastically, but the remaining distortion of the sample suggested plastic deformation as well.

4. Thermostatting in MD

In DLPOLY, and in most Molecular Dynamics simulations, temperature is controlled through the use of a kinetic thermostat. Although many different types of kinetic thermostats exist, the basic principle behind them is the same. Kinetic temperature is determined by the average kinetic energy of the atoms in the system, given previously in Equation 1-2.[43]

In equilibrium conditions, the potential and kinetic energy of the system are coupled by the equipartition and virial theorems, so that controlling the kinetic temperature should also control a structural temperature, through the potential energy of the system. In order to achieve a desired temperature, the velocities of the atoms in the system are scaled up or down to bring the average system temperature closer to the temperature dictated by the thermostat. This neatly avoids the complexities that would be required to scale the potential energy term of the temperature, while still addressing the system structure through that kinetic energy – potential energy coupling.

However, glass systems do not obtain equilibrium, and so the potential energy of the system is not coupled to the kinetic energy. This means that the potential energy term of the temperature may not be accurately reflected in the kinetic energy temperature, and so the structural elements of the system temperature could be ignored by the kinetic thermostat.[44] This is a probable cause for the elevated fictive temperature noted the glass structural features discussed in Chapter Two.

If the temperature of the glass sample was not being well controlled, the viscous behavior of the system could be attributed to a high configurational temperature that was left unaddressed by the kinetic thermostat. To investigate this, the temperature of the systems was evaluated by a calculation based purely on the configurational energy of the system.

In a paper in 1997, Rugh presented an approach for measuring temperature of a microcannonical ensemble, using the Hamiltonian function.[113] Advancing on this, Butler et al. derived an expression for temperature based entirely on the configurational energy of the system, using just the potential energy term of the Hamiltonian, and termed it T_{config}.[114] Butler had developed this measure of temperature as a diagnostic tool to check the validity of the algorithms in Monte Carlo computer programs. A lack of agreement between the intended system temperature and T_{config} would reveal the presence of coding or algorithmic errors. In the absence of any computational errors, configurational temperature was found to quickly equilibrate to the desired system temperature.

Travis and Braga[44,45] have since worked to establish a reliable configurational thermostat for classical molecular dynamics simulations. Working from their papers, it was possible to write a code to calculate the configurational temperature of a snapshot from the MD simulations in the present study. Configurational temperature is calculated using Equation 4-2, and the position, velocity, and acceleration of the atoms within the system at a given timestep.

$$k_B T_{config} = \frac{\left\langle \sum_{i=1}^{N} \left(\partial U / d\vec{r}_i \right)^2 \right\rangle}{\left\langle \sum_{i=1}^{N} \left(\partial^2 U / d\vec{r}_i^{\,2} \right) \right\rangle} \tag{4-2}$$

Using this equation, the configurational temperature of a sample of 20Na glass was calculated every 500 timesteps of a 5000 timestep run at a kinetic temperature of 300K. The configurational temperature was found to be 303±5 K, indicating that the kinetic thermostat had provided adequate control over the glass-forming process, and that the formed sample appeared to be at room temperature. The configurational temperature of a 20Na glass was also monitored throughout the straining process, but no significant deviation from room temperature was noted as the system stretched.

This apparent agreement between the kinetic and configurational temperatures of the system fails to explain the elevated structural temperature of the glass and does not suggest the cause of the viscous, stretching behavior under tension. If the temperature of

the system is elevated, as suggested by the structure and dynamic behavior, it may be that this configurational thermostat equation is not complex enough to detect the change in system energy.

5. Forced Failure

These sodium silicate glass samples can be broken through the use of artificial constraints. If the x and y dimensions of the sample box are held constant as the sample is strained in z, enforcing a Poisson's ratio of 0, then the sample breaks. In a similar manner, changing the sample geometry to create a thinner rectangular box, which has a larger portion of the structure constrained by the periodic boundary conditions, also will cause the sample to break as an apparent brittle solid. As a sample box, originally measured as a cube 54.6 Å on each side, is thinned into a rectangular box it breaks at lower and lower values of strain, until a box measuring 30 Å by 30Å by 187 Å will break as expected in experimental work. Straining a sample at the low temperature of 10K also produced failure by a more brittle process.

However, the use of these artificial constraints to force the samples to break in a brittle manner is unwise when the source of the problem is not well defined. Although assumptions and approximations are often used to simplify scientific problems to make it possible to pursue a result, each assumption must be well understood before it is applied. In this case, it is not clear why such constraints are needed, and until the problem is well understood, modifications to the testing conditions should not be applied.

6. Conclusions

The viscous behavior noted when straining the sodium silicate and sodium aluminosilicate glass samples does not have a clear origin. Although evidence suggests that an increase in the energy of the system is allowing the reformation of bonds as the sample is deformed, this energy is not visible in either the potential and kinetic energy terms of the system. Further research is necessary to determine the cause of this behavior, and until a cause is found, analysis of the failure of the system is of questionable value.

Chapter Six - Conclusions

1. Conclusions and Future Work

In this work, molecular dynamics simulations were used to study the structure of glass samples on a scale that is unobservable by experimental techniques.

The silica glass fibers formed in this study had a distinct surface structure characterized by a lower atomic density and a high population of defect structures. This surface layer ranged in size, for samples containing between 12,000 and 599,040 atoms, but for larger fibers it was between 8 and 11Å thick. Because the size dependency of the surface layer thickness tapered off with increasing system sizes, samples only 5nm in diameter had a similar surface layer thickness to samples 20nm thick. These smaller 5nm diameter systems were strained under tension to study the failure process at an atomistic level.

When the silica glass fibers were strained, they broke at reasonable values of failure stress and strain, when compared to experimental studies of thin fibers and simulations of bulk silica glass. The failure process for each fiber was initiated at the surface, typically from several bond breakages in series that created a region of concentrated stress. The bonds that broke were usually associated with three-coordinated silicon, triply-bonded oxygen or ran parallel to the strained axis. As bonds broke, they created areas of concentrated stress in the bonds around them, as fewer bonds remained in that area to share the load. Under this concentrated stress, more bonds in this region broke, forming a small crack on the surface that propagated into the bulk of the sample. The fracture surfaces that were formed were also populated with a high concentration of defect species, like the initial surface layer on the exterior of the formed fiber.

One fiber showed the formation of several separate voids in the surface of the fiber before it broke. In this case, the crack that was moving the fastest was the one to travel across the full length of the fiber, while other surface cracks remained as voids on the surface when the fiber was broken.

The sodium silicate and sodium aluminosilicate glass samples formed were found to have an atomic structure that agreed well with the results of other computational work and experiments. However, the structure of these glasses indicated that they had an elevated structural temperature, similar to the structure of a splat-cooled glass. When these bulk samples were subjected to tension in the same manner as the silica fibers, they could not be strained until failure occurred. Viscous behavior was noted, and the samples elongated well beyond what would be expected from these brittle, elastic solids. The kinetic thermostat used in these simulations did not indicate an elevated system temperature. After writing a program to calculate system temperature based only on the potential energy of the system, configurational temperature was examined. This configurational thermostat also did not reveal any apparently elevated system temperature despite the high-temperature structure previously noted and the viscous behavior of the glass under tension.

Although structural and dynamic evidence suggests that these glass samples are at an elevated temperature, the thermostats used do not agree. It is possible that the current thermostats are missing information that would allow them to reflect an increase in temperature when samples are being strained. Or, a process unrelated to the thermostatting of the glass may cause this phenomenon. More work is needed to fully understand the cause of this behavior and to clear the way for future researchers to examine dynamic processes in glass compositions other than silica.

References

1) I. Beery, U. Lev, and D. Sherman, "On the lower limiting velocity of a dynamic crack in brittle solids," *J. Appl. Phys.,* **93** [5] 2429-34 (2003).

2) M.M. Chaudhri, "Self-sustained fracture waves in soda-lime glass," *Mater. Sci. Forum,* **662** 95-104 (2011).

3) M. Peroni, G. Solomos, V. Pizzinato, and M. Larcher, "Experimental investigation of high strain-rate behaviour of glass," *Appl. Mech. Mater.,* **82** 63-8 (2011).

4) G.D. Quinn, *Fractography of Ceramics and Glasses*. Ch. 5 pp. 1-70. National Institute of Standards and Technology, Washington, DC 2006.

5) G. Binnig and H. Rohrer, "Surface imaging by scanning tunneling microscopy," *Ultramicroscopy,* **11** [2-3] 157-60 (1983).

6) J.E. Shelby, *Introduction to Glass Science and Technology,* 2nd ed. pp. 69-89 Royal Society of Chemistry, Cambridge, UK, 2005.

7) A.C. Wright, "Diffraction studies of glass structure," *J. Non-Cryst. Solids,* **123** [1-3] 129-48 (1990).

8) A.C. Wright, B. Bachra, T.M. Brunier, R.N. Sinclair, L.F. Gladden, and R.L. Portsmouth, "Neutron diffraction and MAS-NMR study of the structure of fast neutron irradiated vitreous silica," *J. Non-Cryst. Solids,* **150** [1-3] 69-75 (1992).

9) J. Schneider, V.R. Mastelaro, E.D. Zanotto, B.A. Shakhmatkin, N.M. Vedishcheva, A.C. Wright, and H. Panepucci, "Qn distribution in stoichiometric silicate glasses: thermodynamic calculations and 29Si high resolution NMR measurements," *J. Non-Cryst. Solids,* **325** [1-3] 164-78 (2003).

10) B.J. Alder and T.E. Wainwright, "Studies in Molecular Dynamics I. General Method," *J. Chem. Phys.,* **31** [2] 459-67 (1959).

11) A. Rahman, "Correlations in the motion of atoms in liquid argon," *Phys. Rev.,* **136** A405-11 (1964).

12) M.P. Allen and D.J. Tildesley, *Computer Simulation of Liquids*. pp. 1-32. Clarendon Press, Oxford, 1989.

13) L.V. Woodcock, C.A. Angell, and P. Cheeseman, "Molecular Dynamics Studies of the vitreous state: Simple ionic systems and silica," *J. Chem. Phys.,* **65** [4] 1565 (1976).

14) B. Vessal, M. Amini, and C.R.A. Catlow, "Computer simulation of the structure of silica glass," *J. Non-Cryst. Solids,* **159** [1-2] 184-6 (1993).

15) G. Malavasi, M.C. Menziani, A. Pedone, and U. Segre, "Void size distribution in MD-modelled silica glass structures," *J. Non-Cryst. Solids,* **352** [3] 285-96 (2006).

16) G. Cormier, J.A. Capobianco, and A. Monteil, "Molecular dynamics simulation of the trivalent europium ion doped in silica and sodium disilicate glasses," *J. Non-Cryst. Solids,* **152** [2-3] 225-36 (1993).

17) L. Cormier, D. Ghaleb, D.R. Neuville, J.-M. Delaye, and G. Calas, "Chemical dependence of network topology of calcium aluminosilicate glasses: A computer simulation study," *J. Non-Cryst. Solids,* **332** [1-3] 255-70 (2003).

18) J. Du, "Molecular dynamics simulations of the structure and properties of low silica yttrium aluminosilicate glasses," *J. Am. Ceram. Soc.,* **92** [1] 87-95 (2009).

19) A. Takada, P. Richet, C.R.A. Catlow, and G.D. Price, "Molecular dynamics simulation of temperature-induced structural changes in cristobalite, coesite and amorphous silica," *J. Non-Cryst. Solids,* **354** [2-9] 181-7 (2008).

20) J.M. Delaye and D. Ghaleb, "Molecular dynamics simulation of SiO_2 + $B2O_3$ + Na_2O + ZrO_2 glass," *J. Non-Cryst. Solids,* **195** [3] 239-48 (1996).

21) J. Du and A.N. Cormack, "The medium range structure of sodium silicate glasses: A molecular dynamics simulation," *J. Non-Cryst. Solids,* **349** 66-79 (2004).

22) J. Du and L.R. Corrales, "Erbium implantation in silica studied by molecular dynamics simulations," *Nucl. Instrum. Methods Phys. Res., Sect. B,* **255** [1] 177-82 (2007).

23) A. Pedone, G. Malavasi, M. Cristina Menziani, U. Segre, and A.N. Cormack, "Role of magnesium in soda-lime glasses: Insight into structural, transport, and mechanical properties through computer simulations," *J. Phys. Chem. C,* **112** [29] 11034-41 (2008).

24) J. Du and A.N. Cormack, "Molecular dynamics simulation of the structure and hydroxylation of silica glass surfaces," *J. Am. Ceram. Soc.,* **88** [9] 2532-9 (2005).

25) S.H. Garofalini, "Molecular dynamics computer simulations of silica surface structure and adsorption of water molecules," *J. Non-Cryst. Solids,* **120** [1-3] 1-12 (1990).

26) S.M. Levine and S.H. Garofalini, "Surface structure of silica glasses by Molecular Dynamics simulations," *Mater. Res. Soc. Symp. Proc.,* **61** 29-37 (1986).

27) M. Wilson and T.R. Walsh, "Hydrolysis of the amorphous silica surface I. Structure and dynamics of the dry surface," *J. Chem. Phys.,* **113** 9180-90 (2000).

28) C. Mischler, W. Kob, and K. Binder, "Classical and ab-initio molecular dynamic simulation of an amorphous silica surface," *Comput. Phys. Commun.,* **147** 222-5 (2002).

29) C. Wang, N. Kuzuu, and Y. Tamai, "Molecular dynamics study on surface structure of a-SiO_2 by charge equilibration method," *J. Non-Cryst. Solids,* **318** [1-2] 131-41 (2003).

30) B. Anatoly B, "Molecular dynamics of silica at high pressures: Equation of state, structure, and phase transitions," *Geochim. Cosmochim. Acta,* **58** [6] 1557-66 (1994).

31) K. Trachenko and M.T. Dove, "Densification of silica glass under pressure," *J. Phys.: Condens. Matter,* **14** [32] 7449-59 (2002).

32) K. Trachenko and M.T. Dove, "Floppy modes in silica glass under pressure," *J. Phys.: Condens. Matter,* **14** [6] 1143-52 (2002).

33) J. Horbach, "Molecular dynamics computer simulation of amorphous silica under high pressure," *J. Phys.: Condens. Matter,* **20** (2008).

34) A. Takada, P. Richet, C.R.A. Catlow, and G.D. Price, "Molecular dynamics simulations of vitreous silica structures," *J. Non-Cryst. Solids,* **345-346** 224-9 (2004).

35) A. Takada, P. Richet, and T. Atake, "New description of structural disorder in silica glass," *J. Non-Cryst. Solids,* **355** [10-12] 694-9 (2009).

36) A. Pedone, M. Gianluca, C.M. Menziani, U. Serge, and A.N. Cormack, "Molecular Dynamics Studies of Stress-Strain Behavior of Silica Glass under a Tensile Load," *Chem. Mater.,* **20** 4356-66 (2008).

37) .H. Simmons, T.P. Swiler, and R. Ochoa, "Molecular dynamics studies of brittle failure in silica. Bond fracture," *J. Non-Cryst. Solids,* **134** [1-2] 179-82 (1991).

38) K. Muralidharan, J.H. Simmons, P.A. Deymier, and K. Runge, "Molecular dynamics studies of brittle fracture in vitreous silica: Review and recent progress," *J. Non-Cryst. Solids,* **351** [18] 1532-42 (2005).

39) J.H. Simmons, "What is so exciting about non-linear viscous flow in glass, molecular dynamics simulations of brittle fracture and semiconductor-glass quantum composites," *J. Non-Cryst. Solids,* **239** [1-3] 1-15 (1998).

40) L. Adkins and A. Cormack, "Large-scale simulations of sodium silicate glasses," *J. Non-Cryst. Solids,* **357** [14] 2538-41 (2011).

41) P.B. Balbuena and J.M. Seminario, *Molecular dynamics: from classical to quantum methods*. pp. 2-25 Elsevier Science, Amsterdam, 1999.

42) A. Pedone, G. Malavasi, M.C. Menziani, A.N. Cormack, and U. Segre, "A new self-consistent empirical interatomic potential model for oxides, silicates, and silicas-based glasses," *J. Phys. Chem. B,* **110** [24] 11780-95 (2006).

43) J.G. Powles, G. Rickayzen, and D.M. Heyes, "Temperatures: Old, new and middle aged," *Mol. Phys.,* **103** [10] 1361-73 (2005).

44) K.P. Travis and C. Braga, "Configurational temperature and pressure molecular dynamics: Review of current methodology and applications to the shear flow of a simple fluid," *Mol. Phys.,* **104** [22-24] 3735-49 (2006).

45) K.P. Travis and C. Braga, "Configurational temperature control for atomic and molecular systems," *J. Chem. Phys.,* **128** [1] (2008).

46) H.J.C. Berendsen, J.P.M. Postma, W. van Gunsteren, A. DiNola, and J.R. Haak, "Molecular dynamics with coupling to an external bath," *J. Chem. Phys.,* **81** 3684 (1984).

47) W. Smith, T.R. Forester, and I.T. Todorov, DL_POLY, [Computer Program] STFC Daresbury Laboratory, Warrington, WA and Cheshire, UK, 2009.

48) X. Yuan and A.N. Cormack, "Efficient algorithm for primitive ring statistics in topological networks," *Comput. Mater. Sci.,* **24** [3] 343-60 (2002).

49) V.A. Bakaev, W.A. Steele, T.I. Bakaeva, and C.G. Pantano, "Adsorption of CO_2 and Ar on glass surfaces. Computer simulation and experimental study," *J. Chem. Phys.,* **111** 9813-21 (1999).

50) M.M. Branda, R.A. Montani, and N.J. Castellani, " Monte Carlo simulation of amorphous silica dehydration," *Surf. Sci.,* **341** 295-303 (1995).

51) M.M. Branda, R.A. Montani, and N.J. Catellani, "The distribution of silanols on the amorphous silica surface: a Monte Carlo Simulation," *Surf. Sci.,* **446** L89-L94 (2000).

52) Y.C. Chen, Z. Lu, K.I. Nomura, W. Wang, R.K. Kalia, A. Nakano, and P. Vashishta, "Interaction of voids and nanoductility in silica glass," *Phys. Rev. Lett.,* **99** (2007).

53) E.B.W. III and S.H. Garofalini, "Relaxation of silica glass surfaces before and after stress modification in a wet and dry atmosphere: molecular dynamics simulations," *J. Non-Cryst. Solids,* **226** 47-57 (1998).

54) E.A. Leed and C.G. Pantano, "Computer modeling of water adsorption on silica and silicate glass fracture surfaces," *J. Non-Cryst. Solids,* **324** 48-60 (2003).

55) Y. Ma, A.S. Foster, and R.M. Nieminen, "Reactions and clustering of water with silica surface," *J. Chem. Phys.,* **122** [14] 1-9 (2005).

56) P.D. Maniar and A. Navrotsky, "Energetics of high surface area silicas," *J. Non-Cryst. Solids,* **120** [1-3] 20-5 (1990).

57) K.I. Nomura, Y.C. Chen, W. Weiqiang, R.K. Kalia, A. Nakano, P. Vashishta, and L.H. Yang, "Interaction and coalescence of nanovoids and dynamic fracture in silica glass: Multimillion-to-billion atom molecular dynamics simulations," *J. Phys. D: Appl. Phys.,* **42** [21] (2009).

58) R. Ochoa, T.P. Swiler, and J.H. Simmons, "Molecular dynamics studies of brittle failure in silica. Effect of thermal vibrations," *J. Non-Cryst. Solids,* **128** [1] 57-68 (1991).

59) C.G. Pantano, "What do we know about glass surfaces?," *Ceram. Eng. Sci. Proc.,* **22** 137-48 (2001).

60) C.L. Rountree, R.K. Kalia, E. Lidorikis, A. Nakano, L.V. Brutzel, and P. Vashishta, "Atomistic Aspects of Crack Propagation in Brittle Materials: Multimillion Atom Molecular Dynamics Simulations," *Annu. Rev. Mater. Res.,* **32** 377-400 (2002).

61) C.L. Rountree, S. Prades, D. Bonamy, E. Bouchaud, R. Kalia, and C. Guillot, "A unified study of crack propagatio in amorphous silica: Using experiments and simulations," *J. Alloys Compd.,* **437-435** 60-3 (2007).

62) T.F. Soules, "Molecular dynamic calculations of glass structure and diffusion in glass," *J. Non-Cryst. Solids,* **49** [1-3] 29-52 (1982).

63) T.P. Swiler, J.H. Simmons, and A.C. Wright, "Molecular dynamics study of brittle fracture in silica glass and cristobalite," *J. Non-Cryst. Solids,* **182** [1-2] 68- (1995).

64) M.I. Trioni, A. Bongiorno, and L. Colombo, "Structural Properties of silica surface: a molecular dynamics study," *J. Non-Cryst. Solids,* **220** 164-8 (1997).

65) L. Van Brutzel, C.L. Rountree, R.K. Kalia, A. Nakano, and P. Vashishta, "Dynamic fracture mechanisms in nanostructured and amorphous silica glasses million-atom molecular dynamics simulations," *Mater. Res. Soc. Symp. Proc.,* **703** 117-22 (2002).

66) J. Wang, A. Omeltchenko, R.K. Kalia, and P. Vashishta, "Molecular dynamics simulations of fracture in amorphous silica," *Mater. Res. Soc. Symp. Proc.,* **455** 267-72 (1997).

67) J.K. West, R. Latour Jr, and L.L. Hench, "Molecular modeling study of adsorption of poly-L-lysine onto silica glass," *J. Biomed. Mater. Res.,* **37** [4] 585-91 (1997).

68) X. Yuan and A.N. Cormack, "Local structure of MD-modeled vitreous silica and sodium silicate glasses," *J. Non-Cryst. Solids,* **283** 69-87 (2001).

69) Y. Cao, "Static and Dynamic Structural Properties of Alkali/Alkalin-Earth Alumino-Silicate Glasses"; PhD Thesis. Alfred University, Alfred, NY, 1994.

70) D.M. Zirl and S.H. Garofalini, "Structure of sodium aluminosilicate glasses," *J. Am. Ceram. Soc.,* **73** [10] 2848-56 (1990).

71) A.K. Varshneya, *Fundamentals of Inorganic Glasses*. pp. 87-114. Academic Press, San Diego, 1994.

72) W. LaCourse and A. Cormack, "Glasses with transitional structures," *Ceram. Trans,*, **82** 273-80 (1998).

73) C. Leonelli, G. Lusvardi, M. Montorsi, M.C. Menziani, L. Menabue, P. Mustarelli, and L. Linati, "Influence of small additions of Al_2O_3 on the properties of the Na_2O $3SiO_2$ glass," *J. Phys. Chem. B,* **105** [5] 919-27 (2001).

74) H. Maekawa, T. Maekawa, K. Kawamura, and T. Yokokawa, "Structural groups of alkali silicate glasses determined from 29Si MAS-NMR," *J. Non-Cryst. Solids,* **127** [1-2] 53-64 (1991).

75) J. Tan, S. Zhao, W. Wang, G. Davies, and X. Mo, "The effect of cooling rate on the structure of sodium silicate glass," *Mater. Sci. Eng. B.,* **106** [3] 295-9 (2004).

76) A.G. Clare, A.C. Wright, and R.N. Sinclair, "A Comparison of the structural role of Na^+ network modifying cations in sodium silicate and sodium fluoroberyllate glasses," *J. Non-Cryst. Solids,* **213-214** 321-4 (1997).

77) A. Kerrache, V. Teboul, D. Guichaoua, and A. Monteil, "Aging effects in supercooled silica. A molecular dynamics investigation," *J. Non-Cryst. Solids,* **322** 41-5 (2003).

78) J.F. Stebbins and P. McMillan, "Compositional and temperature effects on five-coordinated silicon in ambient pressure silicate glasses," *J. Non-Cryst. Solids,* **160** [1-2] 116-25 (1993).

79) L. Zheng, Q. An, R. Fu, S. Ni, and S.-N. Luo, "Densification of silica glass at ambient pressure," *J. Chem. Phys.,* **125** [15] (2006).

80) J.P. Rino, G. Gutierrez, I. Ebbsjo, R.K. Kalia, and P. Vashishta, "Distribution of rings and intermediate range correlations in silica glass under pressure - a molecular dynamics study," *Mater. Res. Soc. Symp. Proc,* **408** 333-8 (1996).

81) N.T. Huff, E. Demiralp, T. Cagin, and W.A. Goddard III, "Factors affecting molecular dynamics simulated vitreous silica structures," *J. Non-Cryst. Solids,* **253** [1-3] 133-42 (1999).

82) V.R.G. Della and E. Venuti, "High-pressure densification of silica glass: A molecular-dynamics simulation," *Phys. Rev. B: Condens. Matter,* **54** 3809-16 (1996).

83) F. Leonforte, A. Tanguy, J.P. Wittmer, and J.L. Barrat, "Inhomogeneous elastic response of silica glass," *Phys. Rev. Lett.,* **97** [5] (2006).

84) L.T. Vinh, P.K. Hung, N.V. Hong, and T.T. Tu, "Local microstructure of silica glass," *J. Non-Cryst. Solids,* **355** [22-23] 1215-20 (2009).

85) M. Benoit, S. Ispas, P. Jund, and R. Jullien, "Model of silica glass from combined classical and ab initio molecular-dynamics simulations," *Eur. Phys. J. B,* **13** [4] 631-6 (2000).

86) T.F. Soules, "Models of glass strength and relaxation phenomena suggestsed by molecular dynamics simulations " *J. Non-Cryst. Solids,* **73** [1-3] 315-30 (1984).

87) A. Takada, "Molecular dynamics simulation of crystalline and vitreous silica"; pp. 179-87 in *Advances in Glass and Optical Materials II: Ceramic Transactions*, Vol. 197, Proceedings of the 6th Pacific Rim Conference on Ceramic and Glass Technology. Edited by A. Mario, John Wiley & Sons, Inc., 2006.

88) A. Takada, "Molecular dynamics simulation of deformation in SiO_2 and Na_2O-SiO_2 glasses," *J. Ceram. Soc. Jpn.,* **116** [1356] 880-4 (2008).

89) S.K. Mitra, "Molecular Dynamics Simlation of Silicon Dioxide Glass," *Philos. Mag. B,* **45** 529-48 (1982).

90) N. Kuzuu, K. Nagai, M. Tanaka, and Y. Tamai, "Molecular dynamics study of compressibility of vitreous silica," *Jpn. J. Appl. Phys., Part 1,* **44** [11] 8086-7 (2005).

91) N. Kuzuu, H. Yoshie, Y. Tamai, and C. Wang, "Molecular dynamics study of temperature dependence of volume of amorphous silica," *J. Non-Cryst. Solids,* **349** 319-30 (2004).

92) K. Yamahara, K. Okazaki, and K. Kawamura, "Molecular dynamics study of the thermal behaviour of silica glass/melt and cristobalite," *J. Non-Cryst. Solids,* **291** [1-2] 32-42 (2001).

93) B.M. Lee, S. Munetoh, T. Motooka, Y.-W. Yun, and K.-M. Lee, "Molecular-dynamics analysis of the structural properties of silica during cooling," *Diffus. Defect Data, Pt. B,* **139** 101-6 (2008).

94) L. Berthier, "Revisiting the slow dynamics of a silica melt using Monte Carlo simulations," *Phys. Rev. E: Stat., Nonlinear, Soft Matter Phys.,* **76** (2007).

95) Y. Liang, C.R. Miranda, and S. Scandolo, "Temperature-induced densification of compressed SiO_2 glass: A molecular dynamics study," *High Pressure Res.,* **28** [1] 35-44 (2008).

96) Y.C. Chen, K.I. Nomura, R.K. Kalia, A. Nakano, and P. Vashishta, "Void deformation and breakup in shearing silica glass," *Phys. Rev. Lett.,* **103** 155506-1 -5 (2009).

97) A.N. Cormack and X. Yuan, "Molecular Dynamics Simulations of Glass Surface Structure," *Am. Ceram. Soc. Bull.,* **9** 1 (1999).

98) A. Abbas, J.-M. Delaye, D. Ghaleb, and G. Calas, "Molecular dynamics study of the structure and dynamic behavior at the surface of a silicate glass," *J. Non-Cryst. Solids,* **315** [1-2] 187-96 (2003).

99) V.A. Bakaev and W.A. Steele, "On the computer simulation of a hydrophobic vitreous silica surface," *J. Chem. Phys.,* **111** 9803-607 (1999).

100) V.A. Bakaev, W.A. Steele, and C.G. Pantano, " On the computer simulation of silicate glass surfaces," *J. Chem. Phys.,* **114** 9599-607 (2000).

101) E.B. Webb and S.H. Garofalini, "Relaxation of silica glass surfaces before and after stress modification in a wet and dry atmosphere: molecular dynamics simulations," *J. Non-Cryst. Solids,* **226** 47-57 (1998).

102) A.S. D'Souza and C.G. Pantano, "Hydroxylation and Dehydroxylation Behavior of Silica Glass Fracture Surfaces," *J. Am. Ceram. Soc,* **85** [6] 1499-504 (2002).

103) A. Pedone, G. Malavasi, M. Cristina Menziani, U. Segre, and A.N. Cormack, "Molecular dynamics studies of stress-strain behavior of silica glass under a tensile load," *Chem. Mater.,* **20** [13] 4356-66 (2008).

104) C.L. Rountree, D. Bonamy, D. Dalmas, S. Prades, R.K. Kalia, C. Guillot, and E. Bouchaud, "Fracture in glass via molecular dynamics simulations and atomic force microscopy experiments," *Phys. Chem. Glasses: Eur. J. Glass Sci. Technol., Part B,* **51** [2] 127-32 (2010).

105) C.L. Rountree, S. Prades, D. Bonamy, E. Bouchaud, R. Kalia, and C. Guillot, "A unified study of crack propagation in amorphous silica: Using experiments and simulations," *J. Alloys Compd.,* **434-435** 60-3 (2007).

106) T.P. Swiler, "Atomistic fracture of silica glass-predictably unpredictable," *Glass Res.,* **11** [2] 10-1 (2002).

107) T.P. Swiler, J.H. Simmons, and A.C. Wright, "Molecular dynamics sudy of brittle fracture in silica glass and cristobalite," *J. Non-Cryst. Solids,* **182** 68-77 (1995).

108) N.P. Lower, R.K. Brow, and C.R. Kurkjian, "Inert failure strains of sodium aluminosilicate glass fibers," *J. Non-Cryst. Solids,* **344** [1-2] 17-21 (2004).

109) N.P. Lower, R.K. Brow, and C.R. Kurkjian, "Inert failure strain studies of sodium silicate glass fibers," *J. Non-Cryst. Solids,* **349** 168-72 (2004).

110) J. Andersons, R. Joffe, M. Hojo, and S. Ochiai, "Glass fibre strength distribution determined by common experimental methods," *Compos. Sci. Technol.,* **62** [1] 131-45 (2002).

111) P.K. Gupta and C.R. Kurkjian, "Intrinsic failure and non-linear elastic behavior of glasses," *J. Non-Cryst. Solids,* **351** [27-29] 2324-8 (2005).

112) K.I. Nomura, Y.C. Chen, R.K. Kalia, A. Nakano, and P. Vashishta, "Defect migration and recombination in nanoindentation of silica glass," *Appl. Phys. Lett.,* **99** (2011).

113) H.H. Rugh, "Dynamical approach to temperature," *Phys. Rev. Lett.,* **78** [5] 772 (1997).

114) B.D. Butler, G. Ayton, O.G. Jepps, and D.J. Evans, "Configurational temperature: verification of Monte Carlo simulations," *J. Chem. Phys.,* **109** [16] 6519- (1998).